NARROWBAND PHOTON PAIRS FROM A COLD ATOMIC VAPOUR FOR INTERFACING WITH A SINGLE ATOM

GURPREET KAUR GULATI

M.Sc. (Physics), Guru Nanak Dev University

A THESIS SUBMITTED FOR THE DEGREE OF DOCTOR OF PHILOSOPHY

CENTRE FOR QUANTUM TECHNOLOGIES

NATIONAL UNIVERSITY OF SINGAPORE

2015

Declaration

I hereby declare that the thesis is my original work and it has been written by me in its entirety. I have duly acknowledged all the sources of information which have been used in the thesis.

The thesis has also not been submitted for any degree in any university previously.

Gurpreet Kaur Gulati
December 14, 2014

To,

The two most important men in my life:

my father, S.Parminder Singh Gulati

and my husband, Ritayan Roy

Acknowledgements

First and foremost, I offer my sincerest gratitude to my supervisor, Prof. Christian Kurtsiefer , who has supported me thoughout my thesis with his patience and knowledge whilst allowing me the room to work in my own way. The confidence, he has shown in me, has motivated me to persistently work hard on the experiment. I attribute the level of my Ph.D degree to his encouragement and effort and without him this thesis, too, would not have been completed or written.

Besides my supervisor, I would like to thank my labmate, my friend, Bharath Srivathsan, for stimulating discussions, for the sleepless nights we were working together and for all the fun and happiness we shared together with good results, in the last five years. His smartness and intelligence has always inspired and motivated me to think 'out of box'.

Alessandro Ceŕe, for being supportive during the experiments. Brenda Chng, for teaching me the basics when I joined the group and for proofreading my thesis. Siddarth Joshi, for giving me 'instant' ideas whenever I felt stuck and 'instant' emotional support whenever I felt down. Victor Leong, for proof-reading my thesis. It was fun to work with him and Sandako while doing HOM measurements. Gleb, for always teasing me. I still miss that. Dzmitry, for his great ideas. One can approach him anytime and any day and he is always ready to clear your doubts. Syed, Mathias, Victor, Peng Kian, Houshun, DHL, Wilson, Kadir for creating a friendly and cheerful environment in the lab.

My father, my best friend, a great inspiration. Actually, thanks is a small word for him. His constant prayers and blessings has given me strength to fight any difficult situation. My mother, for giving unconditional love. Other members of my family: Rajpreet, Dr. Manpreet, Dr. Deb. Rikhia didi, Indra jiju, for their support. My father and mom in law for always encouraging me to focus on my career.

Lastly my husband, my soulmate Ritayan, who has always encouraged me to be what I am. I am really lucky that I have met him in Switzerland.

Contents

Summary

Recent advances to build quantum networks and quantum repeaters with atom ensembles, benefit from the photon pair sources that not only generate nonclassical light, but also resonant, narrowband light. In this thesis, we characterize one such photon pair source. We take advantage of a fourwave mixing process in a cold atomic ensemble of ^{87}Rb atoms. We use a cascade level scheme that allows to generate non-degenerate, near infrared signal and idler photon pairs. The bandwidth of the generated photons, measured using a Fabry-Perot cavity, is tuneable from 10 MHz–30 MHz with the optical density of the atomic cloud. We observe an instantaneous rate of 20,000 pairs per second using silicon avalanche photodetectors and an efficiency indicated by a pair-to-single ratio of 17%. The rates and efficiency reported are uncorrected for losses due to non-unit detector efficiency, filtering efficiency, and fiber coupling efficiency. We perform a Hanbury-Brown-Twiss measurement individually in the signal and idler modes. The results reveal the thermal nature of light from both conversion modes. The violation of Cauchy-Schwarz by a factor of 50×10^6, indicates a strong non-classical correlation between the generated lights. We further present an estimation of the polarization entangled state of the generated photon pairs by performing quantum state tomography. We show that the resulting polarization entangled state is not maximally entangled due to the dependence on Clebsch-Gordan coefficients that couple the individual Zeeman states of the different hyperfine levels involved in the fourwave mixing process.

The bandwidth, wavelength and brightness of the generated photons makes our source a prime candidate for interfacing with ^{87}Rb atoms, a common workhorse for quantum memories. As an initial step towards interfacing, we have performed a Hong-Ou- Mandel (HOM) interference experiment between a single photon from spontaneous decay of a single ^{87}Rb atom and a heralded single photon from our source. The measured interference visibility of 66.4% without any accidental correction and 84.5% with accidental correction is well beyond the classical limit of 50%. The experiment demonstrates indistinguishability of single photons generated from two different physical systems which is an important step towards establishing quantum networks.

List of Publications

1. B.Shrivathsan, **G.K Gulati**, B. Chng, D.Matsukevich and C.Kurtsiefer. **Narrowband Source of transform-limited photon pairs via fourwave mixing in cold atomic ensemble,** *Physical Review letters* , 111, 123602, 2013.

2. **G.K Gulati**, B.Shrivathsan, B. Chng, A.Cére, D.Matsukevich and C.Kurtsiefer. **Generation of exponentially rising field from parametric conversion in atoms,** *Physical Review A*, 90, 003819, 2014.

3. B.Shrivathsan, **G.K Gulati**, A.Cére, B. Chng, D.Matsukevich and C.Kurtsiefer. **Reversing the temporal envelope of a heralded single photon using a cavity,** *Physical Review letters*, 113, 163601, 2014 .

The results presented in Chapter 4 and Chapter 5 of this thesis are manuscripts in preparation.

List of Tables

List of Figures

Chapter 1

Introduction

In 1905, Albert Einstein's quantum theory of light introduced a non-classical understanding of light and matter. One of his early papers [5] based on Max Planck's work on black body radiations postulated the existence of light-quanta, later termed as a 'photon' by Gilbert Lewis in 1926 [6]. A practical definition of a single photon is to relate it to the detection process: a single photon is a single 'click' on an ideal detector [7].

There are different ways to produce single photons in the laboratory. One way is to use single quantum emitters such as a single atom [8], a NV centre in diamond [9, 10], a single ion [11], or a quantum dot [12, 13], which ideally should emit a single photon 'on demand' per excitation. However, to collect sufficient fluoroscence from a single quantum emitter, it should be confined inside a high numerical aperture lens or inside a high finesse optical cavity [14, 15]. An experimentally simpler way of generating single photons is to use photon pair sources based on parameteric conversion process. Such sources rely on the probabilistic generation of photon pairs where the detection of one photon of the pair 'heralds' the presence of a single photon in the other arm. In this thesis, we will focus on building and characterzing such a photon pair source [16].

Photon pair sources are a resource for wide range of quantum optics experiments ranging from fundamental test of quantum mechanics [17, 18, 19] to applications in quantum information processing, quantum computation and quantum cryptography [20, 21, 22, 23]. Most of these applications, however, are based on manipulation or detection of photons only.

More complex quantum information tasks require interfacing of photons to other physical systems. A typical example is a quantum network where information is stored or processed inside a node which could be a single ion [24], atoms in a cavity [25, 26], or an ensemble of atoms [27, 28]. Several proposals for quantum network architectures can be realised in practice by using photon pair sources [29]. For instance, the DLCZ long-distance quantum communication protocol [30] is based on interfacing entangled photon pairs with atomic ensembles. This requires efficiently absorbing photons and storing entanglement. Our photon pair source is suitable for such applications.

To have an efficient atom-photon interface, it is essential that the bandwidth of interacting photons should be on the order of the atomic linewidth (few tens of Megahertz). So far, most of the photon pair sources based on spontaneous parametric down-conversion in $\chi^{(2)}$ non-linear crystals and waveguides exhibit a relatively wide optical bandwidth ranging from 0.1 to 2 THz [31, 32]. Therefore, various filtering techniques have been employed to reduce the bandwidth of parametric fluorescence light. In addition, the parametric conversion bandwidth may be redistributed within the resonance comb of an optical cavity [33, 34, 35]. Using non-linear crystals and filter cavities, photon pairs of bandwidth around a few tens of Megahertz have been reported [33]. An alternative approach to this problem is to generate photon pairs via a fourwave mixing process (FWM) in an atomic vapor. Atoms, unlike other non-linear crystals have discrete energy levels which leads to narrow bandwidth of photons. Correlated photon pairs generated by FWM in a hot ^{85}Rb atomic ensemble have been observed [36, 37], with an optical bandwidth of 350 and 450 MHz, respectively. On the other hand, using cold atoms can reduce Doppler broadening due to atomic motion which in turn can reduce the bandwidth of the collected fluorescence to within natural atomic linewidth [16, 38, 39].

In this thesis, we will present a narrowband and a bright source of time correlated photon pairs based on parametric conversion in a cold cloud of ^{87}Rb atoms via a fourwave mixing process. The generated photon pairs are entangled in polarization degree of freedom which can be used to implement entanglement swapping [40] and other quantum communication protocols with single atoms or atomic ensembles [30]. The bandwidth and wavelength of the generated photons is suitable to interface with ^{87}Rb atoms, a common workhorse for quantum memories. As a first step towards interfacing, we have performed a Hong-Ou-Mandel interference experiment [41] between a single photon from spontaneous decay of a single ^{87}Rb atom [8] and a heralded single photon from our source [42]. This experiment demonstrates the indistinguishability of single photons generated from two different physical systems which is an important step towards establishing quantum networks especially for the applications where two different physical systems are required to serve as different nodes of the network [43, 44].

1.1 Thesis outline

Chapter 2 : We start by describing the experimental tools and techniques necessary to build the photon pair source. The list includes lasers, techniques to lock the laser, tapered amplifier, cooling and trapping the atoms. This is followed by the description of experimental setup and source alignment procedure.

Chapter 3 : In this Chapter, we discuss the temporal properties of the generated photon pairs via a cross correlation measurement. The bandwidth of the generated photons is measured using a Fabry-Perot cavity. We describe some characterstic qualities of the photon pair source including total pair detection rates, accidental rates and heralding efficiencies.

Chapter 4 : Here, we discuss the production of photon pairs entangled in polarization degree of freedom. The resultant polarization entangled state is determined by performing quantum state tomography. We also present an observation of controlled, high-contrast quantum beats in the time correlation measurement between the generated photon pairs.

Chapter 5 : In this Chapter, we present a Hong-Ou-Mandel interference experiment between a single photon from spontaneous decay of a single atom and heralded single photon from our source. We observe a HOM dip by varying the extent of overlap between the temporal envelope of the two photons.

Chapter 2

Experimental tools and techniques

In this Chapter, we will discuss the technical details of the experimental setup that are generic to all the experiments discussed in subsequent chapters. The first Section gives a brief overview of Four-Wave Mixing (FWM) process and photon pair generation. This is followed by a description of the equipment and techniques necessary to build our photon pair source. Finally we will discuss the experimental setup and the alignment procedure.

2.1 Four-Wave Mixing (FWM)

FWM is a third order non-linear process that involves the interaction of four optical fields in a non-linear medium.

When a non-linear dielectric material is placed in an external optical field, the field induces a dipole moment and polarizes the material. The response of a dielectric material to the external optical field can be written in a series expansion as

$$P = \epsilon_0 \left(\chi^{(1)} E + \chi^{(2)} E^2 + \chi^{(3)} E^3 + \ldots . \right), \tag{2.1}$$

where E is the applied optical field, P is the polarization of the medium defined as the induced dipole moment per unit volume, $\chi^{(1)}$ is a linear susceptibility related to refractive index of the medium $n = \sqrt{1 + \chi^{(1)}}$, ϵ_0 is the permitivity of free space and $\chi^{(2)}$, $\chi^{(3)}$ are the second and third order non-linear susceptibilities. Usually the higher order terms are very small and can be ignored. However, for certain materials and sufficiently

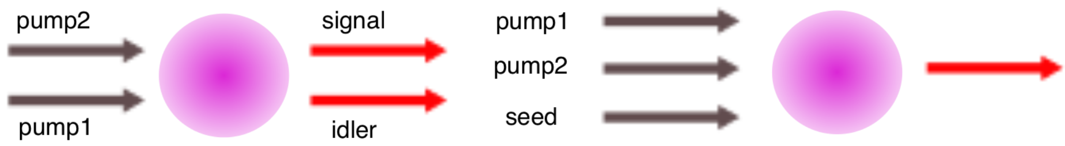

Figure 2.1: (Left) Spontaneous Four-Wave Mixing process (Right) stimulated Four-Wave Mixing in a cloud of atoms.

high field strengths, these terms become noticeable. For the past two decades, the most common method of generating photon pairs is via spontaneous parametric down conversion in PPKTP (periodically poled potassium titanyl phosphate) and BBO (beta barium borate) crystals which is a second order nonlinear process [31, 32].

An alternative approach to generate photon pairs is based on FWM, a third order non-linear process, observed in centrosymmetric materials such as photonic crystal fibers [45, 46], silicon waveguides [47], neutral atoms [48] etc. These materials do not allow $\chi^{(2)}$ non-linearity due to presence of inversion symmetry [49]. Other applications of FWM process include phase conjugation [50, 51], holographic imaging [52] and generation of squeezed light [53].

We use a dense cloud of atoms as a non-linear medium to generate time correlated photon pairs. Pair generation in atoms is a spontaneous FWM process [16], where two pump beams interact with the atomic medium to generate time correlated photon pairs. We label them as signal and idler. The process can be stimulated [54], where in addition to the two pump beams, a third seed beam interacts with the medium to coherently emit a new light. In a spontaneous FWM process, however, in place of seed beam, the vacuum fluctuations in the signal mode seeds the generation of a photon in the idler mode. Figure 2.1 illustrates the two processes. We will use stimulated FWM process as an initial step to align the photon pair source which will be discussed in Section 2.4.

2.1.1 Energy and momentum conservation

In any parametric process such as FWM, the quantum state of the medium remains unchanged before and after the interaction. This implies that there should be no net

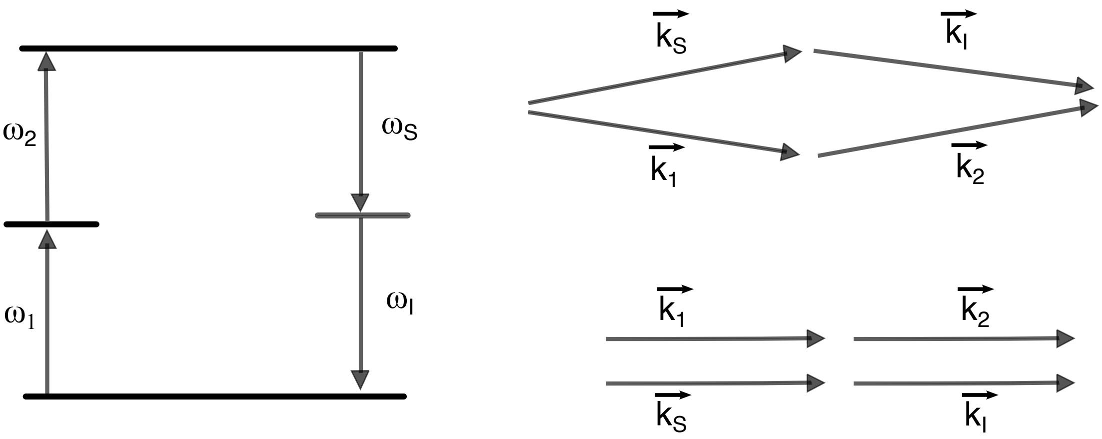

Figure 2.2: (Left) Energy conservation in FWM process. (Right) Two possible phase matching geometries for the pump and collection modes. (Top) Co-propagating pump beams with a small angle between them. (Bottom) Pump, signal and idler modes in a collinear co-propagating geometry.

transfer of energy, momentum, or angular momentum between the incident light and the interacting medium and therefore, these parameters must be conserved in between the pump and converted light fields.

Energy conservation in the FWM process can be written in terms frequency of pumps, signal and idler modes as:

$$\omega_1 + \omega_2 = \omega_\mathrm{S} + \omega_\mathrm{I} \tag{2.2}$$

A cascade decay can generate photon pairs even when only a single atom is interacting with pump beams. Since spontaneous emission from a single atom is more or less isotropic, a high numerical aperture lens is required to collect sufficient fluorescence. This was the case in a initial atomic beam experiments [48] which had only a very small number of atoms participating in the excitation and decay process at any time. A spatially extended atomic ensemble, however, provides translational symmetry which leads to momentum conservation or phase matching for the conversion process. The phase matching condition can be written as

$$\vec{k_1} + \vec{k_2} = \vec{k_\mathrm{S}} + \vec{k_\mathrm{I}}, \tag{2.3}$$

where $\vec{k_1}$, $\vec{k_2}$, $\vec{k_\mathrm{S}}$ and $\vec{k_\mathrm{I}}$ are the wave vectors of the pumps, signal and idler modes. This signifies that for a given geometry of pump beams, the signal and the idler photons are emitted into spatial modes defined by phase matching condition as illustrated in Figure 2.2. The phase matching condition allow for relatively simpler collection of the photons into single mode fibres without the need for high numerical aperture lenses. In addition to conservation of energy and momentum, the total angular momentum must also be conserved in the FWM process. This is one of the condition to generate photon pairs entangled in polarization degree of freedom. The details will be discussed in Chapter 4.

2.2 Fundamentals

The heart of the experiment is our source of photon pairs: an ensemble of ^{87}Rb atoms, trapped and cooled with a Magneto-Optical Trap (MOT). We also need a source of coherent light to talk to the atoms. In the following subsections, we will discuss the details of the components comprising such a photon pair source.

2.2.1 Rubidium

We choose Rubidium atoms because the level structure is well studied [3] and the diode lasers to address the optical transitions in Rubidium are easily available in the market. ^{87}Rb is a naturally occurring isotope of Rubidium with atomic number 37. It has a natural abundance of 28%, mass of 86.9 amu with a nuclear spin I of 3/2. Rubidium has another naturally occurring isotope with nucleon number 85. We choose ^{87}Rb for its compatibility with another experiment in our group with a single trapped atom [8].

We use a cascade level scheme in ^{87}Rb as shown in Figure 2.3 (Right) similar to the scheme used by [38, 55]. It involves four levels with one ground level ($5S_{1/2}$), two intermediate levels ($5P_{3/2}$, $5P_{1/2}$) and one excited level ($5D_{3/2}$). Another commonly used level scheme for photon pair generation in atoms is double lambda scheme as shown in Figure 2.3 (Left). Seminal experiments by Kuzmich et al [27] and Vanderwal et al [56] utilised double lambda level scheme in alkali atoms to create nearly degenerate photon pairs. Work at Stanford in the Harris group has made improvements to the pair generation rates with the first demonstration of electromagnetic Induced Transparency (EIT) in double lambda scheme [39, 57]. It is important to point out differences between the two schemes. The cascade level scheme allows for the generation of pairs that are

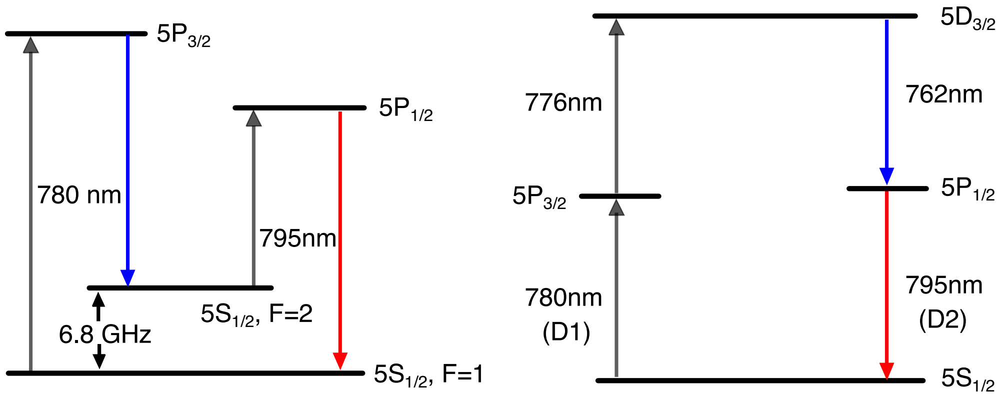

Figure 2.3: Level schemes for photon pair generation in ^{87}Rb atoms. (Left) Double lambda level scheme. (Right) Cascade level scheme similar to what we use for the experiment. The more detailed level version of this scheme with the hyperfine levels is shown in Figure 2.10

quite different in frequency from the pump beams. Therefore, one can easily filter out the contamination of pump beams into the collection modes using interference filters.

2.2.2 Lasers

We address the two lowest energy optical transitions in ^{87}Rb: D1 (780 nm) and D2 (795 nm), using solid state diode lasers from Sanyo (DL7140-201SW). The recommended forward current to operate the diodes is 100 mA. However, we operate the diodes around 70 mA to increase their lifetime. This gives an output power of around 35 mW. The free running wavelength of these diodes at room temperature (25° C) is between 780 − 785 nm. We tune the temperature of the diodes to achieve the desired wavelength. To address D2 line, we raise the temperature of the laser diode to around 65° C with a peltier element. The two excited transitions of the cascade with the wavelength of 762 nm and 776 nm are addressed using a ridge waveguide diodes from Eagleyard (EYP-RWE-0790-04000-0750-SOT01-0000). We operate these diodes at 100 mA with an output power of 60 mW.

In order to coherently probe an atomic transition, the linewidth of the lasers should be narrower than the natural linewidth of the transition. The linewidth of the free

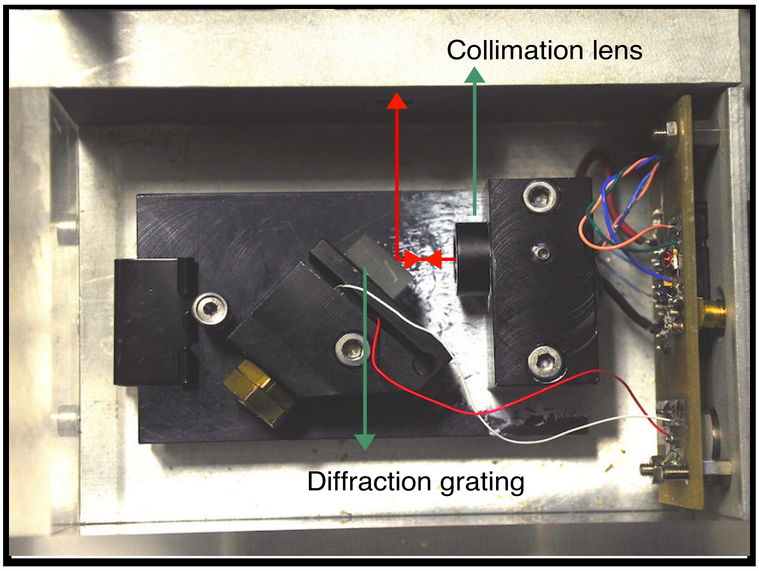

Figure 2.4: An External cavity diode laser (Littrow configuration) contains a collimating lens (Thorlabs C230) and a diffraction grating (Thorlabs 1800 lines/mm). The first-order diffracted beam provides optical feedback to the laser diode. The laser output power is taken from the zero-order reflection of the grating.

running diodes is ≈ 20 MHz. To narrow the linewidth further, we use a grating-stabilised extended cavity in a Littrow configuration (ECDL) [58] as shown in Figure 2.4. The external grating is aligned such that the first diffraction order of the light goes back into the diode to provide optical feedback to form an optical cavity. The zeroth order diffraction from the grating is used for the experiment. A piezo is attached to the grating to scan the frequency of the laser. The linewidth of the ECDL is estimated by performing a beat note measurements between the two independent lasers with slightly different frequencies. The linewidth of all ECDLs on our optical table is between 1 – 2 MHz.

The light emitted from the diodes has different divergence in the plane parallel and perpendicular to the emitting facet. To correct astigmatism, we use a pair of anamorphic prisms as shown in Figure 2.5. Any optical feedback back into the laser diode is suppressed by an optical isolator with 30–60 dB isolation.

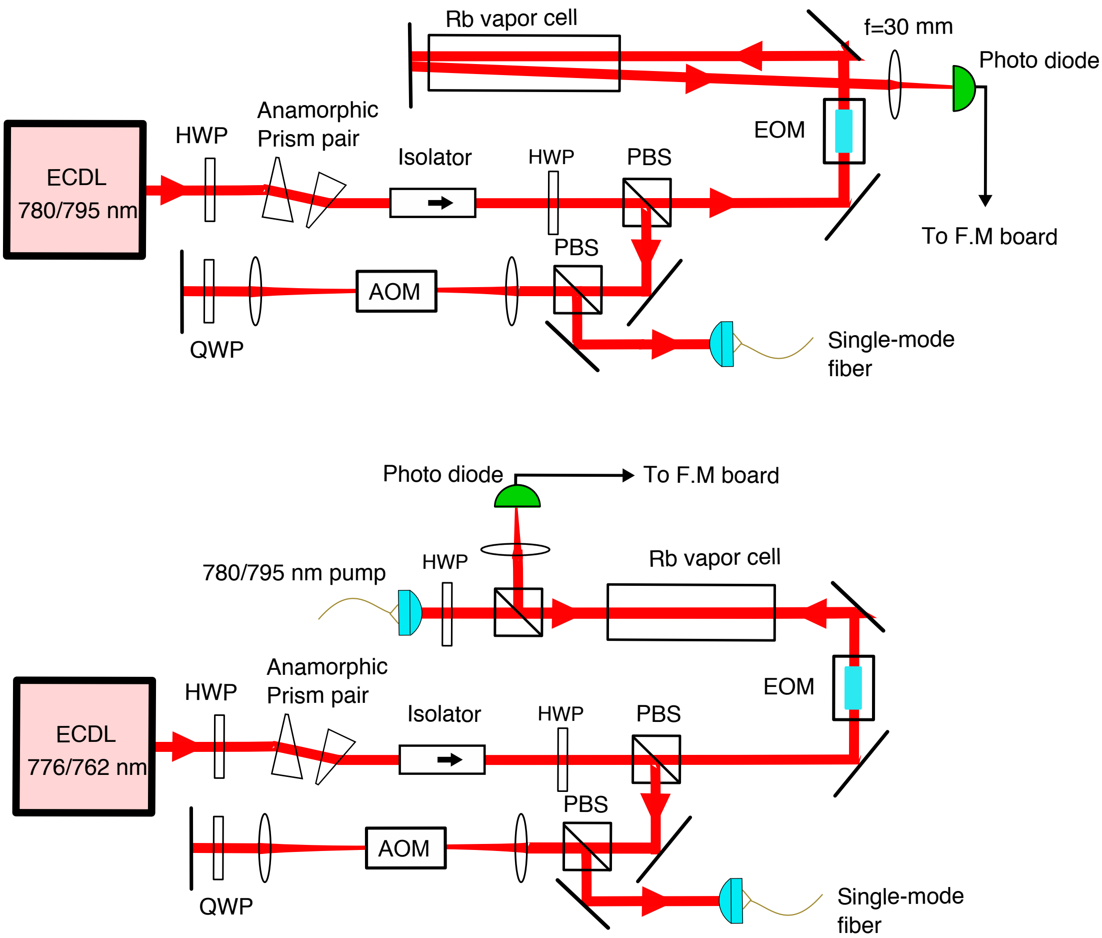

Figure 2.5: Schematic of Doppler-free saturation-absorption spectroscopy setup used for locking the frequency of ECDL. (Top) The optical setup used for the 780 nm and 795 nm lasers. (Bottom) The optical setup used for the 776 nm and 762 nm lasers. The details are explained in the text.

2.2.2.1 Frequency locking and tuning

We next lock the frequency of the lasers. The drifts in the frequency can be due to thermal variations, mechanical instabilities which can change laser cavity's length, laser driver current and others. The frequency of the lasers is locked to either the real or crossover lines of ^{87}Rb using frequency modulated (F.M) Doppler-free saturation-absorption spectroscopy [59, 60]. We apply frequency modulation to the light via an Electro-Optic-Modulator (EOM) in a tank circuit with a resonance frequency of 20 MHz. The RF signal at 20 MHz is supplied from a function generator which is distributed equally by a power splitter to all the EOMs on the optical table. The modulated beam is sent to the Rubidium vapour cell in a counterpropagating pump-probe geometry as shown in Figure 2.5 (Top). This is a well known technique [61] where a strong pump beam saturates the atomic transition and a counterpropagating weak, modulated probe beam acquires a phase shift when tuned across the atomic resonance. The change in phase shift is measured with a fast photodetector (Hamamatsu S5792). The detected signal is sent to a F.M demodulation circuit where frequency demodulation, error signal generation and locking with a proportional-integral-derivative (PID) control loop is performed. To perform spectroscopy at 776 nm and 762 nm, we first saturate the lowest energy optical transition of Rubidium with the pump beams derived from the 795 nm and 780 nm lasers respectively. With counterpropagating probe beams of wavelength 762 nm and 776 nm respectively, we address the higher excited transitions as shown in Figure 2.5 (Bottom). The error signals obtained for all the lasers is shown in Appendix A

Further fine tuning of the frequency of the lasers is done using Acousto-Optic Modulators (AOM) in a single pass or double pass configuration. The RF signal to drive the AOMs is produced by a home built Direct Digital Synthesiser (DDS).

The AOMs are also used as an optical switch to turn off the beams. We use a mini circuits switch (ZYSWA - 2 - 50 - DR, 60 dB extinction) to switch off the RF signal sent to the AOM. The first order diffracted beam from the AOM is coupled into single mode fibres and guided to the vacuum chamber. Single mode fibers also help to clean up the spatial mode of the beam.

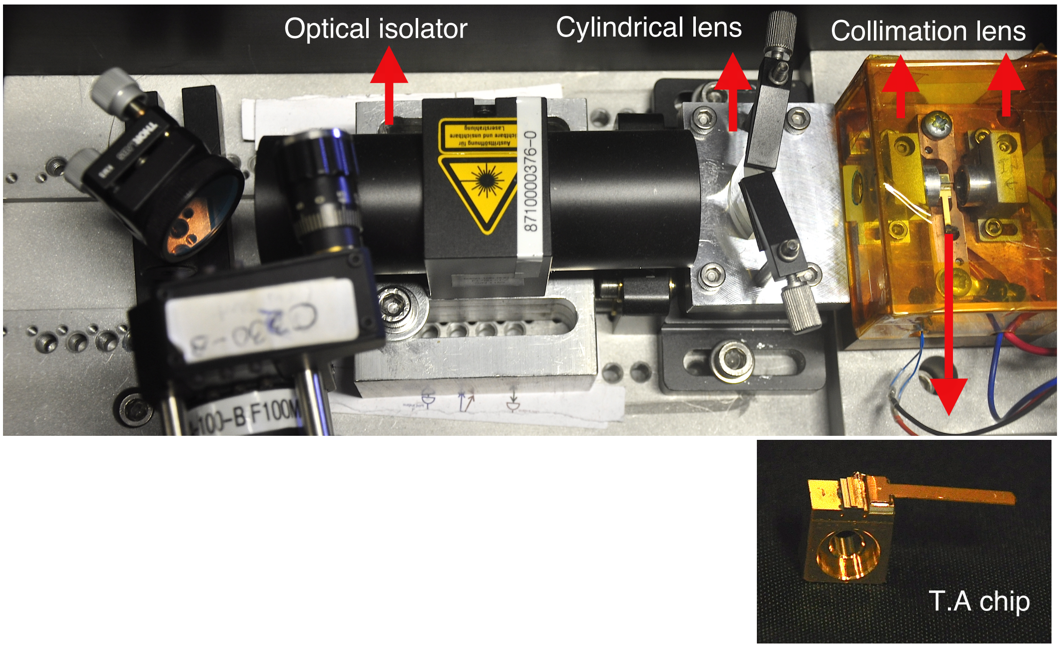

Figure 2.6: A Tapered Amplifier (T.A) kit with a T.A chip (Inset), aspheric lens, cylindrical lens and a 60 dB optical isolator.

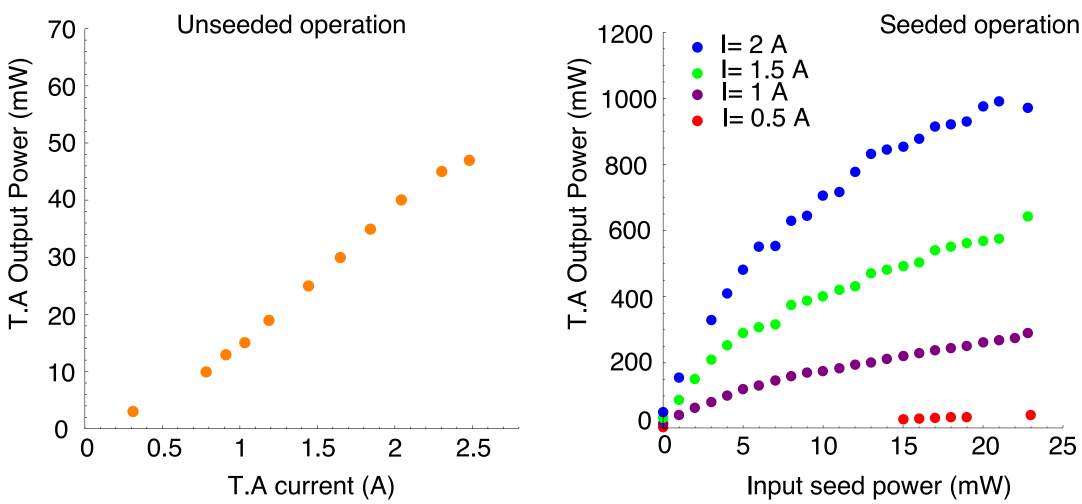

Figure 2.7: (Left) T.A output power as a function of current supplied to T.A chip during unseeded operation. (Right) T.A output power as a function of seed power for different operating currents.

2.2.3 Tapered Amplifier (T.A)

The number of atoms in the Magento-Optical Trap (MOT) strongly depend on the intensity of the cooling laser [62]. Therefore, more laser power is desired than can be produced by a single ECDL alone. We use an Eaglyard Tapered Amplifier (TA) chip (EYP-TPA-0780-01000-3006-CMT03-0000), seeded by an ECDL to achieve high power while retaining the narrow linewidth and stability of the ECDL. The basic structure and details of the T.A chip is described in [63]. A T.A chip consists of a short, ridge waveguide section which is coupled into a long gain guided tapered section. The chip is located on the top of a copper heat sink which sits on the top of large aluminium plate. Any temperature fluctuations will result in fluctuations in the power of the emitted light. We stabilise the temperature of the T.A chip using a home built temperature control unit. A thermistor fixed on the copper block monitors the temperature and the temperature controller supplies feedback current to the peltier element to match a manual set temperature within a 10 mK resolution. The unseeded output power from the T.A chip as a function of operating current is shown in Figure 2.7 (Left). We focus the seed beam (780 nm) into the input of the T.A chip using an aspheric lens (Thorlabs C170 (TME-B)) of focal length 6.16 mm. Another aspheric lens (Thorlabs C390 (TME-B)) of focal length 2.75 mm is used to collimate the divergent output from the TA chip. The astigmatism is corrected with a cylindrical lens of focal length of 50 mm. A 60 dB optical isolator (Thorlabs) is used to prevent optical feedback into the TA chip. The output optical power from the TA chip as a function of seed laser power for different operating currents is shown in Figure 2.7 (Right). In a seeded operation, the TA chip can emit a maximum power of 1 W. It is recommended to operate the T.A near the saturation region such that any power fluctuations in seed beam does not translate into fluctuations of the output power of the T.A.

2.3 Magneto-Optical Trap (MOT)

Once we had T.A, we next focussed on loading the atoms in a MOT. Photon pair generation via a FWM process has been demonstrated in hot atomic vapours [54, 56]. These systems inherently suffer from Doppler broadened atomic transitions. Therefore, the bandwidth of the generated photons is of the order of few hundreds of MHz. The problem can be solved by using cold atomic ensembles where a low temperature of

$\approx 100\,\mu$K or below can be achieved and Doppler broadening effects are significantly reduced. There are numerous laser cooling and trapping methods to produce cold atoms in the laboratory [64].

When an atom absorbs a photon, it receives a momentum kick in the propagation direction of the photon. If we use a laser beam red detuned from the atomic transition, then only a certain velocity class of atoms moving towards the laser beam will absorb the light due to Doppler effect. This results in a friction force to the atom. For cooling to occur, the atoms must be illuminated in all three direction by counter propagating laser beams. Magnetic trapping is created by adding a linear magnetic field gradient together with the red detuned optical field needed for laser cooling. This causes a Zeeman shift in the magnetic-sensitive m_F sub-levels, which increases with the radial distance from the centre (zero field point). Because of this, atoms moving away from the centre of the trap will see the atomic resonance to be shifted closer to the frequency of the laser light, and the more likely to receive a photon kick towards the zero field. The correct polarizations must be used so that photons moving towards the field zero point will be on resonance with the correct shifted atomic energy level. There is plenty of literature on the basics of cooling and trapping the atoms in a MOT [65, 66]. In this section we will just give a brief overview on the MOT setup used for our experiment.

As with all cold atom experiments, in order to ensure that the atoms are not heated by collisions with a background gas, we must work in an ultra-high vacuum. Our vacuum system consists of a vacuum chamber, a glass cuvette and an ion pump. We use a 2 l/s ion pump from Varian to continuously pump the vacuum chamber. The vacuum pressure in our chamber is around 1×10^{-9} mbar. A cuvette of dimensions 70 mm $\times$ 30 mm $\times$ 30 mm is attached to the vacuum chamber via a seal of indium wire with a low vapor-pressure epoxy. The cuvette is antireflection coated at 780 nm on the outer side. Rubidium vapor is evaporated into the chamber from a Rubidium getter (Alvatec) when heated above 200° C.

The MOT is formed at the intersection of six red detuned, circularly polarized cooling beams and a magnetic quadrupole field gradient with zero field at the point of intersection. The cooling beams are derived from a master ECDL coupled into the T.A chip as discussed in Section 2.2.3. The master laser is locked to a crossover between $5S_{1/2}, F = 2 \rightarrow 5P_{3/2}, F = 2$ and $5P_{3/2}, F = 3$. The frequency is shifted by a +190 MHz with a single pass AOM in the spectroscopy.

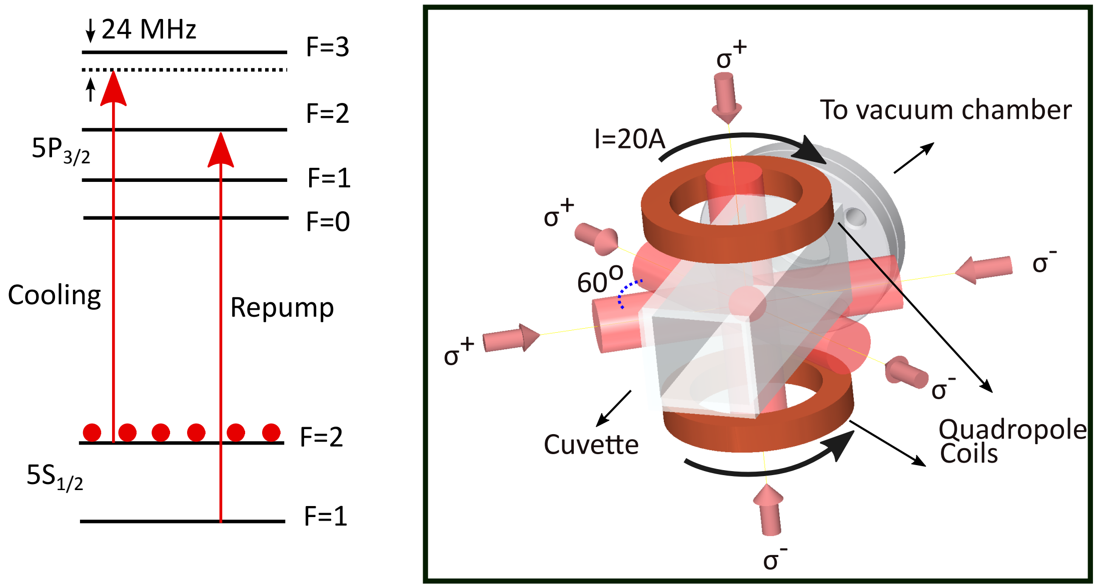

Figure 2.8: (Left) Hyperfine energy levels of ^{87}Rb with relevant transitions used for cooling the atoms is indicated. (Right) Magneto-Optical Trap set up: a glass cuvette attached to a vacuum chamber, quadruple coils and circular polarized beams used for cooling the atoms. The MOT is formed at the intersection of the cooling beams.

We couple another single pass AOM after the TA to shift frequency by -81 MHz such that we are 24 MHz red-detuned from the $5S_{1/2}$, $F = 2 \rightarrow 5P_{3/2}$, $F = 3$ transition. The power of each cooling beam is around 45 mW with a beam diameter $\approx$15 mm such that the intensity of each beam is more than 15 times the saturation intensity (I_s) of D2 transition ($I_s = 3.6\,\mathrm{mW\,cm^{-2}}$). Although much less likely, the finite detuning of cooling laser can transfer the atoms into $5P_{3/2}$, $F = 2$ level. When this happens, then with a certain probability atoms can also decay into $5S_{1/2}$, $F = 1$ level. Therefore after a few absorption-emission cycles, the cooling process stops. A repump laser, therefore, is necessary to excite the $5S_{1/2}$, $F = 1 \rightarrow 5P_{3/2}$, $F = 2$ transition in order keep the population of atoms in the $5S_{1/2}$, $F = 2$ level. The optical power of the repump laser used for the experiment is around 9 mW. The relevant transitions used for cooling the atoms in ^{87}Rb is shown in Figure 2.8 (Left).

The magnetic quadrupole field gradient is generated by a pair of coils carrying current in the opposite direction (Anti Helmohtz configuration). We use an enamel coated copper wires with a rectangular crossection wound with around 40 turns. With the quadruple current of 12 A to the coils, we can generate magnetic-field gradient of

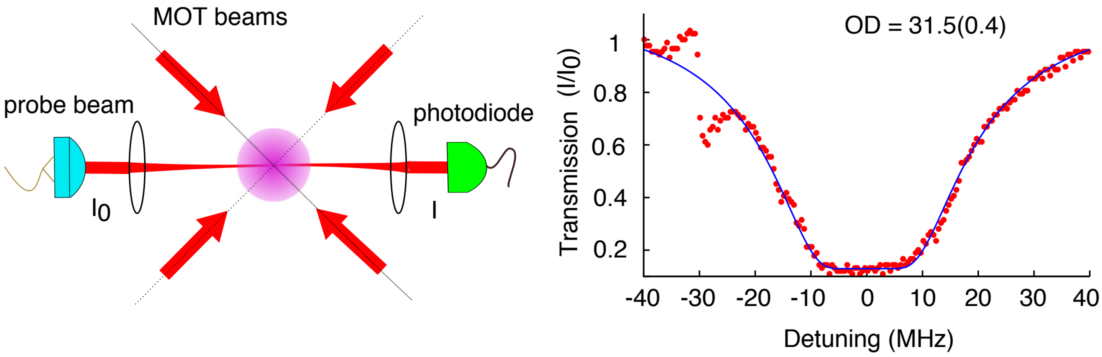

Figure 2.9: (Left) Setup to measure the optical density of the atomic cloud. The MOT beams are always ON during the measurement. (MOT beams perpendicular to the plane of paper are not shown). (Right) Transmission as a function of detuning from the $5S_{1/2}$, $F = 2 \rightarrow 5P_{3/2}$, $F = 3$ transition.

24.8 G/cm in the radial direction and 49 G/cm in the axial direction with this configuration.

2.3.0.1 Optical density of the cloud of atoms

The number of atoms collected in the MOT can be estimated by measuring the Optical density (OD) which is related to number of atoms as [67]

$$\mathrm{OD} = \frac{d^2 \omega\, N}{c\, \hbar\, \epsilon_0 A\, \gamma_0}\,, \tag{2.4}$$

where d is transition dipole moment, ω is the frequency of the laser, A is the cross-section of the beam and γ_0 is the natural linewidth of the transition, N is the total number of atoms. The experimental setup to measure the OD of the atomic cloud is illustrated in Figure 2.9 (Left). We measure the transmission of a probe beam after passing through the cloud of atoms. The probe beam is focused onto a spot size of 100 μm at the centre of the cloud and scanned across the resonance of $5S_{1/2}$, $F = 2 \rightarrow 5P_{3/2}$, $F = 3$ transition. The initial intensity of the probe I_0 should be lower than the saturation intensity of the transition. The intensity I of the probe after passing through the cloud can be written as a function of detuning as

$$I = bg\, +\, I_0 \exp\left(\frac{\mathrm{OD}\, \gamma_0^2}{4\,(\omega - \omega_0)^2\, +\, \gamma_0^2}\right) \tag{2.5}$$

where bg is the background signal in the absence of the probe beam, $\omega - \omega_0$ is the detuning of the probe beam frequency from the resonance of the transition ω_0, $\gamma_0 = 2\pi\times$ 6.06 MHz is the natural linewidth of the $5P_{3/2}$, $F = 3 \rightarrow 5S_{1/2}$, $F = 2$ transition [3]..

The measured transmission of the probe beam I/I_0 as a function of detuning is shown in Figure 2.9 (Right). We observe a drop in transmission as we approach near resonance as expected from Equation 2.5. At around $\omega - \omega_0 =$ 24MHz, we observe a sharp increase in the transmission of the probe beam. This can be explained with Electro-magnetic induced transparency effect [68]. Since the cooling beams are not switched off during the measurement, therefore, the strong cooling beams create a spectral window of transparency for the weak probe beam which reduces the absorption of probe beam by the atoms at this frequency. The OD estimated from the fit using Equation 2.5 is around 31.5±0.4.

2.4 Experimental set up and alignment procedure

The experimental setup is shown in Figure 2.10. Two pump beams of wavelength 780 nm and 776 nm are overlapped at an angle of 0.5° in a co-propagating geometry inside the cloud of atoms. We label them as pump1 and pump2 respectively. The pumps are resonant with the $5S_{1/2}$, $F = 2 \rightarrow 5P_{3/2}$, $F = 3$ and $5P_{3/2}$, $F = 3 \rightarrow 5D_{3/2}$, $F = 3$ transitions, respectively. As discussed in Section 2.1.1, for a given propagation direction of the pump beams, the phase matching condition will allow for the generation of signal and idler photon pairs into a well defined spatial modes. But with just two pump beams, it becomes tedious to search for the correct phase matched direction of the collection modes. Therefore, as an initial alignment step, we send a third seed beam of wavelength 795 nm inside the cloud. The seed beam is overlapped with 780 nm pump using a interference filter IF1 (Semrock laserline 780 nm, Full Width Half Maximum (FWHM) bandwidth 3 nm, peak transmission 96%).

The frequency of the seed beam is tuned to be resonant with the $5S_{1/2}$, $F = 2 \rightarrow$ $5P_{1/2}$, $F = 2$ transition. All the beams have Gaussian profiles with a waist of 0.45 mm, collimated using aspheric lens (Thorlabs C230-TMEB). The three coherent beams interact with the ensemble of atoms to generate a new coherent beam of wavelength 762 nm into the signal mode via a stimulated FWM process. We use interference filters IF2, IF3 to separate the pumps from the collection mode. In this configuration, the 762 nm light

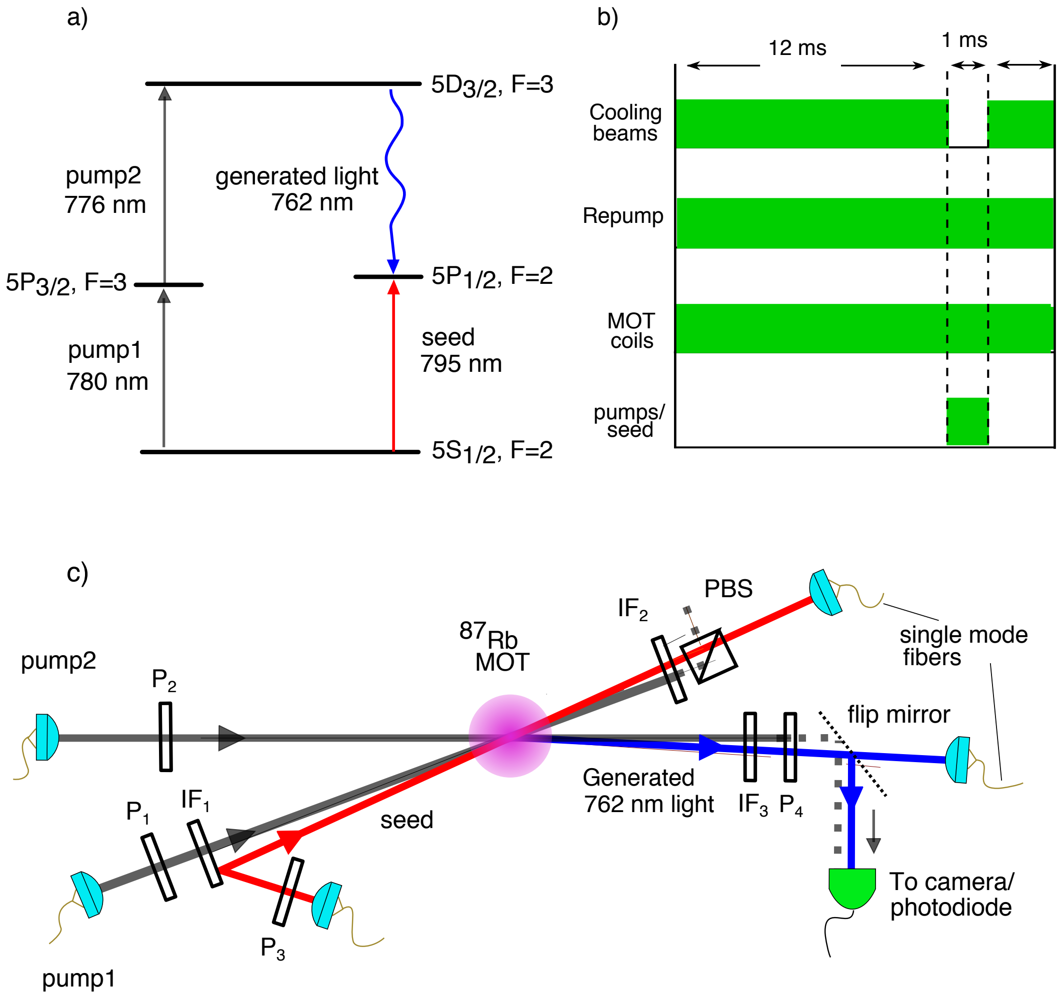

Figure 2.10: a) Cascade level scheme for four wave mixing in ^{87}Rb. b) Timing sequence of the experiment. c) Schematic of the experimental setup: (An alignment step before the photon pair generation). Pump1, Pump2 and seed beams are overlapped inside the cloud. The coherent beam at 762 nm is generated into the signal mode via stimulated FWM process. IF1, IF2, IF3 are interference filters and P(1-4) are polarizers

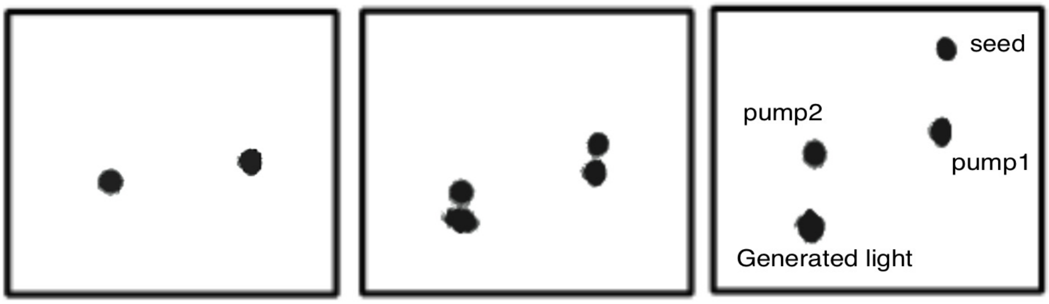

Figure 2.11: Camera images to illustrate phase matching condition. When the seed beam is overlapped with pump1, the generated light is overlapped with pump2. As we gradually increase the angle between seed and pump1, the separation between pump 2 and generated light also increases to satisfy the phase matching condition.

is generated along the direction of the pump2. Figure 2.11 demonstrates a neat illustration of phase matching condition. We observe that, as we gradually increase the angle between the seed beam and pump1, the separation between the generated light and the pump2 also increases to satisfy phase matching condition. The spectrum of the generated light is measured using a grating spectrometer (Ocean optics - USB2000) shown in Figure 2.12. The polarization of the pump beams, seed and generated light were chosen to maximize the power of the generated light. Table 2.1 illustrates the power of generated light with different combination of polarization of the pump1, pump2, seed and the generated light. With an optical power of pump1 $= 100\mu$W, pump2 $=$ 5 mW, seed $=$ 1 mW, we measure 83 nW of the generated 762 nm light into a signal mode fiber.

2.4.1 Timing sequence

The timing sequence of the experiment is controlled by a pattern generator. A host computer sends a series of commands (timing sequence) to the pattern generator that outputs a sequence of electrical signals (TTL or NIM) to control the rest of the devices in the setup. The timing sequence used in the experiment is shown in Figure 2.10 (b). We choose a 12 ms time window during which the cooling beams are on, interleaved with a 1 ms long generation time window where pump and seed beams are on.

The duty cycle was found to give a maximum optical density of the MOT. The repump laser is kept on all the time to continuously optically pump the atoms into $5S_{1/2}$, $F = 2$ level.

pump1 polarization	pump2 polarization	seed polarization	generated light polarization	generated light power (nW)
H	H	H	H	30.2
H	H	V	V	7.8
V	H	H	V	80
V	H	V	H	7.8
H	V	V	H	83
V	V	V	V	30

Table 2.1: Polarization of pump1, pump2, seed, generated light and power of generated light. Horizontal polarization is labelled as $|H\rangle$ and vertical is $|V\rangle$

.

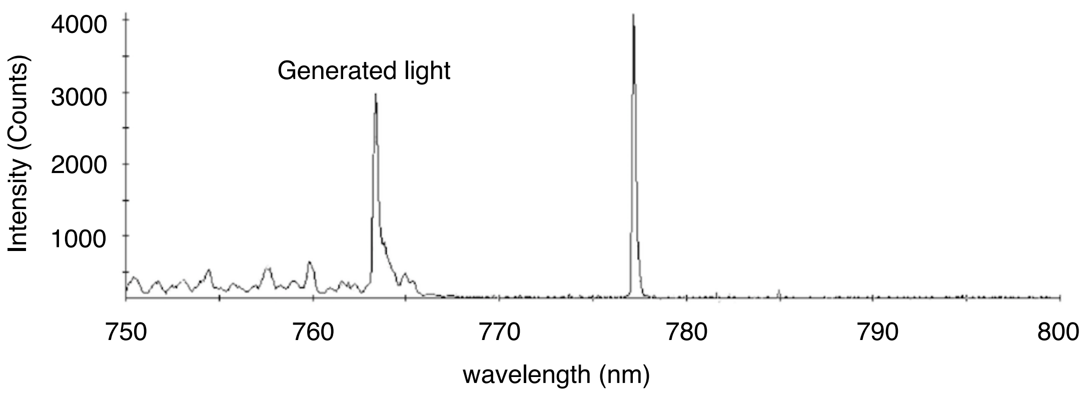

Figure 2.12: The wavelength of the generated light measured with a USB spectrometer of +1 nm offset. The peak on the left is the generated 762 nm light in FWM process and the peak on the right is the pump2 (776 nm) leaking into the collection modes.

We couple the seed beam and the light generated by the FWM process into signal mode fibers with a coupling efficiency of 70% and 80% respectively using aspheric lenses (Thorlabs A375-TMEB). The effective waists of the collection modes at the location of the cold cloud were determined to be 0.4 mm and 0.5 mm for the signal and idler by back-propagating the light through the fibers and couplers. After the source is aligned, we block the seed beam, and only the parametric fluorescence is coupled into the collection fibers and sent to APDs. The details regarding photon pair generation and detection is discussed in Chapter 3.

Chapter 3

Narrowband time correlated photon pairs

In this Chapter we will present a bright and narrowband source of photon pairs based on four wave mixing process in a cold cloud of ^{87}Rb atoms. We first describe the experimental setup. This is followed by the characterization of the temporal properties of the generated photon pairs via a cross correlation measurement that provide an evidence of the superradiance effect. The quality of the source is assessed by measuring total pair detection rates, accidental rates and heralding efficiencies. The bandwidth of the generated photons is measured with a Fabry-Perot cavity. A merit comparision between the directly measured bandwidth and that inferred from the characteriztic decay time ($1/e$) of the cross correlation function indicates a Fourier transform limited spectrum of the generated photons. We also perform a Hanbury-Brown-Twiss measurement individually in the signal and idler modes. The results reveal the thermal nature of light from both conversion modes.

3.1 Introduction

The DLCZ protocol allows for the implementation of quantum communication over long distance using atomic ensembles [30]. The idea of effectively storing photonic qubit into an atomic ensemble based quantum memory, motivated the search for methods for generating narrowband correlated photons. For decades, parametric downconversion in non-linear crystals and waveguides has been a standard method to generate time correlated photon pairs. In the recent years many other nonlinear materials [45, 46] are being explored for the efficient pair production. Although extremely robust [34], they exhibit a relatively wide optical bandwidth ranging from 0.1 to 2 THz [31, 32]. This makes it difficult to interact with atomic systems, since their optical transitions usually have a lifetime-limited bandwidth on the order of several MHz. An alternative approach is to use nonlinearities in the atoms. Near resonant four wave mixing (FWM) in hot atomic vapours [37, 55] and in cold ensembles [38] has been shown to produce photon pairs that are inherently narrowband. We generate photon pairs via FWM in a cold cloud of atoms provided by a Magneto-Optical Trap (MOT).

3.2 Experimental setup

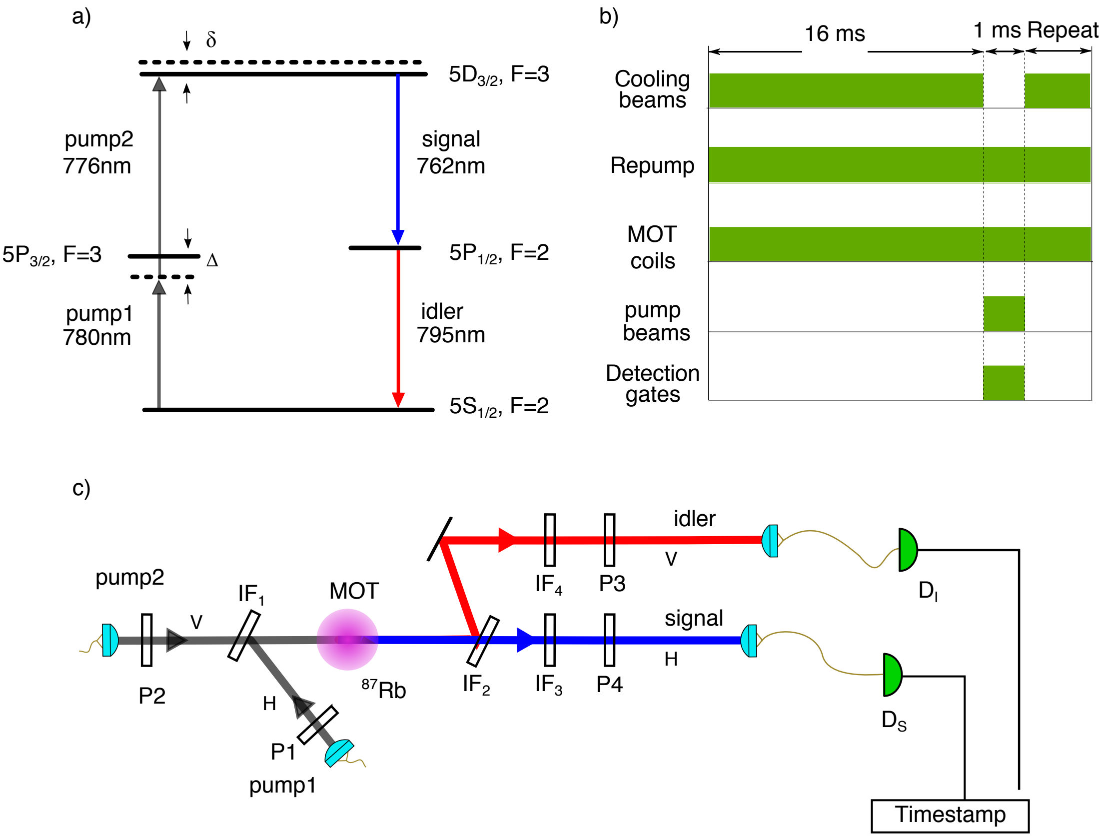

Figure 3.1: (a) Cascade level scheme used for parametric conversion in atoms. (b) Timing sequence of the experiment. (c) Schematic of the experimental set up, with P1, P2, P3 and P4: Polarization filters, IF_1, IF_2, IF_3, IF_4: interference filters, $\mathrm{D_I}$, $\mathrm{D_S}$: avalanche photodetectors.

The experimental setup is shown in Figure 3.1.[1] The pumps beams of wavelength 780 nm (pump1) and 776 nm (pump2) excite the atoms from $5S_{1/2}, F = 2$ to $5D_{3/2}$, $F = 3$ via a two-photon transition. The 780 nm pump beam is red detuned by $\Delta = 60$ MHz from the intermediate level $5P_{3/2}$, $F = 3$, since its population would result in a decay back to the initial state. Photon pairs from a cascade decay of atoms in the excited $5D_{3/2}, F = 3$ level via $5P_{1/2}, F = 2$ back into the $5S_{1/2}, F = 2$ emerge into well-defined directions determined by momentum conservation of the four participant modes. Using all four modes in a collinear geometry makes the alignment simpler and allows for an efficient coupling of the generated photons into a single mode fiber. An interference filter (IF_1) (Full Width Half Maximum (FWHM) bandwidth 3 nm, peak transmission 96%) combines the two pump beams in a co-propagating geometry inside the cloud. The signal (762 nm) and idler (795 nm) photons are separated from the residual pump light by the interference filters (IF_2, IF_3, IF_4). Uncorrelated photons are further removed from the collection modes by polarizers P_1 and P_2. The polarization of the pump beams and the photons are chosen from the Clebsch-Gordan coefficients to maximize the effective nonlinearity [69]. Parametric fluorescence is then coupled into single mode fibers with aspheric lenses[2]. The photons are detected with silicon avalanche photodetectors (APDs) D_I and D_S, (estimated quantum efficiencies of $\approx 40\%$, dead time $\approx 1\,\mu$s) and their arrival time is recorded by a timestamp unit. The combined timing uncertainty of the detectors and timestamp unit is about 0.6 ns.

The timing sequence used in the experiment is shown in the Figure 3.1. We choose 16 ms time window for cooling, interleaved by 1 ms window for photon pair generation. We electronically gate the APDs such that only photon counts during the 1 ms of pair generation time are registered by the timestamp unit.

The power of the pump beams and detuning from the two photon resonance (δ) have a substantial effect on the generation rates and efficiency of the source. Their values are changed according to the measurement as will be discussed in rest of this Chapter.

[1] The set up is similar to that described in Chapter 2, Section 2.4 but the geometry of the pump beams is different.

[2] Alignment procedure is described in Chapter 2, Section 2.4

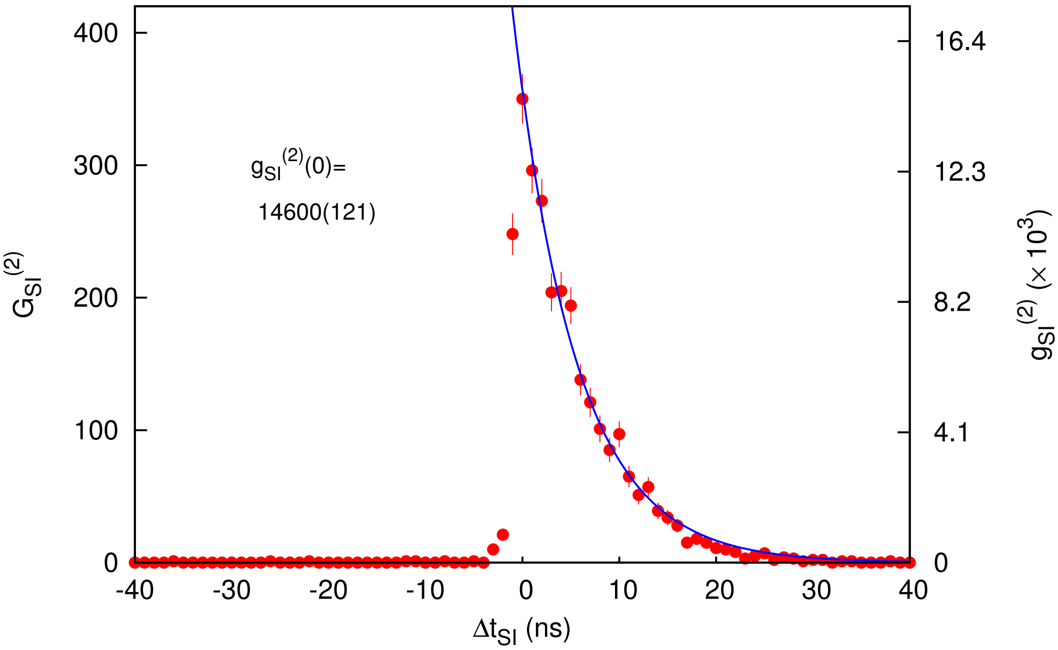

Figure 3.2: Histogram of coincidence events $G^{(2)}_{\mathrm{SI}}(\Delta t_{\mathrm{SI}})$ as a function time difference between the detection of signal and idler photons for an integration time $T = 42\,\mathrm{s}$ and its normalised version $g^{(2)}_{\mathrm{SI}}(\Delta t_{\mathrm{SI}})$. The solid line is a fit to the model $g^{(2)}_{\mathrm{SI}}(\Delta t_{\mathrm{SI}}) = B + A \times \exp(-\Delta t_{\mathrm{SI}}/\tau_0)$, where $B = 1.06 \pm 0.01$ is the mean $g^{(2)}_{\mathrm{SI}}(\Delta t_{\mathrm{SI}})$ for Δt_{SI} from 125 ns to 1μs, resulting in $A = 14600 \pm 121$ and $\tau_0 = 6.52 \pm 0.04\,\mathrm{ns}$.

3.3 Background

The nature of a light source can be uniquely characterized by its coherence properties, which is usually measured by a second-order coherence [70]. For a classical light source, a second-order correlation function $g^{(2)}(\tau)$ can be expressed in terms of intensity fluctuations at two different times separated by a time delay τ as

$$g^{(2)}(\tau) = \frac{\langle I(t)\, I(t+\tau)\rangle}{\langle I(t)\rangle\, \langle I(t+\tau)\rangle}\,, \tag{3.1}$$

where $\langle ... \rangle$ denotes the time average. However, in the quantum world, we no longer deal with the large beam intensities but with clicks on single photon detectors. Therefore, instead of looking at the instantaneous intensity $I(t)$, we must re-write the correlation function in terms of the photon number distribution as

$$g^{(2)}(\tau) = \frac{\langle n_i(t)\, n_i(t+\tau)\rangle}{\langle n_i(t)\rangle \langle n_i(t+\tau)\rangle}, \tag{3.2}$$

where $n_i(t)$ are the number of clicks on detector i at time t. In case of the coherent light source, the mean number of photons per unit time must be constant (with a completely random arrival time) and thus the time between detector clicks will follow a Poissonian distribution with $g^{(2)}(\tau) = 1$. Any light source with $g^{(2)}(0) > 1$, exhibits a super-Poissonian photon statistics and the light is said to be bunched. This is a unique charactersitic of a photon pair source.

3.4 Time correlation measurement

We measure coincidences between the arrival times of generated signal and idler photons on the APDs, D_I and D_S. The histogram of coincidence events $G^{(2)}_{SI}(\Delta t_{SI})$ as a function of time delay (Δt_{SI}) between the detection of signal and idler photons sampled into time bins of width Δt_B=1 ns is shown in Figure 3.2.

It is possible for two uncorrelated single photons to arrive at the detectors (D_S and D_I) within time bin interval. This causes them to be registered as a coincidence event when they are in reality not. These events are referred to as accidental coincidences. Therefore, we normalise $G^{(2)}_{SI}(\Delta t_{SI})$ with the accidental coincidences rate. The normalized second order intensity cross-correlation function [70] is defined as

$$g^{(2)}_{SI}(\Delta t_{SI}) = \frac{G^{(2)}_{SI}(\Delta t_{SI})/T}{r_I\, r_S\, \Delta t_B}, \tag{3.3}$$

where $T = 42$ s is the integration time during which the pump beams are on (see Figure 3.1 (b)), i.e., 1/17 of the total measurement time. The idler and signal singles rates (Total clicks on D_I and D_S during the time T) are r_I=535 s^{-1} and r_S=1042 s^{-1}. This results in an accidental coincidence rate $r_A = r_I\, r_S\, \Delta t_B = 5.5 \times 10^{-4}\,\mathrm{s}^{-1}$. We observe a peak at $g^{(2)}_{SI}(0)$ of 14600(121), indicating a strong correlation in the arrival times of signal and idler photons. The value of $g^{(2)}_{SI}(\Delta t_{SI})$ reaches 1.06±0.01 in a time interval from 125 ns to 1 μs, showing coincidence events within this time interval are random. The pump powers at 780 nm and 776 nm are $P_{780} = 450\,\mu$W and $P_{776} =$ 3 mW respectively. The combined frequency of the pumps ($\omega_1 + \omega_2$) from the resonance frequency of two photon transition (ω_0) is $\delta = (\omega_1 + \omega_2) - \omega_0 = 12$ MHz, blue-detuned for this measurement. The detunings and power of the pumps are optimised to obtain a maximum value of $g^{(2)}_{\mathrm{SI}}(0)$.

From the coincidence histogram we can also extract information about the coherence time of the heralded idler photons and quality of the photon pair source. The details are discussed in the Sections 3.5 and 3.6.

3.5 Coherence time (τ_0) of heralded idler photons

Time-correlated photon pairs can be used as a source of heralded photons: the detection of a signal photon heralds the presence of a photon in the idler mode [42, 71]. We define this photon in the idler mode as a heralded idler photon. In our cascade level scheme photon pairs are generated with a well defined time order: the signal photon is always generated before the idler photon. Therefore, the correlation function shows an asymmetric shape with a fast rise and a long exponential decay as shown in Figure 3.2. The rise time is limited by the jitter time of the APDs [72]. For an atomic cloud of optical density (OD) of 32, the measured $1/e$ decay time (τ_0) of the heralded idler photons from the fit is 6.52 ± 0.04 ns, which is lower than the single atom spontaneous decay time of 27 ns from the $5\mathrm{P}_{1/2}, F = 2 \rightarrow 5\mathrm{S}_{1/2}, F = 2$ transition. This is due to superradiance effects in an optically thick atomic ensemble.

3.5.1 Superradiance

Superradiance is the collective spontaneous emission from an optically thick atomic ensemble and was first discussed by Dicke in 1954 [73]. The first experimental observation of superradiance was in the 1970s from extended ensembles [74, 75] where they described superadiance as enhanced emission into a particular mode, and is strongly dependent on the relative spatial phases of the atoms in the ensemble. However, recently [76] the connection of superradiance with a photon pair generation process was discussed which supports the creation of a DLCZ–type collective superposition state [30]. We will briefly discuss superradiance effects in a cold ensemble using a cascade level scheme along with our experimental results. A more detailed theoretical description of superradiance in cascade level schemes can be found in [2] and is out of the scope of this thesis.

3.5.1.1 Theory

The generation of photon pairs from an optically thick atomic ensemble is a collective phenomenon due to radiative coupling between the atoms. The ^{87}Rb atoms, initially prepared in the ground state $|g\rangle$ ($5S_{1/2}, F = 2$), undergo a collective excitation to state $|e\rangle$ ($5D_{3/2}, F = 3$) by pump1 and pump2. The subsequent emission and detection of a photon in the signal mode heralds the preparation of a collective state of the form

$$|1\rangle = \frac{1}{\sqrt{N}} \sum_{i=1}^{N} e^{i\,(\vec{k_1}+\vec{k_2}-\vec{k_s})\vec{r_i}} |g\rangle_1 |g\rangle_2 \ldots |d\rangle_i \ldots |g\rangle_N, \tag{3.4}$$

where k_1, k_2 and k_s are the k vectors of pump1, pump2 and the signal photon fields, r_i is the position of the ith atom. The summation is over the number of atoms N. The collective state is a superposition of all possible states with $N - 1$ atoms in $|g\rangle$ and one atom in the intermediate state $|d\rangle$ ($5P_{1/2}, F = 2$) but it is unknown which atom. Consequently, in the low excitation regime, the detection of a photon in the signal mode projects the ensemble into a collective state with a single excitation shared among all the atoms in the ensemble as shown in Equation 3.4. The position dependent phase factor arises from the phase-matching condition. The phase correlation between the atomic dipoles results in constructive interference, resulting in a superradiant emission of the idler photon into a well defined mode. Emission of the idler photon marks the end of the process with all atoms decaying back to the initial ground state $|g\rangle$.

3.5.1.2 Results

The superradiant emission from an ensemble of atoms is a coherent process. It exhibits two characteristic features that differentiate it from incoherent emission:

- The peak intensity (peak pair rate) in a superradiant emission increases quadratically with the number of atoms N, while in the case of incoherent emission, it increases linearly with N [77].
- Atoms in the excited state collectively decay into the ground state with a decay time $\tau_0 = \frac{\tau_{sp}}{1+\mu N}$, much faster than spontaneous emission decay time τ_{sp} from a single atom. The geometric factor μ depends on the size of the cloud [2]

We observe the two characteristic features of superradiance in our experiment. We use the optical density of the cloud (OD) as a measure of the number of atoms N in

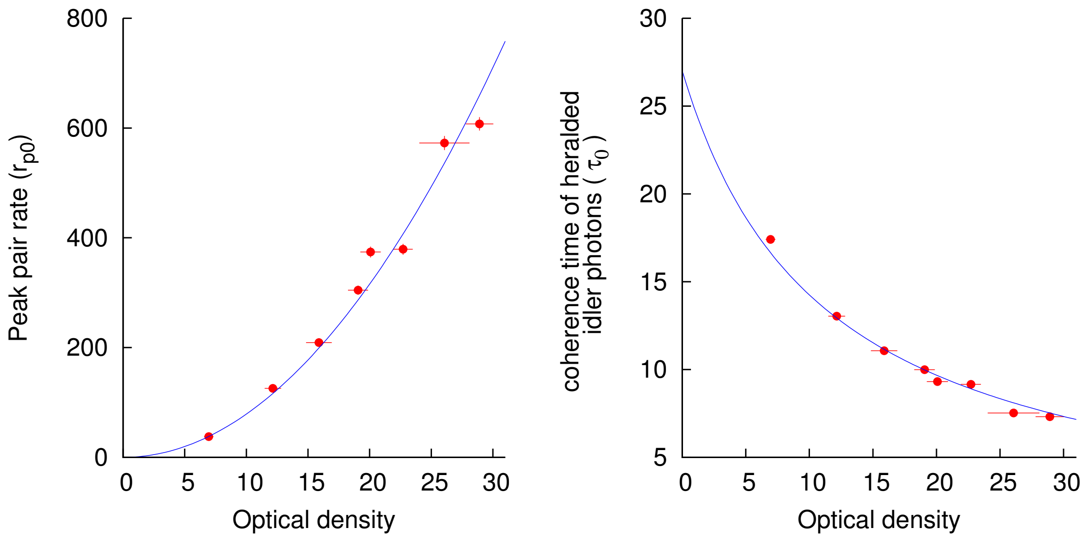

Figure 3.3: (Left) Plot of peak pair rate r_{p_0} (coincidence rate within 1 ns of the detection of the signal photon) as a function of the optical density (OD) of the atomic cloud. The line is a fit of the form $r_{p_0} = \alpha\,\mathrm{OD}^2$ where α is a proportionality constant. (Right) Plot of the coherence time of heralded idler photons (τ_0) as a function of OD of the cloud. The blue line is a fit to theoretical model of the form $\tau_0 = \frac{\tau_{sp}}{1+\mu\mathrm{OD}}$ with a proportionality factor between OD and N.

the cloud (see Equation 2.4). We vary the repump laser power to change OD. The peak pair rate (r_{p_0}) is defined as coincidence rate within 1 ns of the detection of the signal photon. In Figure 3.3 (Left), we see that r_{p_0} does increase quadratically with the OD (with a proportionality factor between OD and N). We also measure decay time constants from the fit of the cross correlation function $g^{(2)}(\Delta t_{\mathrm{SI}})$ and observe a shorter decay time as OD increases as shown in Figure 3.3 (Right)

3.6 Quality of the photon pair source

The quality of the photon pair source can be quantified from its

- Useful pair rate r_p: This rate can be obtained by subtracting accidental coincidence rate r_a from total coincidence rate R_p between the generated signal and idler photons.

- Efficiency: Useful pairs to singles ratio;

r_p

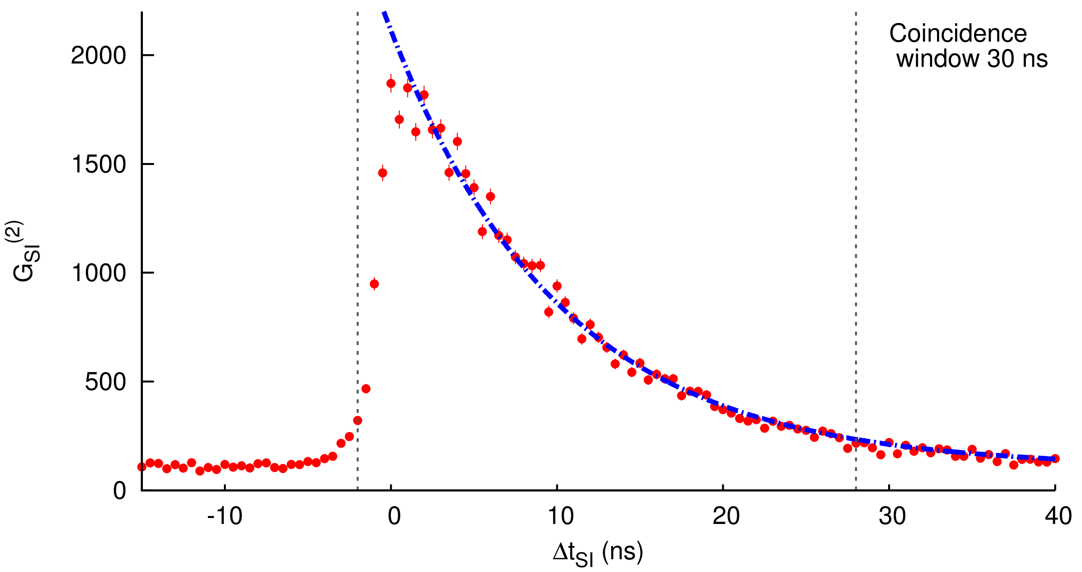

Figure 3.4: Histogram of coincidence events $G_{\mathrm{SI}}^{(2)}(\Delta t_{\mathrm{SI}})$ as a function of the time difference between the detection of signal and idler photons. The pump beam parameters are optimised to maximise the pair rates. The vertical dotted lines denote the coincidence time window chosen to capture almost all the pairs.

- Accidentals: Contribution of random coincidences to the total coincidences.

In the following subsections, we will address these three items briefly.

3.6.1 Total Pair detection rate

The total pair detection rate R_p of this source can be derived from the measured $G^{(2)}(\Delta t_{\mathrm{SI}})$ by integrating over a coincidence time window τ_c, $R_p = \frac{1}{T}\sum_{\tau=0}^{\tau_c} G_{\mathrm{SI}}^{(2)}(\tau)$. We choose $\tau_c = 30\,\mathrm{ns}$ (vertical lines in Figure 3.4), such that more than 98% of the pairs are captured. We further subtract the accidental rate r_A from R_p to obtain useful pair rate r_p. Under optimal experimental conditions with pump powers of $P_{780} = 290\,\mu\mathrm{W}$, $P_{776} = 14\,\mathrm{mW}$ respectively, detuning $\Delta \approx 60\,\mathrm{MHz}$ from the intermediate level and a two photon resonance detuning $\delta \approx 5\,\mathrm{MHz}$, we obtain $r_p = 20,000 \pm 141\,\mathrm{s}^{-1}$ during the parametric conversion interval (with integration time T=4 s). This value is uncorrected for losses due to non-unit detector efficiency, filtering efficiency and fiber coupling efficiency. Our rates exceed the values reported from similar experiments in

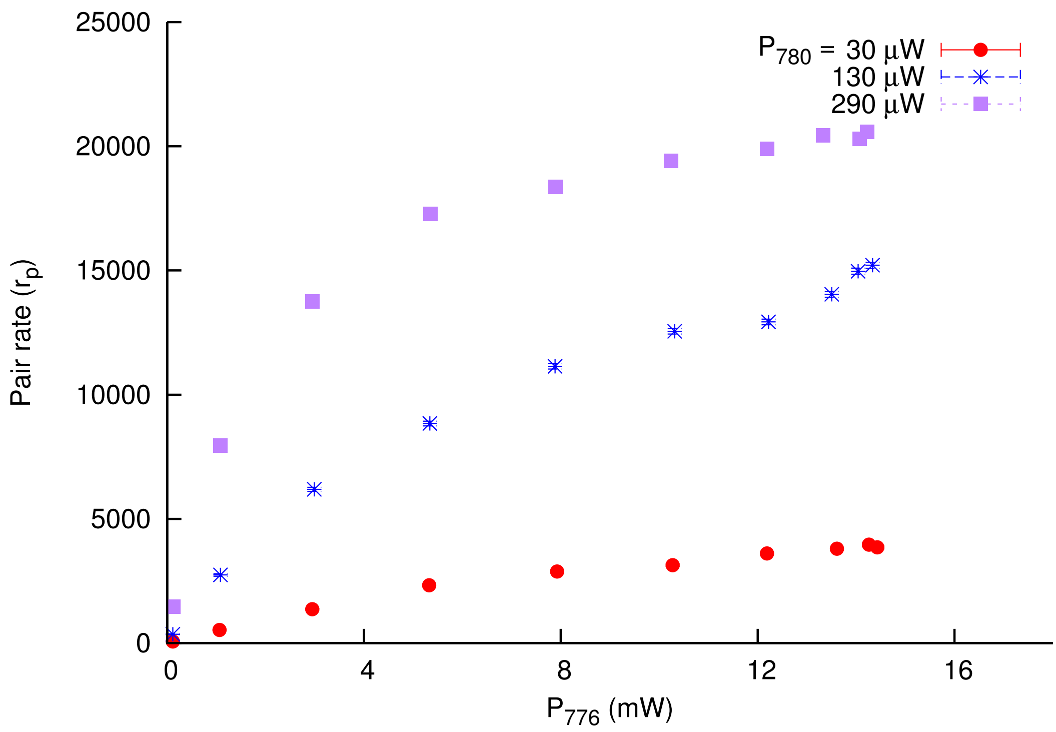

Figure 3.5: Plot of pair rates r_p as a function of pump power at 776 nm for three different pump powers at 780 nm. The vertical error bar on each point is smaller than the size of the data points.

atoms by Balič *et al.* ($r_p = 12{,}000\,\mathrm{s}^{-1}$ in cold atoms [78]), Willis *et al.* ($r_p = 1500\,\mathrm{s}^{-1}$ in hot vapours, [55]), Ding *et al.* ($r_p = 280\,\mathrm{s}^{-1}$ in hot vapours [37]). However, in an another experiment based on cold atoms in an optical cavity, the authors reported $r_p = 50{,}000\,\mathrm{s}^{-1}$ [28][1]

We also vary P_{776} and observe the change in r_p for three different P_{780} as shown in Figure 3.5. For low value of P_{776}, we observe a linear increase in r_p. With a further increase in P_{776}, the increase in r_p slows down and reaches a plateau which could be due to saturation of the two photon transition.

[1]The authors did not mention if the reported rates are before or after corrected for the losses.

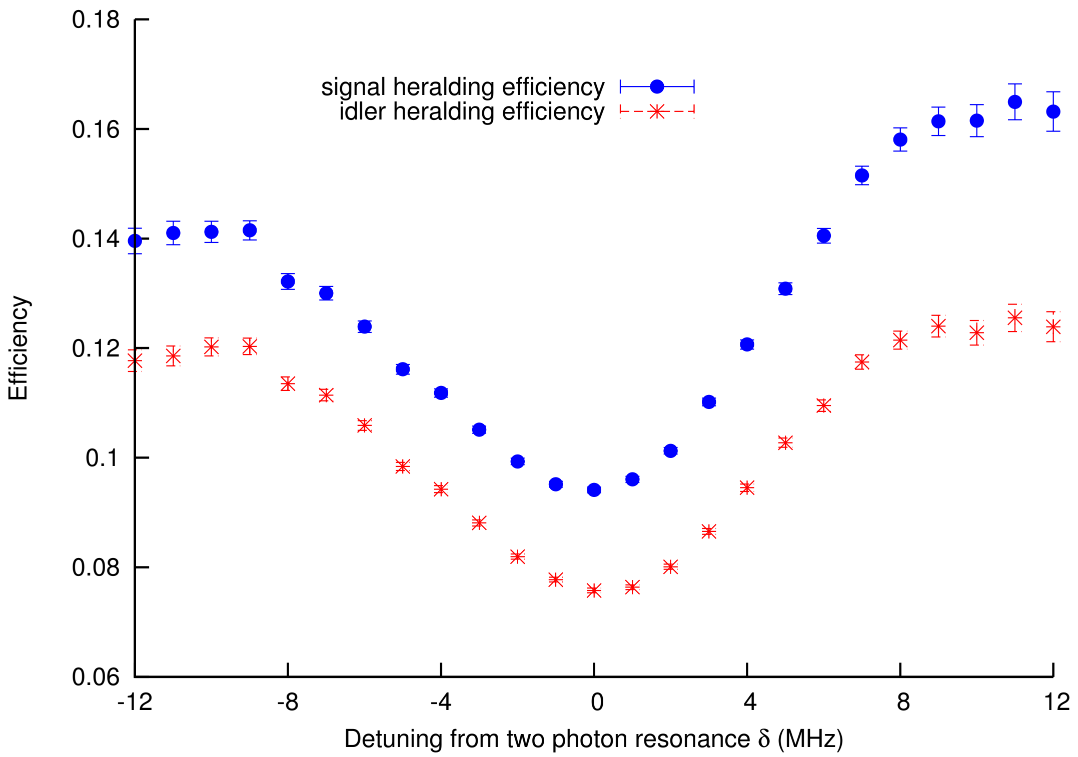

Figure 3.6: Efficiency of the source as a function of the detuning from the two photon resonance δ.

3.6.2 Efficiency

The efficiency of our photon pair source is measured independently for the signal and idler modes as the single rates is different in both modes. The measurement is performed with $P_{780} = 420\,\mu$W and $P_{776} = 15\,$mW. The detuning from the two photon resonance is $\delta \approx 12\,$MHz to the blue. Under these conditions, we find a signal heralding efficiency $\eta_{\rm S} = r_p/(r_{\rm S} - d_{\rm S}) = 17\%$, and an idler heralding efficiency $\eta_{\rm I} = r_p/(r_{\rm I} - d_{\rm I}) = 13\%$, where $d_{\rm I} = 520\,s^{-1}$ and $d_{\rm S} = 200\,s^{-1}$ are the dark counts/background count rates on the detectors in idler and signal mode, $\rm D_I$ and $\rm D_S$ respectively. The dark counts/background counts are spurious counts due to electrical, thermal or optical noise and are measured by blocking the light from the pumps and cooling beams.

We investigate the dependence of efficiency on the detuning from the two photon resonance δ as shown in Figure 3.6. We observe a drop in efficiency as we approach the resonance ($\delta = 0$), which we attribute to an increase in incoherent scattering from the

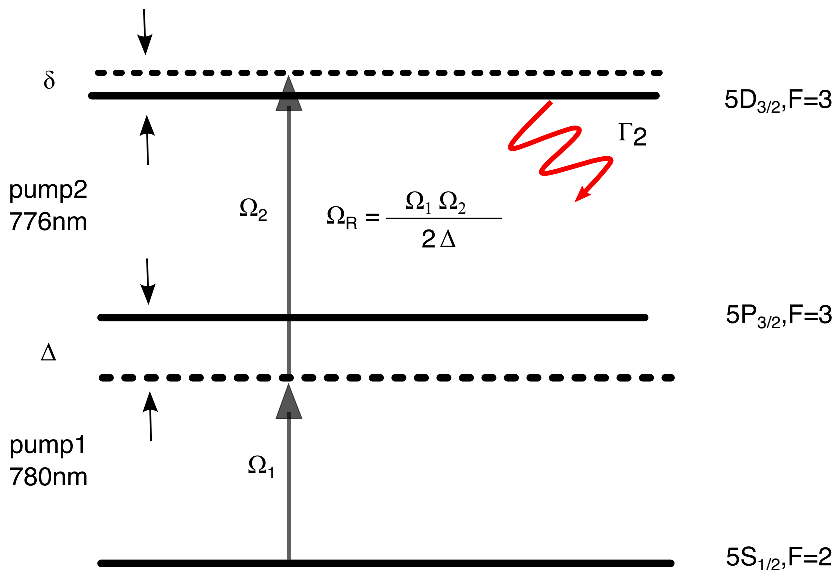

Figure 3.7: Level scheme illustrating the following quantities: Ω_1 and Ω_2 denoting Rabi frequencies of the individual two level transitions, Δ is the detuning from the resonance frequency of $5S_{1/2}$, $F = 2 \rightarrow 5P_{3/2}$, $F = 3$ transition, δ is the detuning from the two photon resonance.

atoms as we approach near the two photon resonance. According to Refs [79, 80], the intensity of the light due to coherent (I_{coh}) and incoherent scattering (I_{incoh}) from the atoms can be expressed as

$$I_{coh} = \frac{1}{2}\frac{s}{(1+s)^2}\,, \tag{3.5}$$

and

$$I_{incoh} = \frac{1}{2}\frac{s^2}{(1+s)^{\,2}}\,, \tag{3.6}$$

where s is the saturation parameter which is related to δ as

$$s = \frac{\frac{\Omega_R^2}{2}}{\delta^2 + \frac{\Gamma_2^2}{4}}\,, \tag{3.7}$$

where $\Omega_R = \frac{\Omega_1 \Omega_2}{\Delta}$ is the two-photon Rabi frequency, Ω_1, Ω_1 are the single photon Rabi frequencies [67] and Γ_2 is the spontaneous decay rate from $5D_{3/2}$ level as shown in Figure 3.7. As mentioned in Section 3.5.1, the photon pair generation is due to coherent scattering of photons from the atoms (superradiant emission). However, the total singles in each mode is given by a statistical mixture of coherent superradiant

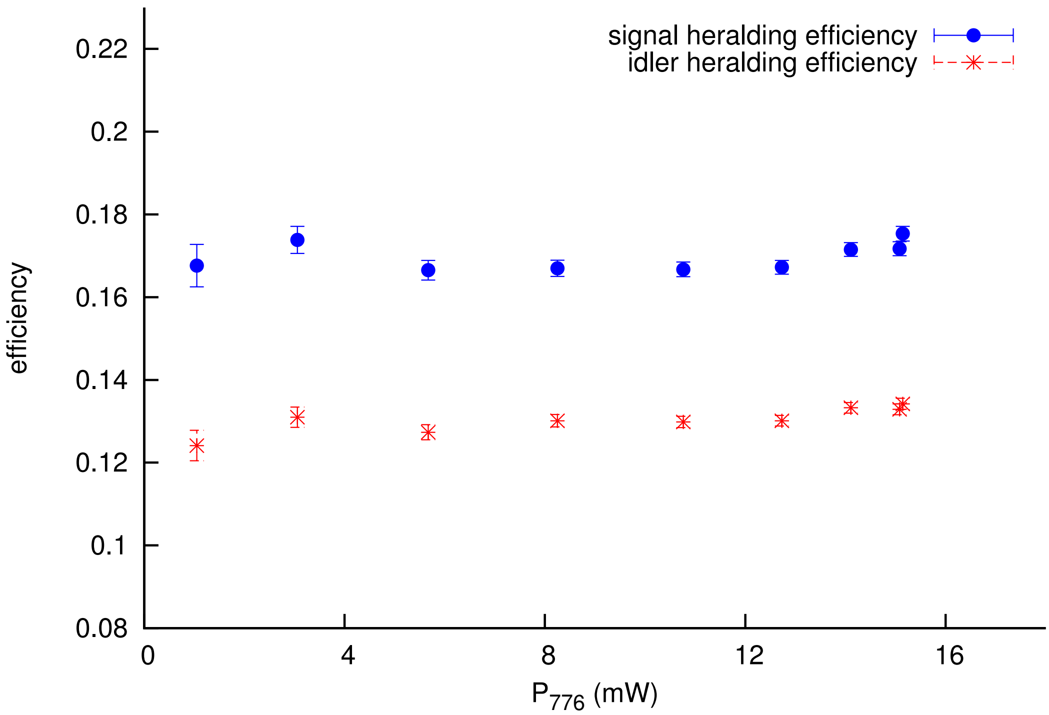

Figure 3.8: Efficiency of the photon pair source as a function of pump power at 776 nm for pump power at 780 nm = 420 μW and $\delta \approx 12$ MHz to the blue

decay and incoherent two step decay, as the photons from incoherent two step process also contributes to light collected in the phase-matched directions. Using 3.5 and 3.6, we can express the efficiency in the signal and idler modes as

$$\eta_{\mathrm{S\,(I)}} = \frac{r_p}{r_{\mathrm{I\,(S)}}} = \frac{I_{coh}}{I_{coh} + I_{incoh}} \tag{3.8}$$

Both I_{coh} and I_{incoh} increase as we approach near two photon resonance (towards $\delta = 0$) but I_{incoh} increases much faster. This results in a drop in efficiency near resonance (Equation 3.8).

We determine the signal and idler heralding efficiency of the source as a function of P_{776}. We observe that efficiency remains almost constant as we vary P_{776} [1] as shown in Figure 3.8

[1] P_{780} and δ is set such that efficiency remains constant with increase in P_{776}

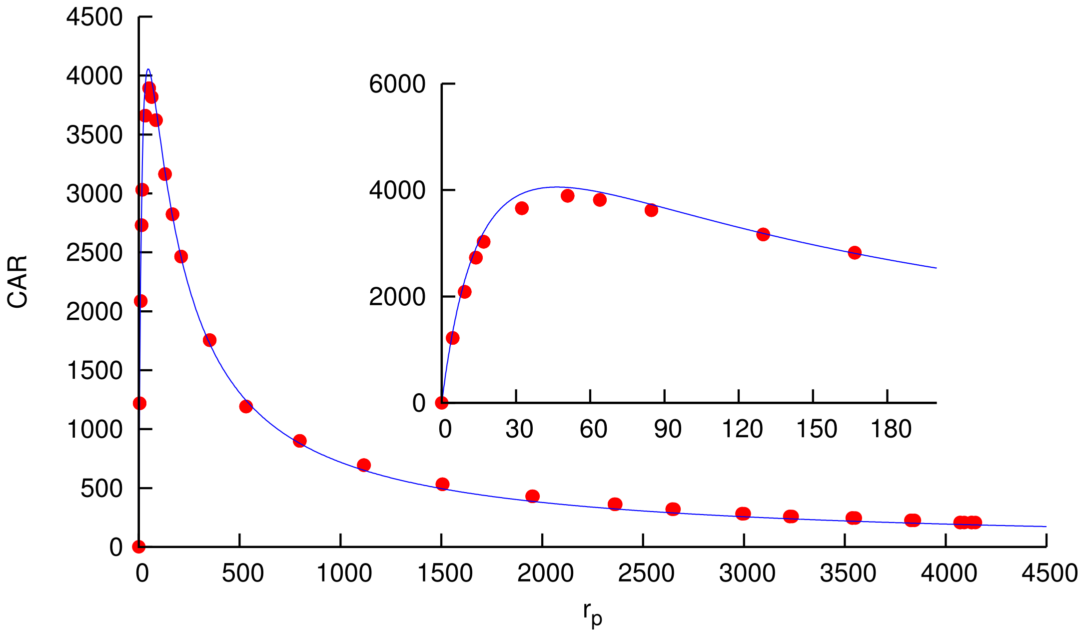

Figure 3.9: The coincidence to accidental ratio (CAR) as a function of pair rates r_p. The blue line is the theoretical model (Equation 3.10) with the parameters described in the text. The inset shows a zoom of the same plot. The vertical error bar on each point is smaller than the size of the data points.

3.6.3 Coincidence to accidental ratio (CAR)

A measure of the signal-to-noise (S/N) ratio of the photon pair source is the coincidence to accidental ratio (CAR). It is defined as [81, 82, 83] r_p

$$\mathrm{CAR} = \frac{R_p}{r_a} = \frac{r_\mathrm{I}\, r_\mathrm{S}\, \Delta t + r_p}{r_\mathrm{I}\, r_\mathrm{S}\, \Delta t}\,, \tag{3.9}$$

where accidental rate (r_a) is a measure of the rate of noise photon generation that can degrade the correlation characteristics of the photon pair source.

3.6.3.1 Results

The measured coincidence to accidental ratio (CAR) as a function of r_p is shown in Fig 3.9. We vary the r_p by varying P_{776}. We observe an increase in CAR, when P_{776} is reduced, This is because both r_p and r_a decreases with P_{776} but drop in r_a is much faster [1]. We observe a CAR peak at 3800 with a r_p of $50\,\mathrm{s}^{-1}$. With a further decrease

[1] accidental rate varies quadratically with pump power

in r_p, CAR starts to decrease as the noise (r_a) becomes more dominant. When the pump beams are blocked, the r_p vanish completely. At this point we are limited only by the background noise and detector's dark counts that contribute to the singles to the detectors in signal and idler mode. (d_S=200 s^{-1}, d_I=520 s^{-1}).

As illustrated in Figure 3.8, the signal and idler heralding efficiency of the source remains almost constant as a function of 776 nm pump power. Therefore, to fit the experimental data, we modify Equation 3.9, replacing the singles rate with heralding efficiencies to.[1]

$$\mathrm{CAR} = \frac{(\frac{r_p}{\eta_S} + d_S)\,(\frac{r_p}{\eta_I} + d_I)\,\Delta t + r_p}{(\frac{r_p}{\eta_S} + d_S)\,(\frac{r_p}{\eta_I} + d_I)\,\Delta t}\,. \tag{3.10}$$

The solid line in Figure 3.9 is obtained from Equation 3.10 with parameters η_S=17%, η_I=13%, d_S=200 s^{-1}, d_I=520 s^{-1}, $\Delta t = 30$ ns for this measurement.

3.7 Bandwidth measurements

One of the feature of this source is the generated photons are narrowband. An indirect assessment of the bandwidth of the idler photons can be obtained from the measured $g^{(2)}(\Delta t_{SI})$, since it is related to the Fourier transform of the spectral distribution. Assuming a transform-limited spectrum, we would infer a bandwidth of $\Delta\nu = 1/(2\pi\tau_0) = 24.4 \pm 0.1$ MHz (FWHM) for the heralded idler photons as inferred from the Figure 3.2. We also performed a direct measurement of the optical bandwidth of idler photons using a scanning Fabry-Perot cavity.

3.7.1 Design and specifications of the cavity

We use a Fabry-Perot cavity with two mirrors of reflectivity 99.94%, with radii of curvature of 50 mm. The finesse of the cavity $\mathcal{F}$ is inferred from the reflectivity of the mirrors as

$$\mathcal{F} = \frac{\pi\sqrt{R}}{1-R} = 6200\,. \tag{3.11}$$

The mirrors are placed inside an invar spacer because of its low coefficient of thermal expansion (1.2×10^{-6} K^{-1}). The distance (L) between the mirrors is 1.1 cm corresponding to a free spectral range ($FSR = c/2\,L$) of 12.8 GHz and linewidth of ($FSR/\mathcal{F}$) =

[1] Signal and idler singles rate (r_S, r_I) vary by changing 776 nm pump power

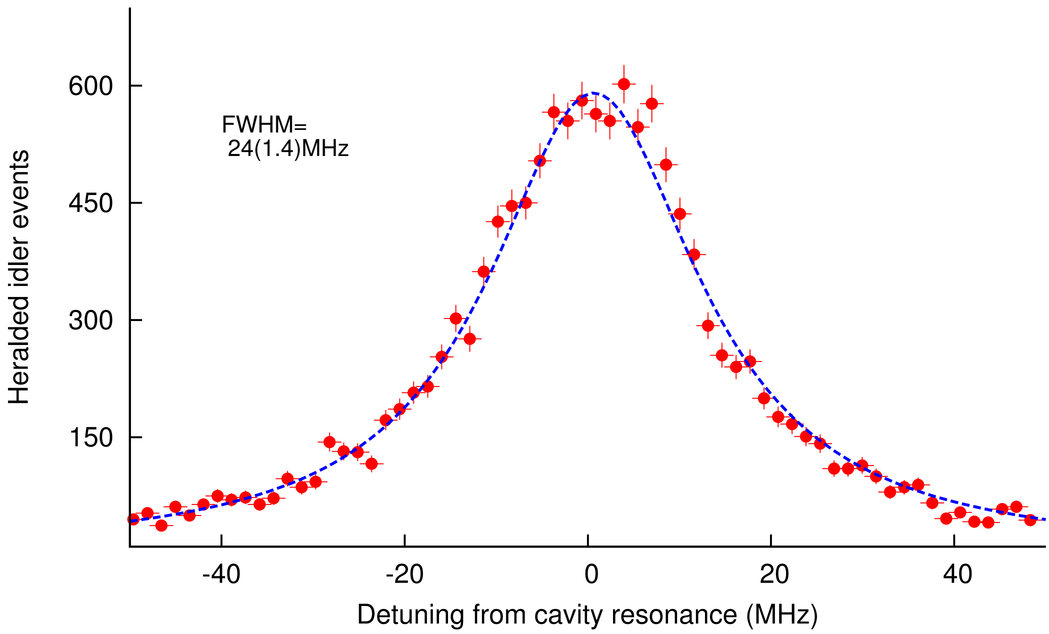

Figure 3.10: Spectral profile of idler photons, heralded by the detection of signal photons with an atomic cloud of OD$\approx$ 32. The frequency uncertainty is due to the uncertainty in voltage driving the cavity piezo. The line shows a fit to a model of a Lorentzian convolved with the cavity transmission spectrum. The fit gives a bandwidth of 24.7$\pm$1.4 MHz (FWHM).

2.8 MHz. The linewidth of the cavity is also experimentally verified by a cavity ring down measurement [84]. To minimise the frequency drift, the cavity is temperature stabilised to within 10 mK and kept in a vacuum (6×10^{-6} mbar). By scanning the voltage across a piezoelectric element attached to one of the mirror, we can change the distance between the mirrors and passively lock the cavity to a reference 795 nm laser such that the central transmission frequency of one of its longitudinal modes matches the resonance frequency of the $5S_{1/2}$, $F = 2 \rightarrow 5P_{1/2}$, $F = 2$ transition. The central transmission frequency is periodically recalibrated via the reference laser.

3.7.2 Bandwidth of heralded idler photons

We perform coincidence measurements between the detection of signal and idler photons for different detunings across cavity resonance (with an atomic cloud of OD$\approx$ 32). The data for each point is measured for $T = 60$ s. The results of this measurement are shown

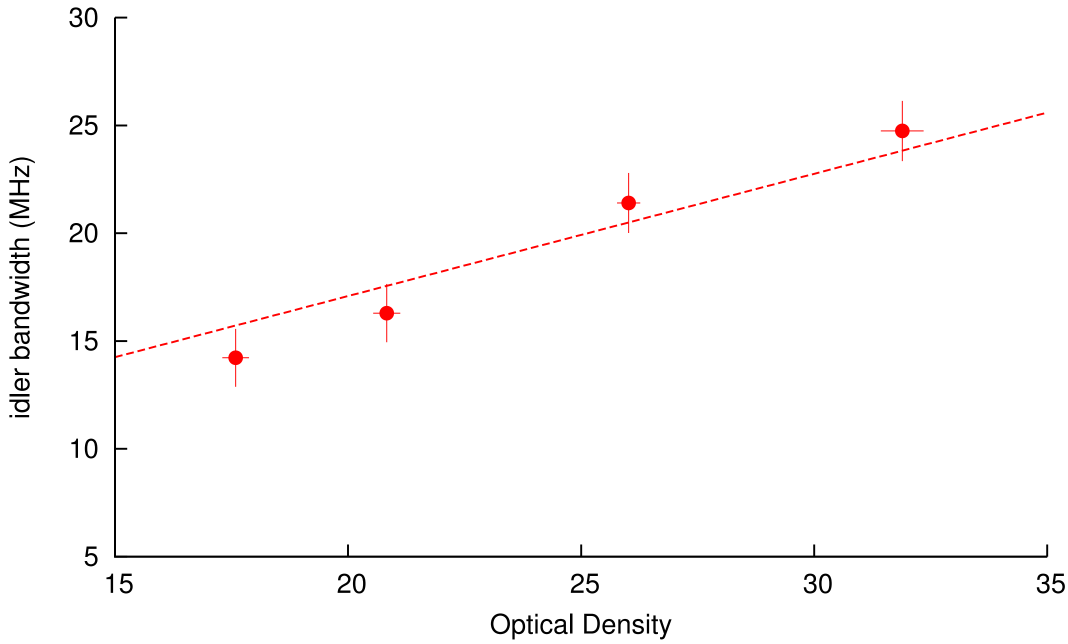

Figure 3.11: Bandwidth (FWHM) of heralded idler photons (pairs) at different cloud optical densities (OD) (filled circles). The line shows the theoretical model according to [1, 2]

in Figure 3.10.

For photons, that are generated by a parametric process in atoms, we expect a spectrum with a Lorentzian line shape [85]. However, since the cavity has finite linewidth, the line shape of the obtained spectrum is a convolution of Lorentzian with the Airy function of the cavity. The convolved function T(ν) used to fit the spectrum is [86]

$$T(\nu) = \frac{1}{FSR}\left[\frac{(1+\mathcal{F}')^{1/2}}{1+\mathcal{F}'\,\sin^2(\frac{\pi\nu}{FSR})}\right]. \tag{3.12}$$

We define a new parameter effective finesse ($\mathcal{F}'$) which is related to the FWHM of the convolved line shape as

$$\mathcal{F}' = \left(\frac{2\sqrt{R'}}{(1-R')}\right)^{\frac{1}{2}}, \tag{3.13}$$

where $R' = R\exp\left(\frac{-4\pi\gamma}{FSR}\right)$ and γ is the FWHM of the convolved spectrum. A fit of the spectrum using Equation 3.12 leads to a bandwidth of 24.7±1.4 MHz (FWHM) for the idler photons, if they are heralded by a signal photon (Figure 3.10). This is compatible

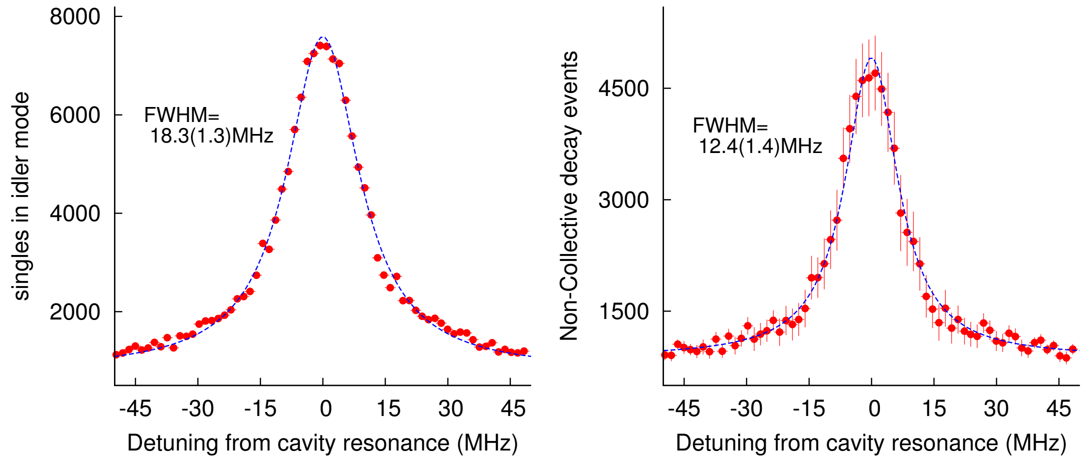

Figure 3.12: (Left): Spectral profile of singles in idler mode (unheralded idler events). The resulting bandwidth from the fit is 18.3±1.3 MHz (FWHM). (Right) Inferred idler spectrum from a two step (non-superradiant) decay with 12.4±1.4 MHz (FWHM) bandwidth from a fit.

with the bandwidth inferred from the correlation function $g^{(2)}(\Delta t_{\mathrm{SI}})$ for the same OD, which indicates that the spectrum of photons is indeed transform limited . We further vary the bandwidth of the heralded idler photons as a function of optical density (OD) as shown in Figure 3.11. The variation of the idler bandwidth due to collective enhanced decay (superradiant decay) can be modeled with the relation $\gamma = \gamma_0 (1 + \mu N)$ where $\gamma_0 = 2\pi \times 5.746$ MHz is the natural linewidth of the $5\mathrm{P}_{1/2}$, $F = 2 \rightarrow 5\mathrm{S}_{1/2}$, $F = 2$ transition. The model is similar to the one referred in Section 3.5.1 with $\gamma_0 = \frac{1}{\tau_{sp}}$. We also find a linear increase of OD compatible with this model.

3.7.3 Bandwidth of unheralded idler photons

The observed spectrum of all light in the idler mode (i.e., the unheralded ensemble) shows a narrower bandwidth of 18.3±1.3 MHz (FWHM) as shown in Figure 3.12 (Left). As discussed in Section 3.5.1 the singles in the idler mode is a statistical mixture of light emerging from coherent superradiant decay and an incoherent spontaneous two step decay. The optical bandwidth of light from the collective decay contribution should increase with the atom number N due to an enhanced cascade decay rate, while the bandwidth of light from the two step contribution should remain the same. Assuming that the incoherent contribution does not significantly contribute to the detected pairs due to small numerical apertures used for collection, we can infer its spectrum by subtracting the heralded idler spectrum from the singles spectrum after correction of losses from the filters.

$$r_{nc} = r_{\mathrm{S}} - \frac{r_p}{\eta_{\mathrm{S}}} \tag{3.14}$$

where r_{nc} is non-collective two photon decay event rate, r_{S} is the singles rate in the signal mode, r_p is the useful pair rate and η_{S} are the losses in signal arm. The losses (η_{S}) include filtering (11%), optical elements (7%), Detector (60%), polarization selection (12%), and fiber coupling loss (30%). The resulting spectrum for OD $\approx$ 32 is shown in Figure 3.12 (Right), with a width of 12.4$\pm$1.4 MHz FWHM. This exceeds the natural linewidth expected for the incoherent two step decay, probably due to frequency dependent self-absorption effects in the atomic cloud.

3.8 Thermal statistics of unheralded photons

While it is well-known that light in each of the modes in a parametric fluorescence should exhibit thermal photon statistics [71], the coherence time of most photon pair sources is too short to be directly observable in an experiment (picoseconds or femtoseconds in non-linear crystals). Due to the long coherence time τ_0 of the source presented here, we are able to measure the photon statistics with a Hanbury-Brown–Twiss experiment as shown in Figure 3.13 (Left). The signal (idler) light is distributed with a 50:50 beam splitter onto two silicon avalanche detectors (D_1 and D_2). The results are shown in Figure 3.13 (Right). We observe a normalized $g^{(2)}_{\mathrm{SS}}(\Delta t_{12} = 0) = 2.06 \pm 0.06$ which is compatible with $g^{(2)}(0) = 2$ of an ideal single mode thermal state within the statistical uncertainty [87].

From a similar experiment performed on the idler photons, we observe that the peak of $g^{(2)}_{\mathrm{II}}(0)$ approaches 2.03$\pm$0.08 as expected. A temperature tuned etalon (linewidth 375 MHz FWHM, peak transmission 86%) is placed in the idler mode to remove uncorrelated photons from the $5\mathrm{P}_{1/2}$, $F = 2 \rightarrow 5\mathrm{S}_{1/2}$, $F = 1$ transition. Without the solid etalon, the idler photons coupled into the single mode fiber are of two different frequencies, thus $g^{(2)}_{\mathrm{II}}(0) < 2$ is expected and indeed observed (1.69 ± 0.02).

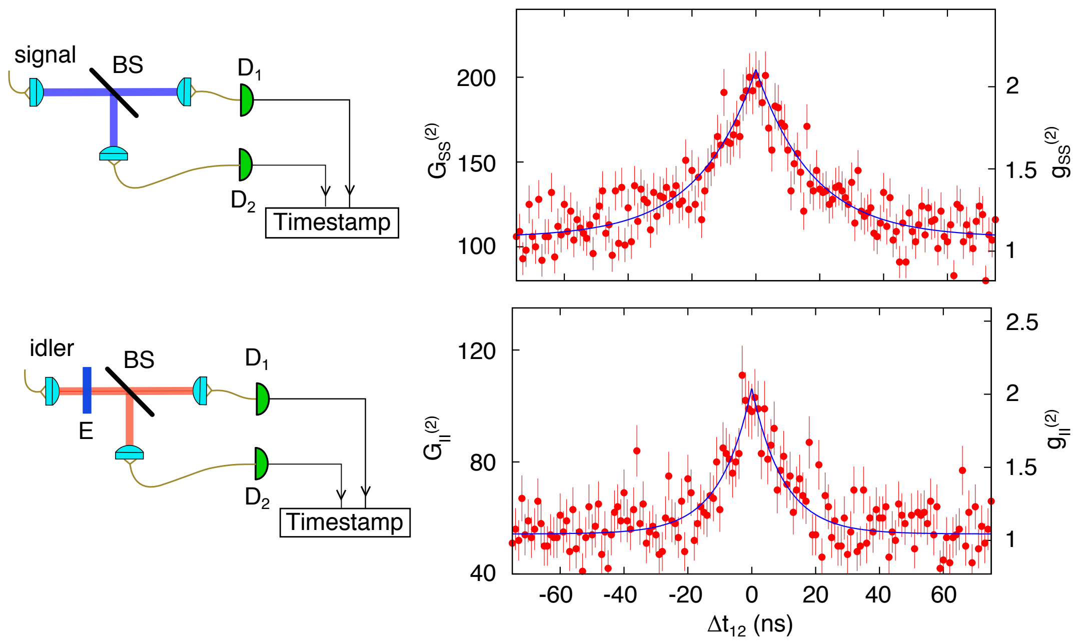

Figure 3.13: (Left) Hanbury-Brown-Twiss setup to measure the photon statistics in the signal and idler modes. The etalon E in the idler mode is used to filter uncorrelated photons from $5P_{1/2}$, $F = 2 \rightarrow 5S_{1/2}$, $F = 1$ transition. (Right) Time resolved coincidence histogram $G^{(2)}_{\mathrm{SS}}(\Delta t_{12})$ and its normalized version in a Hanbury-Brown–Twiss experiment on signal photons (detectors D_1, D_2) for $T = 76.3$ s. The solid line shows a fit to the model $g^{(2)}_{\mathrm{SS}}(\Delta t_{12}) = C \times (1 + D \times \Delta t_{12} \exp(-|\Delta t_{12}|/\tau_0))$, resulting in $C = 1.08 \pm 0.1$, $D = 0.93 \pm 0.06$ and $\tau_0 = 17.8 \pm 1.4$ ns. A similar measurement performed on idler photons for $T = 247.3$ s, lead to fit parameters $C = 1.04 \pm 0.08$, $D = 0.96 \pm 0.08$, and $\tau_0 = 9.9 \pm 1.2$ ns.

3.9 Cauchy-Schwarz inequality

The Cauchy-Schwarz inequality bounds the intensity correlation $g^{(2)}$ between two independent classical fields [85, 88]

$$R = \frac{[g^{(2)}_{\mathrm{SI}}(\Delta t_{\mathrm{SI}})]^2}{g^{(2)}_{\mathrm{II}}(0) \cdot g^{(2)}_{\mathrm{SS}}(0)} \leq 1 \tag{3.15}$$

This inequality between the signal and idler fields in our experiment is violated by a factor $R = 53 \times 10^6$ at $\Delta t_{\mathrm{SI}} = 0$ which shows that our source exhibits statistics unexplainable by classical electromagnetic field theory. Our violation factor strongly exceeds the values reported from similar experiments by Du *et al.* ($R = 11600$, [39]) and Willis *et al.* ($R = 495$, [55]). We attribute this to lower background counts as compared to what has been observed with hot vapours.

3.10 Conclusion

Our photon pair source exhibits a high heralding efficiency, is spectrally bright, and shows a narrow optical bandwidth for signal and idler photons. We also demonstrate the thermal statistics of the signal and idler photons from a direct autocorrelation measurement. The violation of the Cauchy-Schwarz inequality by a factor of 53×10^6 indicates a strong non-classical correlation between the generated photons. The narrow bandwidth and the wavelength match with the transitions in ^{87}Rb, makes our source a prime candidate for heralded interaction with single atom systems, and quantum memories based on atomic ensembles. Beyond correlated photon pair preparation, this scheme can also provide polarization entangled photons by an appropriate choice of pump polarization [38, 55] which is discussed in Chapter 4

Chapter 4

Polarization entangled photon pairs and Quantum beats

The chapter is divided into two parts. We will first present an estimation of the polarization entangled state of the generated photon pairs by performing quantum state tomography. In the second half, we will present an observation of controlled, high-contrast quantum beats in the time correlation measurement between the generated photon pairs. For both measurements, we pump in the reverse direction of the cascade such that photon pairs of wavelength 776 nm and 780 nm are generated from the atomic cloud. The quantum beats are caused by interference between the two-photon decay paths through different intermediate hyperfine levels in the cascade decay.

4.1 Introduction to polarization entanglement

Entangled photon pairs have been vital for performing fundamental tests of quantum mechanics [89, 90]. They have also found numerous applications in quantum communications [30, 91], cryptography [22], teleportation [92] and precision measurements [93]. Entanglement between photons can be established in several degrees of freedom [94, 95, 96]. A common choice is the polarization degree of freedom. Photon pairs entangled in polarization have been extensively studied with a large number of photon pair sources. The first ones were probably based on spontaneous cascade decays from an atomic beam [48] followed by spontaneous parametric down conversion in nonlinear optical crystals [97], trapped ions [98], hot vapors [36], and recently also cascade emission from quantum dots [99]. Particularly relevant to our discussion is the work of reference [38], where the authors have used a cold atomic cloud to generate polarization entangled photon pairs.

4.2 Experimental setup

The experimental setup is similar to the one described in Chapter 3. However, for this experiment, we reverse the direction of the cascade such that atoms are excited from $5S_{1/2}, F = 2$ to $5D_{3/2}$, $F = 3$ level via a $5P_{1/2}$, $F = 2$ level. From the $5D_{3/2}$, $F = 3$ excited level, atoms decay back to the $5S_{1/2}, F = 2$ ground level through two paths, labelled as X or Y, via two intermediate hyperfine levels, resulting in the emission of photon pairs of wavelength 776 nm (signal) and 780 nm (idler). The motivation behind choosing this level scheme is to use this heralded 780 nm photon and perform a HOM interference experiment with a single 780 nm photon emitted from spontaneous decay of a single ^{87}Rb atom. The details about the experiment are discussed in Chapter 5.

The schematics and cascade level scheme is shown in Figure 4.1. We overlap the two pump beams of wavelength 795 nm and 762 nm in a co-linear, co-propagating geometry inside a cloud of optical density ≈ 32. The 795 nm pump beam is red detuned by 30 MHz from the intermediate level $5P_{1/2}$, $F = 2$. Energy conservation and phase matching results in the generation of signal and idler photon pairs from both decay paths with a frequency difference of δf=266 MHz corresponding to the hyperfine splitting of the intermediate level. A quarter-wave (q), half-wave plate (h) and a Polarizing Beam Splitter (PBS) are placed in both signal and idler modes for measuring the polarization correlations (Figure 4.1). The generated photons are collected into single-mode fibers and detected by the avalanche photodetectors[1]. The timing sequence for the experiment comprises of 10 μs period for the photon pair generation, interleaved with periods of 150 μs when the MOT is turned on to replenish and cool the atomic cloud.

4.3 Tomography of the polarization state

We first investigate the polarization state of the generated photon pairs for each decay path. To do that, we separate light emerging from the two decay paths using a temperature tuned solid fused silica etalon (2 cm length, transmission bandwidth 53 MHz

[1]For the measurement shown in Figure 4.5, we have used MPD detectors with jitter time 40 ps

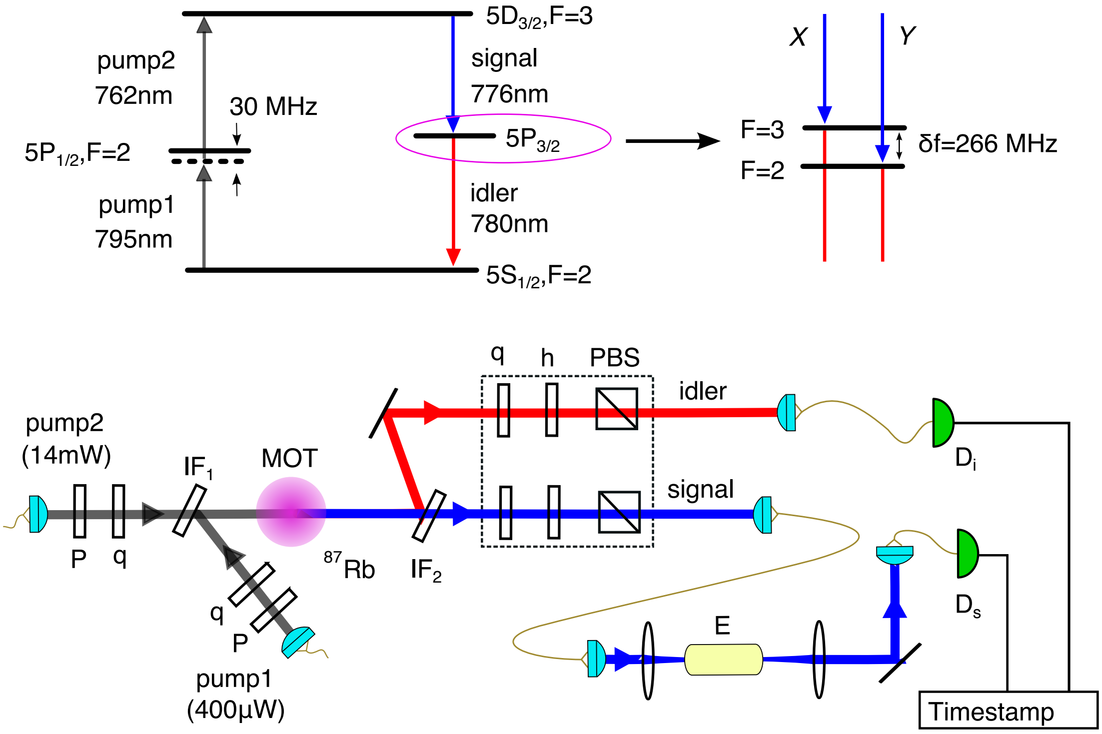

Figure 4.1: Schematic of the experimental setup: The interference filters (IF_1) combines the two pump beams in co-propagating geometry inside the cloud and IF_2 separates the signal and idler photons from residual pump light. The pump beams can be adjusted to any value from a linear to circular polarization using Polarizers (P), quarter wave plates (q). A pair of quarter wave plates (q), half wave plates (h) and polarizing Beam Splitter (PBS) are used in collection modes for measuring polarization correlations. A solid etalon (E) is used as a filter to separate the two decay paths X and Y, Di–Ds: Avalanche Photodetectors. The inset shows the cascade level scheme in ^{87}Rb.

(FWHM)) as a frequency filter in the signal mode. The etalon is temperature stabilised to within 1 mK in order to minimize any frequency drifts. The temperature of the etalon is tuned such that the central transmission frequency of one of its longitudinal modes is matched to the resonance frequency of either $5P_{3/2}$, $F = 3 \rightarrow 5D_{3/2}$, $F = 3$ or $5P_{3/2}$, $F = 2 \rightarrow 5D_{3/2}$, $F = 3$ transition.

In the cascade decays corresponding to the two decay paths X and Y, polarization entanglement arises from indistinguishable decay paths, in our case provided by sufficiently degenerate Zeeman sublevels of each hyperfine level. Choosing the quantization axis along the beam propagation direction of pump and target modes, we only drive transitions with $\Delta m_F = \pm 1$ with orthogonal circularly polarized pump beams ($|L\rangle$ for pump1 and $|R\rangle$ for pump2). In any parametric process like FWM, the quantum state of the medium remains unchanged before and after the interaction. Therefore, and due to the rotational symmetry of the atomic cloud in beam propagation direction, the angular momentum of pump and target modes must be conserved. This condition, along with the angular momentum selection rules limits the possible polarizations of the generated signal-idler photon pairs to $|LR\rangle$ (or $|RL\rangle$). Since the process is coherent and the two possible states are indistinguishable in spatial modes and arrival times, we obtain an entangled state in polarization. A simple model to estimate the polarization entangled state of photon pairs from our source is discussed in Section 4.3.1

In order to completely characterize the polarization state of photon pairs from the cold cloud of atoms, we perform a quantum state tomography, independently for the two decay paths X and Y. The quarter-wave plates, half wave plate in the signal and idler modes for projection base selection (see Figure 4.1) are mounted on rotation mounts controlled by a stepper motor, the projection is carried out using polarizing beam splitters (PBS). Coincidence measurements in 16 independent basis combinations are carried out as shown in Table 4.1, and the density matrices ρ_X and ρ_Y of the biphoton polarization states are tomographically reconstructed [100, 101].

The density matrices of both the decay paths is shown in Appendix C. The real components of the resulting states $\rho_{X,Y}$ are shown in the Figure 4.2. The imaginary part for both cases remains within $\pm 0.09i$.

From the reconstructed matrices, we can infer a purity of the biphoton state with $P_X = \mathrm{tr}[\rho_X^2] = 0.921 \pm 0.018$, which suggests that the polarization state is very close to a pure state.

Measurement polarization		**Coincidences in 3 min**		**Normalization counts in 3 min**	
Signal	**Idler**	X	Y	X	Y
L	L	40	21	104761	301037
L	R	2890	2196	106442	303703
R	R	39	22	105960	314461
R	L	5948	1349	104748	310206
-	L	3255	910	102066	298136
-	R	882	876	103403	299937
H	R	1455	1196	114502	302626
H	L	2734	714	114511	306598
H	-	2539	799	112718	301586
H	H	352	311	111691	308062
-	H	1842	708	110398	309087
L	H	1332	945	107775	310633
R	H	3078	519	106758	310747
R	+	2369	550	111733	302095
L	+	1847	1440	111710	298813
-	+	3891	1837	107917	298834

Table 4.1: Number of coincidences in 3 minutes for different polarization measurement on signal and idler modes for the decay paths X and Y. The normalization counts are obtained by collecting the 776 nm fluroscence from the atom cloud without any polarization projection. This corrects for any fluctuations in photon pair rate due to the fluctuations in the pump beam powers. Horizontal polarization is labeled as $|H\rangle$, vertical is $|V\rangle$, $|L\rangle = \frac{|H\rangle + i|V\rangle}{\sqrt{2}}$, $|R\rangle = \frac{|H\rangle - i|V\rangle}{\sqrt{2}}$ are left-handed and right-handed circular polarization, $|+\rangle = \frac{|H\rangle + |V\rangle}{\sqrt{2}}$, $|-\rangle = \frac{|H\rangle - |V\rangle}{\sqrt{2}}$.

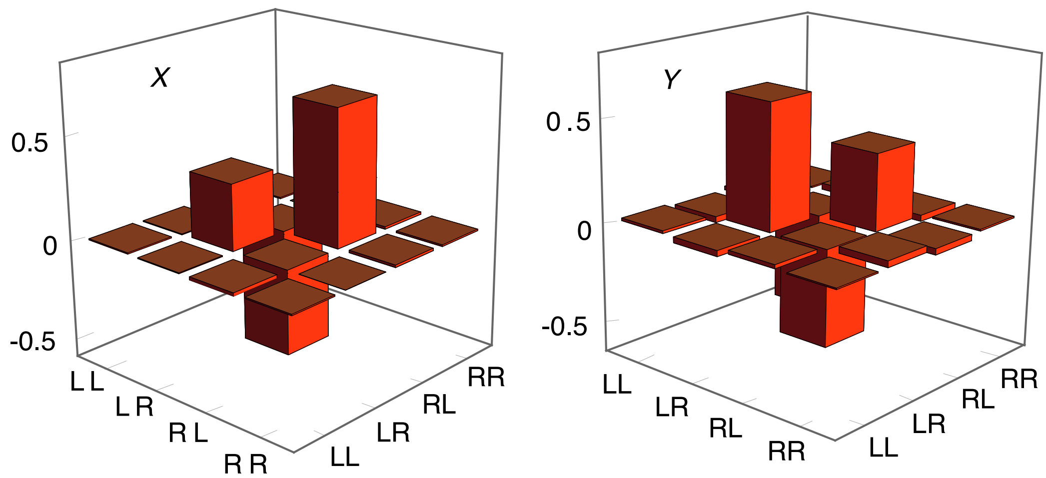

Figure 4.2: Tomographic reconstruction of the density matrix (real part only) for the biphotons generated via decay X (left) and Y (right). The pumps are set to orthogonal circular polarizations ($|L\rangle$ and $|R\rangle$, respectively). The decay path is selected by a temperature tuned etalon.

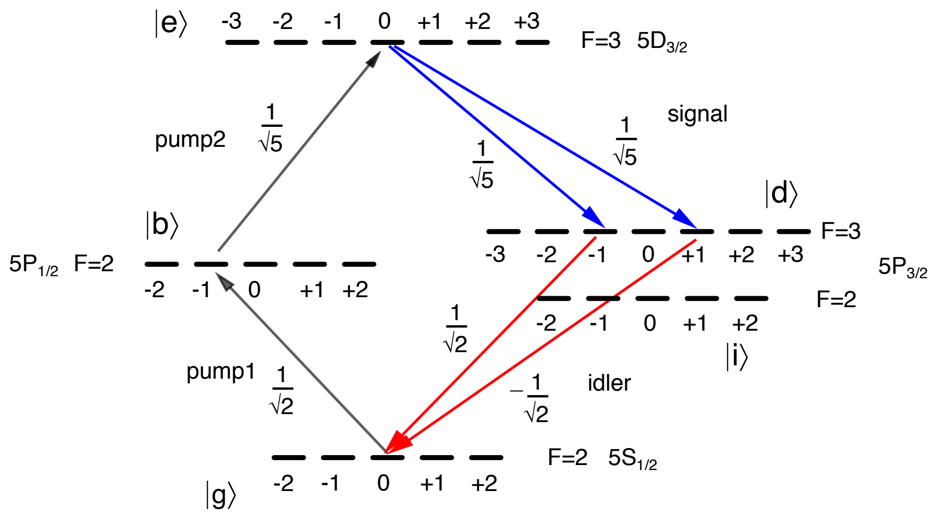

Figure 4.3: Cascade level scheme with relevant hyperfine levels and Zeeman manifold: We choose the quantisation axis along the beam propagation direction of pump and target modes and drive only transition with $\Delta m_F = \pm 1$ using orthogonal circularly polarized pump beams. The atoms are initially prepared in incoherent mixture of all the Zeeman states of the ground level $|g\rangle$. We show Clebsh-Gordon coefficients for only one of the cycle around the cascade starting with $m_F = 0$

We can also calculate the concurrence [102] $C_X = 0.891 \pm 0.015$, and entanglement of formation [103] $E_X = 0.85 \pm 0.04$[1], two commonly cited measures of entanglement. For decay path Y, we find corresponding values of $P_Y = \mathrm{tr}[\rho^2] = 0.964 \pm 0.03$, $C_Y = 0.939 \pm 0.014$ and $E_Y = 0.98 \pm 0.01$, exhibiting an even higher purity. Uncertainties in the quantities quoted are all computed by propagating Poissonian noise from the initial coincidence measurements.

The remarkable observation is that the obtained polarization states are relatively pure, even though the atomic ensemble is prepared in a not very well defined statistical mixture of magnetic sublevels by the magneto-optical cooling/trapping process.

4.3.1 Estimation of polarization entangled state

We consider the polarization state of photon pairs emerging from the cloud to be of the form

$$a_0 |LL\rangle + a_1 |LR\rangle + a_2 |RL\rangle + a_3 |RR\rangle \ . \tag{4.1}$$

To calculate the probability amplitudes $a_{(0-3)}$, we consider a simple model based only on the Clebsh-Gordan coefficients of all four transitions of the cascade (Figure 4.3) following the theoretical work by [104]. We assume that the experiment starts with all atoms prepared in incoherent mixture of all the Zeeman states of the ground level $|g\rangle$ such that probability of an atom prepared in one of the Zeeman state $|g, m_F\rangle$ is $p_m = \frac{1}{2F_g+1}$. The second assumption is that the atom returns to its original Zeeman state after the cycle owing to phase matching condition.

Based on the two assumptions, the probability amplitudes $a_{(0-3)}$ can be written as

$$a_{(0-3)} = \frac{X_{\alpha_S,\, \alpha_I}}{\sqrt{\sum\limits_{\alpha_S, \alpha_I = \pm 1} (X_{\alpha_S, \alpha_I})^2}} \, , \tag{4.2}$$

where α_S and α_I are the helicities of the signal and idler photons, and X_{α_S,α_I} is the product of relevant Clebsch-Gordan coefficients [1] that couple the individual $|m_F\rangle$ states of the different hyperfine levels involved in the four wave mixing process,

$$X_{\alpha_S,\alpha_I} = \sum_{m_F=-F_g}^{F_g} p_m \, C^{F_g \; 1 \; F_b}_{m_F \; -1 \; m_F-1} \, C^{F_b \; 1 \; F_e}_{m_F-1 \; 1 \; m_F} \, C^{F_d \; 1 \; F_e}_{m_F-\alpha_S \; \alpha_S \; m_F} \, C^{F_g \; 1 \; F_d}_{m_F \; -\alpha_I \; m_F-\alpha_I} \, . \tag{4.3}$$

The predicted state from the this model $|\psi_X\rangle \approx 0.55 \, |LR\rangle - 0.83 \, |RL\rangle$ agrees with the measured state with a fidelity of 94±1% . For the other decay path, the model predicts a state $|\psi_Y\rangle \approx 0.92 \, |LR\rangle - 0.39 \, |RL\rangle$, which agrees with the measured state with a fidelity of 93±1%.

4.4 Introduction to Quantum beats

Quantum beats are oscillations in the radiation intensity of an ensemble of excited atoms due to interference of emission paths. They are one of the earliest predictions

[1] The value should be 0 for a completely separable state to 1 for a maximally entangled state

[1] The notations used for Clebsch-Gordan coefficients in Equation 4.3 are the standard notations described in [64, 104].

of quantum mechanics [105]. First experimental observations of quantum beats were induced by pulsed optical excitation of atoms with two upper states which decay to the same ground state [106, 107]. Recently, quantum interference in absorption and emission of single photons from spontaneous decay of a single ion was observed [108]. Particularly similar to our experiment is the work of reference [109, 110], where authors observed quantum beats in the temporal correlation between the two photons emitted in a cascade level scheme in continuously excited atomic ensembles. The beats originate from a quantum interference between the various decaying channels.

4.5 Time correlation measurement

4.5.1 With etalon

We perform a time correlation measurement between the detection of signal and idler photons for the individual decay paths using an etalon in the signal mode. The histogram of coincidence events as a function of time delay Δt_{SI} between the detection of signal and idler photons is shown in Figure 4.4.

For an atomic cloud of OD ≈ 32, we obtain coherence time of $\tau_X = 5.6 \pm 0.1$ ns for an idler photon heralded by a signal photon, and $\tau_Y = 13.1 \pm 0.2$ ns for decay path X and Y, respectively. The decay time constants in both cases are lower than the single atom spontaneous decay time of 27 ns from $5\mathrm{P}_{3/2}$ level. This is due to the superradiance effects in an optically thick atomic ensemble [2]. The details about superradiance is discussed Section 3.5.1

The difference in decay time constants for the two decay paths can be understood by considering the difference in transition strengths d^2 (d is the transition dipole matrix element). The transition from $5\mathrm{P}_{3/2}$, $F = 3$ to $5\mathrm{S}_{1/2}$, $F = 2$ is 2.8 times stronger than from $5\mathrm{P}_{3/2}$, $F = 2$ [3]. This results in higher optical density (OD) for the $F = 3$ transition as OD $\propto d^2$. (Equation 2.4). Therefore, we observe a faster collective enhanced decay from $5\mathrm{P}_{3/2}$, $F = 3$ level as compared to $F = 2$.

4.5.2 Without etalon

In the absence of an etalon in the signal mode (Figure 4.1), both decay processes through paths X and Y can contribute to observed photon pairs. While these possibilities are distinguishable by their energy, an observation of a coincidence detection event

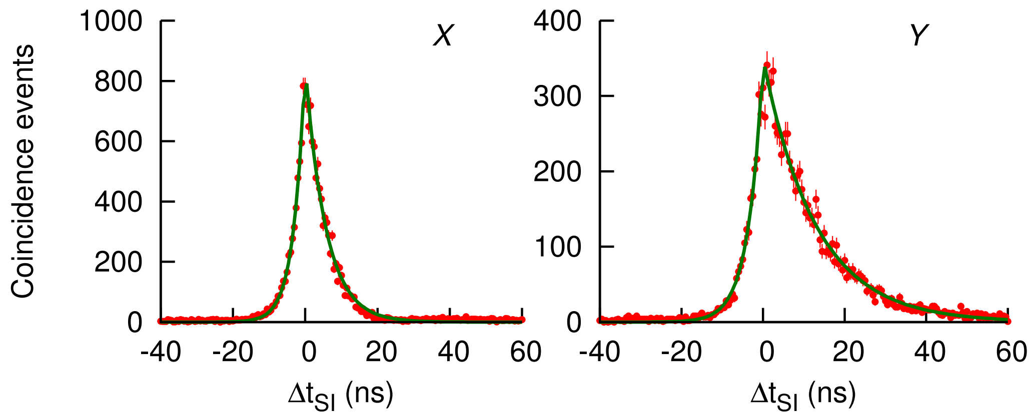

Figure 4.4: Coincidences as a function of the detection time difference between the arrival of signal and idler photons for the decay path X (left, collected over 7 minutes)) and Y (right, collected over 14 minutes). The decay path leading to the photons is selected by a temperature tuned etalon. The solid line in both the cases shows a fit to the model $G^{(2)}_{\mathrm{SI}}(\Delta t_{\mathrm{SI}}) = f(\Delta t_{\mathrm{SI}}) + g(\Delta t_{\mathrm{SI}})$, where $f(\Delta t_{\mathrm{SI}}) = A\,\exp(\Delta t_{\mathrm{SI}}/\tau_r)$ for $\Delta t_{\mathrm{SI}} < 0$ and $g(\Delta t_{\mathrm{SI}}) = B\,\exp(-\Delta t_{\mathrm{SI}}/\tau_{(X,Y)})$ for $\Delta t_{\mathrm{SI}} > 0$. The rise time of $\tau_r = 3.1 \pm 0.2\,\mathrm{ns}$ is a consequence of the finite bandwidth of the etalon $(1/(2\,\pi\,\tau_r) = 51.3\,\mathrm{MHz})$

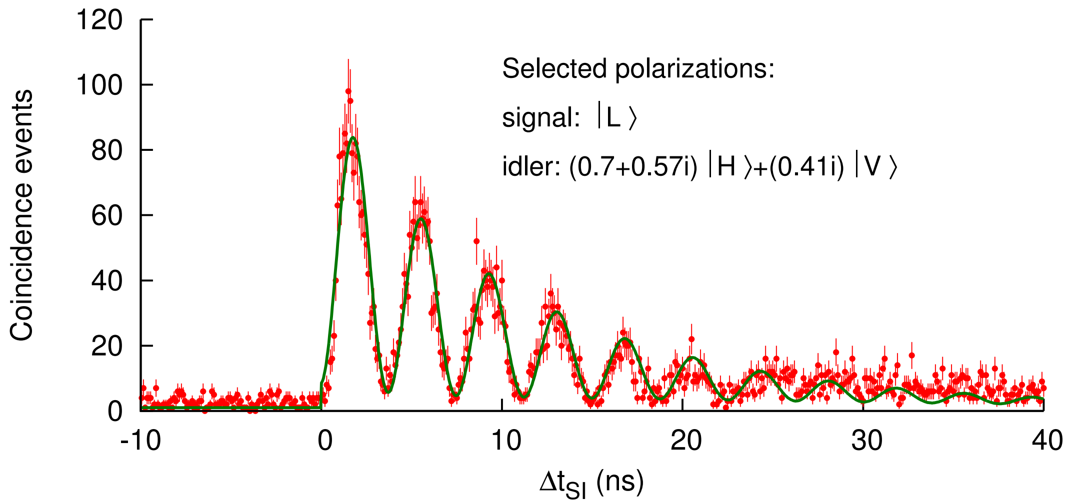

Figure 4.5: (a) Coincidences as a function time delay between the detection of signal and idler photons, with no etalon in the signal mode (collected over 5 hours). The quantum beats are associated with the hyperfine splitting of 266 MHz between $F = 3$, $F = 2$ of the $5P_{3/2}$ level. The solid line is a fit to the model 4.5.

in time between signal and idler photons can remove this distinguishability, and lead to the observation of quantum beats between decay paths. The detection of signal photon prepares the atoms in the coherent superposition of the $F = 3$ and $F = 2$ hyperfine levels. The atom then evolves with Bohr frequencies corresponding to energy splitting of the levels, which is reflected in the modulation ("beat") of the correlation function in time. The coincidence events as a function time delay Δt_{SI} is shown in Figure 4.5 and shows a clear oscillation. The frequency $\delta f = 266\,\mathrm{MHz}$ of the beat is equal to the hyperfine splitting between the levels involved in the interference process. The measurement is performed with the pumps set to orthogonal linear polarization ($|H\rangle$ and $|V\rangle$ for the pump1 and 2, respectively). The polarization of signal and idler modes is set to observe maximum contrast. The measurement is performed with silicon avalanche photodetectors from MPD (jitter time $\approx 10\,\mathrm{ps}$ with quantum efficiency $\approx 10\%$ at $780\,\mathrm{nm}$). We define the contrast as a usual visibility $V = (C_{max} - C_{min})/(C_{max} + C_{min})$, where $C_{min,max}$ are the maximal and minimal coincidence events within the beat period and can be obtained from coincidence plot. For this measurement, we extract a maximum contrast of 94.1% for the first fringe.

To model the interference between the different decay paths, we introduce probability amplitudes $c_{X,Y}$ of the photon pair generation process for the decay paths X and Y; they can be written as a function of detection time difference Δt_{SI} between signal and idler photons [2] as

$$\begin{aligned} c_X(\Delta t_{\mathrm{SI}}) &= \Theta(\Delta t_{\mathrm{SI}}) A_X e^{-\frac{\Delta t_{\mathrm{SI}}}{2\tau_X}} e^{-i\omega_i \Delta t_{\mathrm{SI}}}\,, \\ c_Y(\Delta t_{\mathrm{SI}}) &= \Theta(\Delta t_{\mathrm{SI}}) A_Y e^{-\frac{\Delta t_{\mathrm{SI}}}{2\tau_Y}} e^{(-i\omega_i+\delta f)\Delta t_{\mathrm{SI}}+\phi}\,, \end{aligned} \tag{4.4}$$

and interfere to a pair detection probability

$$\begin{aligned} G^{(2)}_{\mathrm{SI}}(\Delta t_{\mathrm{SI}}) &= |c_X + c_y|^2 \\ &= \Theta(\Delta t_{\mathrm{SI}}) A_X^2 e^{-\frac{\Delta t_{\mathrm{SI}}}{\tau_X}} + A_Y^2 e^{-\frac{\Delta t_{\mathrm{SI}}}{\tau_Y}} + \\ &\quad 2\,A_X\,A_Y\,e^{-\frac{\Delta t_{\mathrm{SI}}}{2(\tau_A+\tau_Y)}} \cos\left(2\pi\,\delta f \Delta t_{\mathrm{SI}} + \phi\right)\,. \end{aligned} \tag{4.5}$$

The coefficients A_X, A_Y and initial phase of oscillations ϕ depend on the product of all Clebsh-Gordon coefficients of the transitions involved for each four wave mixing contribution, and can be evaluated from Equation 4.3, for given pump and target mode polarizations. We use equation 4.5 for fitting experimental data shown in Figure 4.5. The resulting pair emission profile agrees very well with the data.

The dependence of the interference coefficients A_X and A_Y allows us now to control contrast and the initial phase of the oscillations with the choice of polarization of projective measurements on the generated photons [108]. The coincidence time distribution with three different polarization projections on the generated photons are shown in Figure 4.6. We observe the damping of the oscillations with the suppression of the coincidences from one decay path (Figure 4.6, Top). We estimate the coincidences in decay path Y to be suppressed by a factor of 32 from the ratio of the coefficients A_X and A_Y from the fit. We estimate the total pair detection rate upto $3000\,\mathrm{s}^{-1}$ for this polarization settings [16] since the contribution of the coincidences is mainly from the decay path X.

Figure 4.6 (Middle/Bottom) shows the coincidences for two different sets of measurement polarizations where we observe the beats. One can observe a relative phase shift of π in the initial phase of the oscillations. The situation of quantum beats in our case is quite similar to quantum interference effect observed in Young's double slit experiment. As in the latter case, any attempt to determine which channel the photon is scattered results in disappearance of beat pattern. The same analogy can be applied here. By using of appropriate polarization for the pumps and collections modes, one can erase 'which path information' that results in suppression of coincidences through one decay path and hence erase beats [111, 112].

4.6 Conclusion

In this Chapter, we have characterized the polarization entangled state of photon pairs from a cold cloud of atoms by performing a quantum state tomography, individually for two decay paths of the cascade. The resulting polarization entangled state for both decay paths is not maximally entangled but reasonably close to it. This is due to the dependence on Clebsch-Gordan coefficients that couple the individual $|m_F\rangle$ of the different hyperfine levels involved in the fourwave mixing process. We observe a high-contrast quantum beats in the time correlation measurement between the generated photon pairs. The contrast and the initial phase of beats can be controlled with the choice of polarization of pumps and projective measurements on the generated photons.

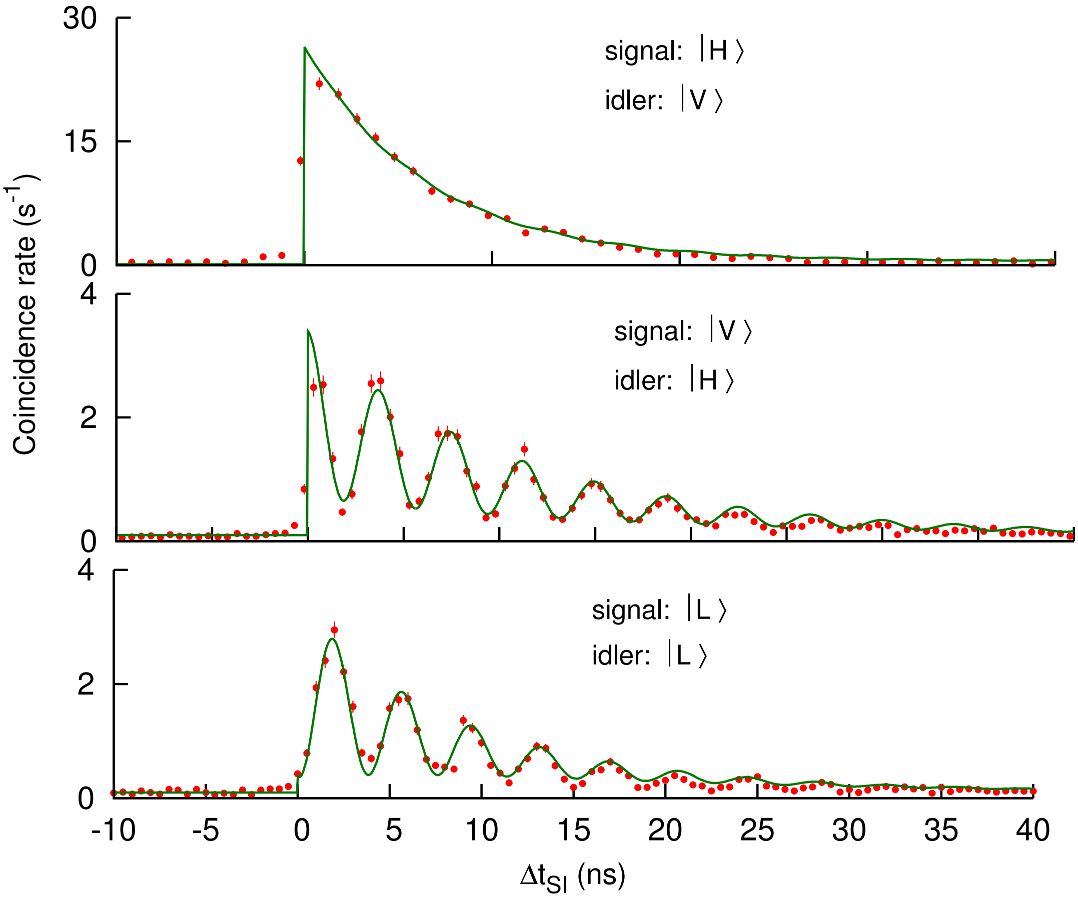

Figure 4.6: Coincidence rate as a function of time delay between the detection of signal and idler photons for different choice of polarization of signal and idler photons. (Top) The beats are damped by choosing the appropriate polarizations due to suppression of coincidences from decay path Y. (Middle/Bottom): Controlling the initial phase of oscillations with certain polarization projections. In these two cases, the oscillations have a relative phase difference of π

Chapter 5

Hong-Ou-Mandel interference between single photons from a single atom and cold atomic vapour

In this Chapter, we will present a Hong-Ou-Mandel (HOM) interference experiment between single photons produced by a single ^{87}Rb atom and a cold cloud of ^{87}Rb vapour. We will first present a theory to describe the HOM interference effect. This is followed an overview of the single atom setup, the fourwave mixing setup and the HOM interferometer. Finally, we will demonstrate the observation of HOM dip by varying the overlap between the temporal envelope of the single photons

5.1 Introduction

Many proposed all-optical quantum-photonic networks are based on indistinguishable single photons carrying information between nodes and interacting with one another [113, 114]. It is important to demonstrate that single photons generated from different systems using different physical processes can indeed be indistinguishable and exhibit two-photon interference effects such as Hong-Ou-Mandel (HOM) interference [41]. HOM interference takes place when two indistinguishable photons enter a 50:50 Beam Splitter (BS) leave together from the same output port of the BS. This effect has been extensively studied in the past using various photon sources, based on nonlinear

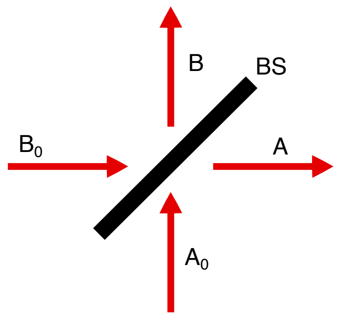

Figure 5.1: A 50:50 Beam Splitter (BS) with input modes A_0 and B_0, output modes as A and B

crystals [41, 115, 116], neutral atoms [117, 118], quantum dots [119, 120], NV centers in diamond [121], single molecules [122, 123], atomic ensembles [124] and trapped ions [125]. In most of these experiments the two photons originate either from the same source or separate sources with a same physical generation process. Two photon interference has also been demonstrated between two disparate sources: a quantum dot and a non-linear crystal based on Parametric Down-Conversion (PDC) [44]. Another experiment involves interference between the single photons from PPLN waveguide and microstructured fiber [43]. Both the experiments rely on spectral filtering in order to match the bandwidth of the generated photons.

We present a two-photon interference experiment with single photons produced by a single ^{87}Rb atom and a cold cloud of ^{87}Rb vapour without any use of spectral filtering. Our experiment demonstrates the compatibility of two different methods for generating single photons: triggering and heralding. The single atom generates a single photon through spontaneous emission after a triggered excitation by a short resonant optical pulse. A cold atomic ensemble generates narrowband time correlated photon pairs through a four wave mixing process, where the detection of one photon of the pair heralds the presence of the other.

5.2 Theory

We first present the theory of the HOM interference effect. In a HOM interferometer, two photons are incident on a 50:50 BS and the correlations between the two detectors at the output ports A and B are measured. If the two photons are indistinguishable, i.e. they are described by identical polarization, spatial, temporal, and spectral modes, the two photons will coalesce and leave the BS through the same output port. Thus the coincidence rate is zero, i.e. no photons are detected at both output ports simultaneously. If this indistinguishability gets reduced, i.e by changing temporal overlap, polarization, the coincidence rate increases.

We consider two input optical modes A_0 and B_0 of the beam splitter and output modes A and B as shown in the Figure 5.1. The creation operators of photons in A_0 and B_0 are labelled as $\hat{a}^\dagger_{A_0}$ and $\hat{a}^\dagger_{B_0}$, respectively. For a lossless 50:50 BS, the creation operators for the input modes are transformed into combination of creation operators for th output modes $\hat{a}^\dagger_A$ and $\hat{a}^\dagger_B$ via the relations

$$\hat{a}^\dagger_{A_0} = \frac{1}{\sqrt{2}}\,(\hat{a}^\dagger_A + \hat{a}^\dagger_B)\,, \tag{5.1}$$

$$\hat{a}^\dagger_{B_0} = \frac{1}{\sqrt{2}}\,(\hat{a}^\dagger_A - \hat{a}^\dagger_B)\,, \tag{5.2}$$

We can write the state of two simultaneously incident photons in modes A_0 and B_0 as

$$\hat{a}^\dagger_{A_0}\,\hat{a}^\dagger_{B_0}\,|\text{Vac}\rangle\,. \tag{5.3}$$

where $|\text{Vac}\rangle$ is the vacuum field state. Using relations 5.1 and 5.2 this become,

$$\hat{a}^\dagger_{A_0}\,\hat{a}^\dagger_{B_0}\,|\text{Vac}\rangle = \frac{1}{2}\left(\hat{a}^\dagger_A + \hat{a}^\dagger_B\right)\left(\hat{a}^\dagger_A - \hat{a}^\dagger_B\right)|\text{Vac}\rangle\,. \tag{5.4}$$

which be expanded to

$$\hat{a}^\dagger_{A_0}\,\hat{a}^\dagger_{B_0}\,|\text{Vac}\rangle = \frac{1}{2}\left(\hat{a}^\dagger_A\hat{a}^\dagger_A + \hat{a}^\dagger_B\hat{a}^\dagger_A - \hat{a}^\dagger_A\hat{a}^\dagger_B - \hat{a}^\dagger_B\hat{a}^\dagger_B\right)|\text{Vac}\rangle\,, \tag{5.5}$$

As $\hat{a}^\dagger_A$ and $\hat{a}^\dagger_B$ are orthogonal modes, they commute reducing the expression to

$$\begin{aligned}\hat{a}^\dagger_{A_0}\,\hat{a}^\dagger_{B_0}\,|\text{Vac}\rangle &= \frac{1}{2}\left(\hat{a}^\dagger_A\hat{a}^\dagger_A - \hat{a}^\dagger_B\hat{a}^\dagger_B\right)|\text{Vac}\rangle \\ &= \frac{1}{\sqrt{2}}\left(|2_A, 0_B\rangle - |0_A, 2_B\rangle\right)\,.\end{aligned} \tag{5.6}$$

This implies that two indistinguishable photons will always exit the beam-splitter through the same but random output port of the BS.

The indistinguishability of the two interfering photons is typically investigated by varying the arrival time of the photons at BS and measuring correlations between detectors at the output ports A and B. When there is a large difference in the photon arrival times, one will observe coincidence rate consistant with random distribution of the photons between the two outputs. As the difference in arrival times is reduced, the photons begin to interfere, thus reducing the number of correlations. This reaches a minimum when the photons arrive at the same time. This observation is often called as Hong-Ou-Mandel (HOM) dip [41]. In our experiment, the coherence time of the two interfering photons is of the order of few tens of nanoseconds, therefore we vary the temporal overlap between the two interfering photon's wavepackets to observe HOM dip.

5.3 Joint experimental setup

Figure 5.3 illustrates the joint experimental setup where a single photon from the single atom (SA) setup and a heralded single photon from four-wave mixing (FWM) setup interfere on a 50:50 BS in a HOM interferometer. Both interfering photons are resonant to $5S_{1/2}, F = 2 \rightarrow 5P_{3/2}, F = 3$ transition at 780 nm as shown in Figure 5.2. In the next sub-sections, we will provide an overview of the individual setups. The SA setup and HOM interferometer are located on same optical table, while FWM setup is located in an adjacent room at a distance of approximatively 15 m.

5.3.1 Four wave mixing setup

The experimental setup is similar to the one described in Chapter 4. After the trapping and cooling stages, the two pump beams, at 795 nm and 762 nm, excite the atoms from the $5S_{1/2}$, F = 2 ground level to the $5D_{3/2}, F = 3$ level via a two-photon transition. The 776 nm (signal) and 780 nm (idler) photon pairs emerge from a cascade decay back to the ground level and are coupled to single mode fibers. All four modes are collinear and propagate in the same direction. The cascade decay ensures that the temporal shape of the idler photon is an exponential decay, similar to the one emitted by a single atom via spontaneous emission. The detection of a signal photon by the APD D_T heralds the presence of a photon in the idler arm. The idler mode is a single photon state to a very good approximation [42]. (further details are written in the Appendix B). The detection of a signal photon also serves as a time reference for the generation of single

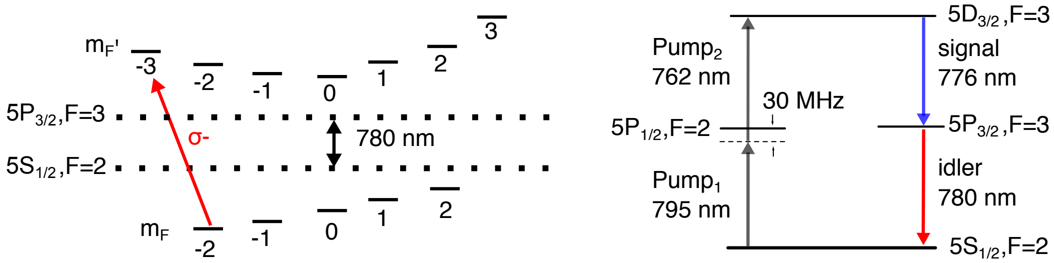

Figure 5.2: (Left) Closed transition along which the single atom is excited and spontaneously emits a single photon. (Right) Energy level diagram of ^{87}Rb showing the cascade decay scheme of the FWM process.

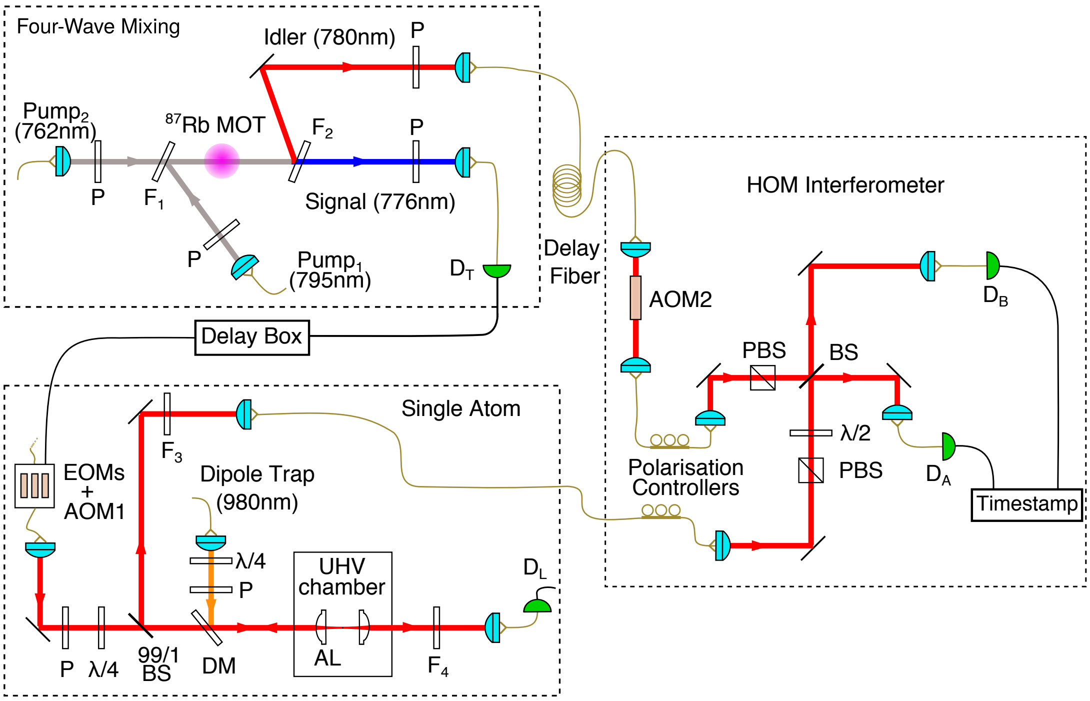

Figure 5.3: Schematic of the joint experimental setup: SA setup, FWM setup and HOM interferometer. Schematic overview of the experimental apparatus. P: polarizer, F_1 - F_4: Interference filters, $\lambda/2$, $\lambda/4$: half wave and quarter wave plate, PBS: polarizing Beam Splitter, BS: (Non-polarizing) Beam Splitter, AOM: Acousto-Optic Modulator, FPC: Fiber polarization Controllers, D$_T$, D$_L$, D$_A$, D$_B$: Avalanche photodiodes.

photons from the single atom setup, synchronizing the whole experiment. The idler photon is launched into a long fiber (230 m) and sent to HOM interferometer.

5.3.2 Single Atom setup

The details about the SA setup can be found in [8, 126, 127]. The setup consists of two confocal aspheric lenses of focal length of 4.5 mm enclosed in an ultra high vacuum chamber. The aspheric lens transforms a collimated laser beam into a diffraction-limited spot at the focus with a minimal spherical aberrations. A single ^{87}Rb atom is confined in a far-off resonant optical dipole trap (FORT) at 980 nm, tightly focussed by one of the aspheric lens. The presence of a single atom in the trap has been independently verified by measuring a second-order autocorrelation function $g^{(2)}(\tau)$ of the atomic fluorescence between two independent detectors, where τ is the detection time delay between the two detectors. We measure $g^{(2)}(\tau) < 0.5$ which is a signature of a single emitter [8].

We probe the closed $5\mathrm{S}_{1/2}, F = 2, m_F = -2 \rightarrow 5\mathrm{P}_{3/2}, F = 3, m_F = -3$ transition at 780 nm to excite the ^{87}Rb atom. Amongst the numerous methods to excite a single atom [128, 129], we use a square resonant π-pulse to transfer the atom efficiently from the ground to the excited state. The optical frequency of the pulse is tuned to be on resonance to the closed cycling transition using an Acousto-Optic Modulator (AOM1). The excitation process has to be much faster than the transition lifetime of 27 ns. Thus, we choose an excitation pulse of 3 ns duration with rise and fall times of <1 ns as shown in Figure 5.4 (Top). The excitation pulses are generated using Mach-Zehnder based electro-optic amplitude modulators (EOM), each with an extinction ratio of 21 dB. We use two synchronised EOMs in series with AOM1, which also acts as an additional optical switch in order to obtain a sufficiently large extinction ratio. This configuration minimizes the leakage of resonant light that can interact with the atom. The generation of an excitation pulse is triggered by the detection of a FWM signal photon at detector D_T.

The measured excitation probability (probability of having an atom in the excited state after the excitation process) is ≈ 0.8 using a π-pulse of 3 ns width. We collect $\approx 1\%$ of the spontaneously emitted photons into single mode fiber (without compensating for any losses) [127].

5.3.3 Hong-Ou-Mandel interferometer

A heralded single photon from the FWM setup and a single photon from the SA setup are sent to the HOM interferometer. The output modes of a 50:50, Non-polarizing Beam Splitter (BS) are coupled into single mode fibers which are connected to APDs, D_A and D_B. We ensure that both the photons are maximally indistinguishable in polarization, spatial, frequency and temporal modes.

- Polarization mode matching: We place a Fiber polarization Controller (FPC) and a PBS in each arm of the HOM interferometer. The FPC are set to maximize the transmission through each PBS. The PBS (in each arm) acts as a fixed polarization reference, ensuring that the transmitted light has parallel polarizations. The polarization of one of the input modes can be rotated with a HWP. Depending on the angle of the HWP, the two photons can be made to interfere (parallel polarizations) or not (orthogonal polarizations).

- Spatial mode matching: The spatial mode matching is done with a Mach-Zehnder interferometer constructed around the HOM interferometer as shown in Figure 5.5. A 780 nm laser beam is split by a fiber BS and sent to input arms of HOM interferometer. An optical path difference of a few cm is introduced by adding a free-space coupling link. The BS in HOM interferometer acts as the second BS of Mach-Zehnder interferometer where the two beams are combined. The passive instability of the free-space link introduces a sufficient variation in the optical path difference between the arms of the HOM to observe interference fringes on the timescale of few seconds. The two input beams have equal power and parallel polarizations at the BS. The measured interference visibility of $98.1\% \pm 1.5\%$ signifies a good spatial mode overlap between the two input modes of the HOM interferometer.

- Matching the frequency of the two photons: The single photons from both SA and FWM setups are derived from the $5P_{3/2} \rightarrow 5S_{1/2}$ transition in ^{87}Rb. However the resonance frequency of this transition is shifted by $\delta_{AC} = 76$ MHz in the single atom due to the combined AC stark shift caused by dipole trap and the Zeeman shift caused by the applied bias B-field. The FWM photon is not shifted from the natural resonance frequency. To compensate for this, the frequency of FWM photon is also shifted by 76 MHz with AOM2.

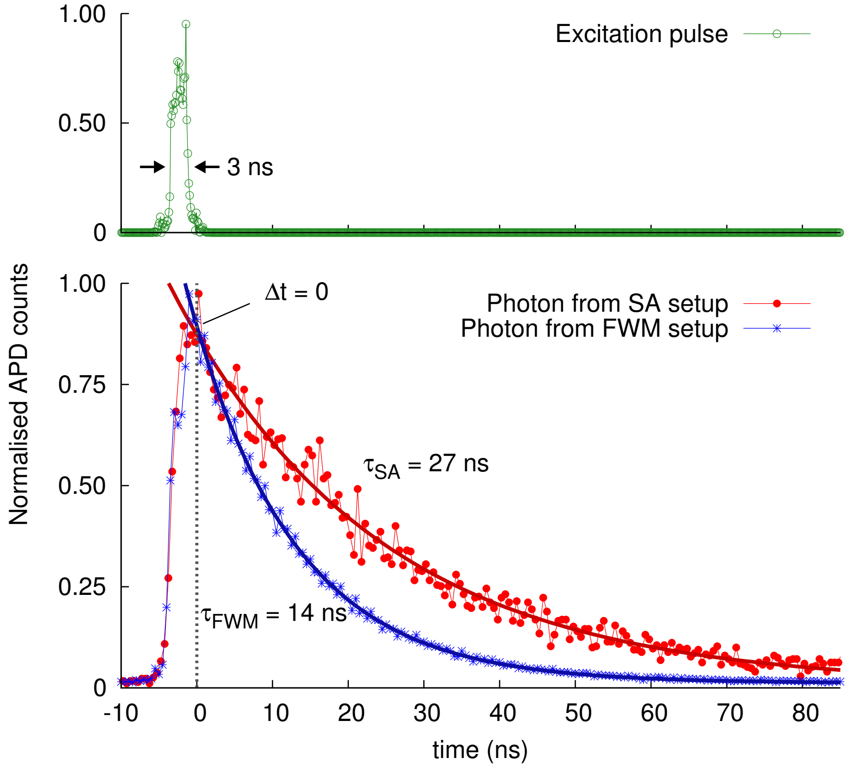

Figure 5.4: APD measurements, normalized to the peak of their detection time distributions. (Top) 3 ns pulse used to excite the single atom. (Bottom) Temporal profile of single photons from the single atom (SA) via spontaneous decay and from the atomic ensemble via four-wave mixing (FWM), with exponential fits showing decay times. The time delay Δt is measured from a time difference between the peak of detection time distributions of a SA photon and FWM photon. The $\Delta t = 0$ for this measurement, ensures that there is maximum overlap between the temporal envelopes of the SA photon and FWM photon.

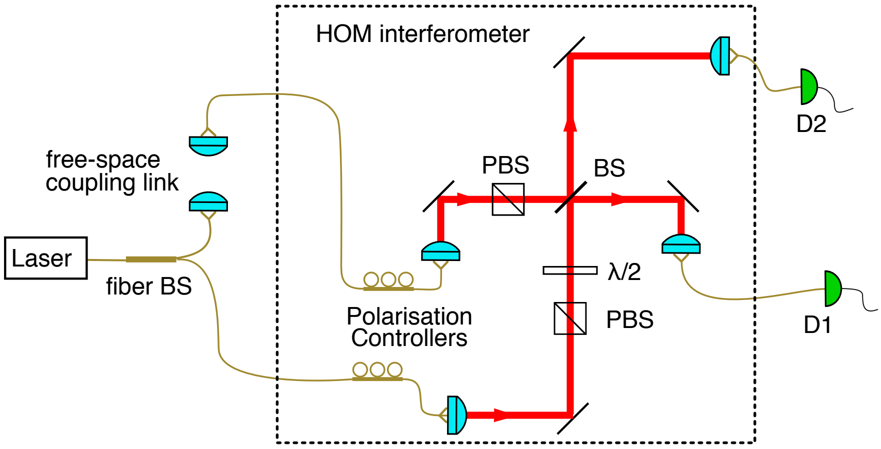

Figure 5.5: A Mach-Zehnder Interferometer constructed around the HOM interferometer is used to maximize the spatial mode overlap between the two arms of interferometer. $D_{1,2}$ are the photodetectors used to measure the interference fringes.

- Matching the temporal envelopes: In our experiment, both single photons have an exponentially decaying temporal envelopes. A maximal overlap of their temporal envelopes is achieved by matching their coherence times and arrival time distributions at the BS. The coherence time of the single photon from a single atom τ_{SA} is the natural lifetime of the $5P_{3/2} \rightarrow 5S_{1/2}$ transition. However, the coherence time of heralded idler photon τ_{FWM} is always shorter than τ_{SA} due to superradiance effects and can be tuned with the optical density (OD) of the atomic cloud as discussed in Chapter 3 . We can tune τ_{FWM} close to τ_{SA} by reducing the OD at the expense of decreasing the overall idler heralding efficiency. For this experiment, we set the OD such that $\tau_{FWM} = 14.1 \pm 0.1$ ns with an idler heralding efficiency of around 2% (without compensating for any losses) and rates of about 12 pairs/s. A comparison of the temporal profiles of both photons is shown in Figure 5.4. The measured characteristic decay time of single photon from a single atom $\tau_{SA} = 26.5$ ns is in agreement with the results reported in [130, 131].

- Matching the arrival times of the two photons: The arrival times of both photons must be carefully synchronised at the BS. In the SA setup (section 5.3.2), we use AOM1 as an additional optical switch to increase the extinction ratio. The response time of an AOM is limited by the time taken for the acoustic wave to

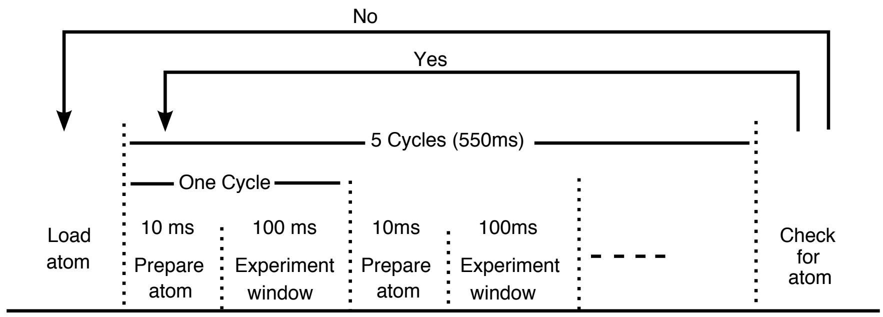

Figure 5.6: Timing sequence in the joint experiment.

travel from a transducer to the beam and propagate across it. In our setup, AOM1 takes a minimum of 615 ns to reach a stable ON state from a OFF state; only then we are ready to generate an excitation pulse with EOMs. This gives a relative time delay between FWM trigger sent to EOMs to generate excitation pulse and arrival of SA photon at the BS. To account for this and ensure that both photons reach BS around the same time, we delay the FWM idler photon by launching it into a 230 m long optical fiber to obtain a relative delay of 850 ns between arrival of FWM trigger at the SA setup and arrival of FWM photon at BS. Further fine tuning of the time delay between the two photons is done using a manual delay box. The time delay Δt, signifies the extent of the overlap between the temporal envelopes of SA and FWM photon and is measured from a time difference between the peaks of their detection time distributions as illustrated in Figure 5.4.

5.4 Experimental sequence

The main steps of the measurement sequence are:

- Loading a single atom from the MOT into the FORT. The loading time varies between 1 to 5 seconds.
- A state preparation period of 10 ms during which atom is optically pumped into $5S_{1/2}, F = 2, m_F = -2$ level.
- Experiment time window of 100 ms during which a FWM trigger signal from the FWM setup triggers an excitation pulse to the single atom.

- The steps 2 and 3 are repeated 4 times.
- The MOT beams are switched on to check if the atom is still in the FORT by monitoring fluoresence with detector D_L; if 'yes', start a new measurement sequence; otherwise discard the data collected in this sequence, turn on the MOT, and wait for another atom to be loaded into the FORT.

The FWM setup runs a continuos loop with a time window of $80\,\mu$s for cooling the atoms and $10\,\mu$s for generating photon pairs, not synchronised with above mentioned measurement steps.

5.5 Results

To measure Hong-Ou-Mandel Interference, we measure the coincidences between detector events on D_A and D_B with a condition that a trigger event on D_T is detected within a window of $0 \leq \Delta t_{TA} \leq 85\,$ns where Δt_{TA} is detection time difference between D_{T} and D_A[1]. We chose Δt_{TA} such that such that at maximum interference i.e at $\Delta t = 0$, more than 95% of the photons from the single-atom, and 99.5% of the photons from FWM is detected. We label these triple coincidences as $N_{AB|T}$. The coincidences are sorted into time bin of width 5 ns. We normalize $N_{AB|T}$ with the total number of trigger events N_T during the measurement time to obtain conditioned coincidence probability $P(\Delta t_{AB})$ of detecting a coincidence event

$$P(\Delta t_{AB}) = \frac{N_{AB|T}(\Delta t_{AB})}{N_T}\,, \tag{5.7}$$

where Δt_{AB} is the time difference between the detection events on D_A and D_B.

We first set the time delay $\Delta t = 0$ such that there is maximum temporal overlap (Figure 5.4) and measure coincidence probability $P_{||}(\Delta t_{AB})$ with the polarization of both the photons set to horizontal for maximum interference. We also measure the coincidence probability $P_{\perp}(\Delta t_{AB})$ when both photons have orthogonal polarizations and thus do not interfere. These results are shown in Figure 5.7.

For both the cases, we observe a time dependence (spread) in the coincidence probability because even though the photons arrive at the beam splitter at same time, they

[1] Actually Δt_{TA} is from t_f to $\mathrm{t}_f + 85\,$ns where t_f time delay due to long fiber (850 ns), since the fiber delay is fixed, we can ignore it for understanding.

can be detected in the different parts of their temporal envelopes (As photons are longer than the detector's resolution of 0.6 ns).

For a non interfering case, there is a large increase in the coincidence probability for a small $|\Delta t_{AB}|$ (of the same order of magnitude as the decay time of the single photons, i.e. 14 ns (FWM) and 26 ns (SA)) as compared to the interfering case. For $|\Delta t_{AB}| \gg 0$, the coincidence probability for both cases level off to the same level, which can be attributed to the background counts or accidentals. The dark counts of the detectors, thermal nature of the photons from the FWM source and uncorrected scattered light from FWM and SA setup contributes to a finite accidental coincidence probability.

Following the definition in [132], the HOM interference visibility is

$$V = 1 - \int_{T_c} \frac{P_{||}}{P_{\perp}} d(\Delta t_{AB}), \tag{5.8}$$

where T_c is the integration time window.

A large T_c reduces V due to an increased contribution from accidental coincidences, while a small T_c considers only a fraction of the HOM interference events. For subsequent data analysis, we chose T_c as the most appropriate time window which is comparable with the coherence times of both the photons. This is consistent with other similar HOM experiments [125, 132]. We measure $V = 66 \pm 4\%$ for an integration window $T_c = -25\,\text{ns} \leq \Delta t_{AB} \leq 25\,\text{ns}$ to reflect the longer of the two photon coherence times. An increase in visibility value of 84$\pm$5% is observed after correcting for accidental coincidences in this window. To correct for accidental coincidences, we take an average value of the background in Figure 5.7 from $200\,\text{ns} \leq \Delta t_{AB} \leq 700\,\text{ns}$ (individually for interfering and non interfering case) and subtract that value from $P_{||}(\Delta t_{AB})$ and $P_{\perp}(\Delta t_{AB})$ respectively in Equation 5.8. Our trigger rate is maintained between $150 - 200\,s^{-1}$. We further estimate the coincidence detection probability, given there is a trigger to be around 1.3×10^{-4} within an integration window of $T_c = -25\,\text{ns} \leq \Delta t_{AB} \leq 25\,\text{ns}$ [125].

Our reported visibility value is an improvement with respect to 16$\pm$3% (uncorrected for accidental coincidences) reported by Polyakov *et al.* for an interference between single photons from a PDC source and a quantum dot [44]. In an another experiment, that involves interference between heralded single photons from PPLN waveguide and microstructured fiber reports a visibility of about 70% (uncorrected for accidental coincidences) and 80% (after correction) [43].

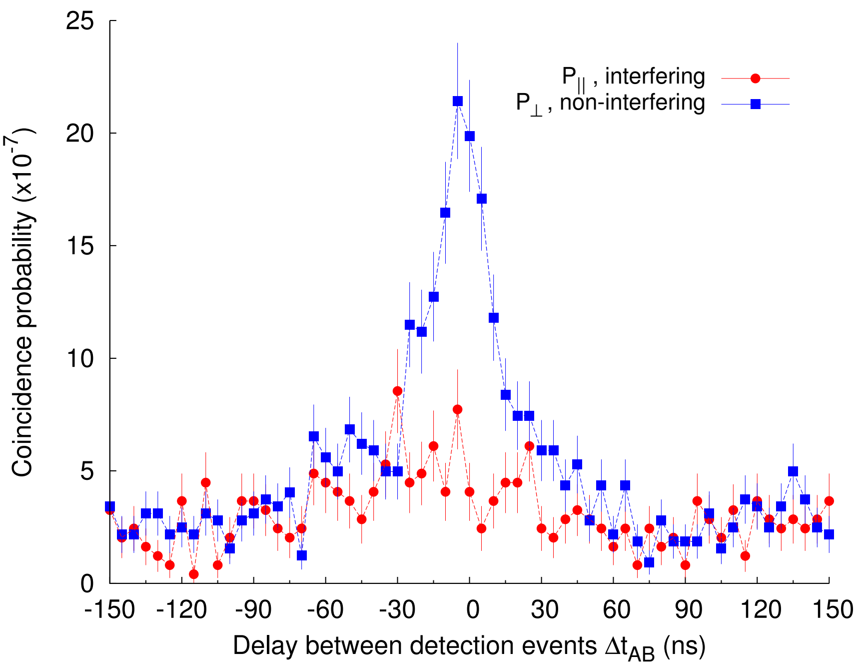

Figure 5.7: The histogram of coincidence probability ($P(\Delta t_{AB})$) obtained from triple coincidences between the detectors D_T, D_A and D_B normalized to the total number of triggers registered by D_T as a function of delay Δt_{AB} between the detection events on D_A and D_B. The temporal overlap is maximized with $\Delta t = 0$ for this measurement. The coincidences are resolved into time bin of width 5 ns. The blue squares show the non-interfering case: the photons from the FWM are horizontally polarized and the photons from the single atom are vertically polarized. The red circles shows the interfering case: both photons are horizontally polarized.

We next vary the time delay Δt to change the temporal overlap to observe a HOM dip. We tune the temporal overlap by varying the time delay of SA photon relative to FWM photon with the manual delay box while keeping the time delay between the FWM photon fixed with respect to FWM trigger. In previously reported measurements of the HOM dip, the coherence times of the photons were much shorter than the integration window, and the dip could be observed by using the same window for all the delays [41, 115, 116]. However, in our case T_c is comparable with the coherence time of the photons. Therefore, the choice of T_c depends on the time delay Δt.

To explain this more clearly, we compare three cases when the time delay is $|\Delta t| = 0$, 14 ns and 30 ns. Figure 5.8 illustrates conditional probability $P_{||}(\Delta t_{AB})$ for these three time delay values. We observe that for the time delays $|\Delta t| > 0$, two new peaks start to appear in $P_{||}(\Delta t_{AB})$. The origin of the twin peaks can be understood from Figure 5.9: a coincidence event will be registered at the detectors D_A and D_B, if both the photons are either transmitted or reflected at the BS. An equal probability of the two scenarios will manifest a twin peak in $P_{||}(\Delta t_{AB})$ separated by a time delay of $2\,\Delta t$. Therefore, for all the delays, T_c has to be moved to be centered around the peaks as shown in shaded regions in Figure 5.8 such that

a) For $\Delta t = 0$, we take a continuos window of $-25\,\text{ns} \leq \Delta t_{AB} \leq 25\,\text{ns}$.

b) For all delays $|\Delta t| < 25\,\text{ns}$, we take an integration window of $(-|\Delta t| - 25\,\text{ns}) \leq \Delta t_{AB} \leq (|\Delta t| + 25\,\text{ns})$.

c) For all delays $|\Delta t| > 25\,\text{ns}$ the window is split into two regions $\pm 25\,\text{ns}$ wide around the peaks.

Once we decide on integration window T_c in $P_{||}(\Delta t_{AB})$, we obtain normalized coincidence probability for different time delays Δt as

$$P^n(\Delta t) = \frac{\int\limits_{T_c} P_{||,\Delta t}(\Delta t_{AB})d(\Delta t_{ab})}{\int\limits_{-25\text{ns}}^{25\text{ns}} P_{\perp,\Delta t=0}(\Delta t_{AB})d(\Delta t_{AB})}\,, \tag{5.9}$$

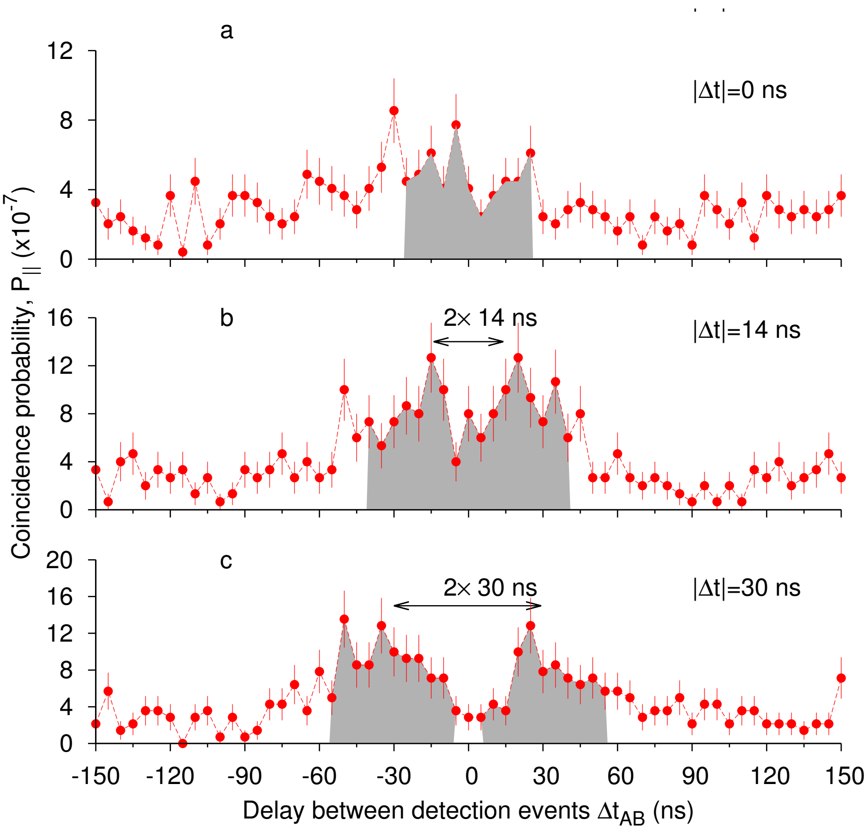

Figure 5.8: The coincidence probability $P_{||}(\Delta t_{AB})$ for $|\Delta t| = 0$, 14 ns and 30 ns. The two peaks at $\Delta t_{AB} = \pm\Delta t$ is from the two possible situations to observe coincidences is shown in Figure 5.9. The integration window T_c for $P_{||}(\Delta t_{AB})$ for each delay is shown as grey shaded region.

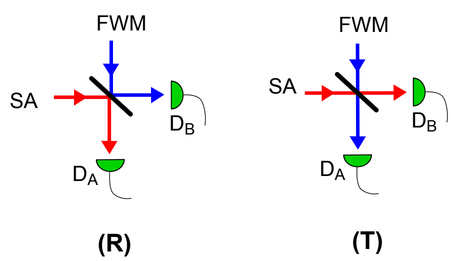

Figure 5.9: The two situations that can result in a coincidence between the detectors D_A and D_B: (R) Both the photons are reflected at the BS. (T) Both the photons are transmitted through the BS.

The normalization term in the denominator of Equation (5.9) is obtained from the $P_{\perp}(\Delta t_{AB})$ shown in Figure 5.7 with an integration window T_c of $-25, \text{ns} \leq \Delta t_{AB} \leq 25\,\text{ns}$ for all the delays. The visibility V for each delay is $V = 1 - P^n$.

The plot of normalized probability $P^n(\Delta t)$ as a function of the time delay Δt without correcting for the accidentals is shown in the Figure 5.11. We observe that for $|\Delta t| \gg 0$, $P^n(\Delta t)$ tends to 1.3 instead of 1. This is because of we take unequal values of the total accidental background for each delay. For instance, when $|\Delta t| = 30\,\text{ns}$. we double count accidental background as compared to the case $\Delta t = 0$ in $P_{||}(\Delta t_{AB})$ of Equation 5.9[1]. We observe that when we subtract for accidental coincidences for each time delay, the value of $P^n(\Delta t)$ reaches 1 for $|\Delta t| \gg 0$ as shown in the Figure 5.10.

5.6 Conclusion

We have demonstrated HOM interference between two single photons produced by two different physical systems: a single atom and a cold atomic ensemble. The behaviour of the HOM interference is examined for different time delays between the two photons. The two photons produced by our systems are already compatible in temporal shape and bandwidth, thus eliminating the need for spectral filter.The measured interference visibility is (well beyond the classical limit of 50%, [133]) is 66±4% without any accidental correction and 84±5% with accidental correction. Our results are a step towards implementing a quantum network especially in the applications where two different physical systems are required to serve as different nodes of the network.

[1]For $|\Delta t| = 30\,\text{ns}$ we take longer T_c, and therefore larger accidental background as compared to the case when $\Delta t = 0$

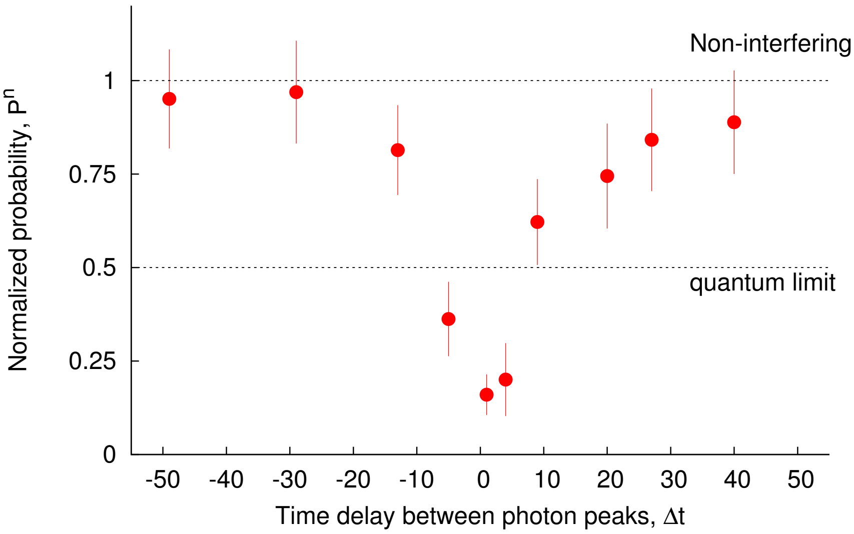

Figure 5.10: Normalized probability $P^n(\Delta t)$ as a function of the delay Δt between the peaks of detection time distributions of the two photons (HOM dip). For each point $P^n(\Delta t)$ is obtained after correcting for the accidental background.

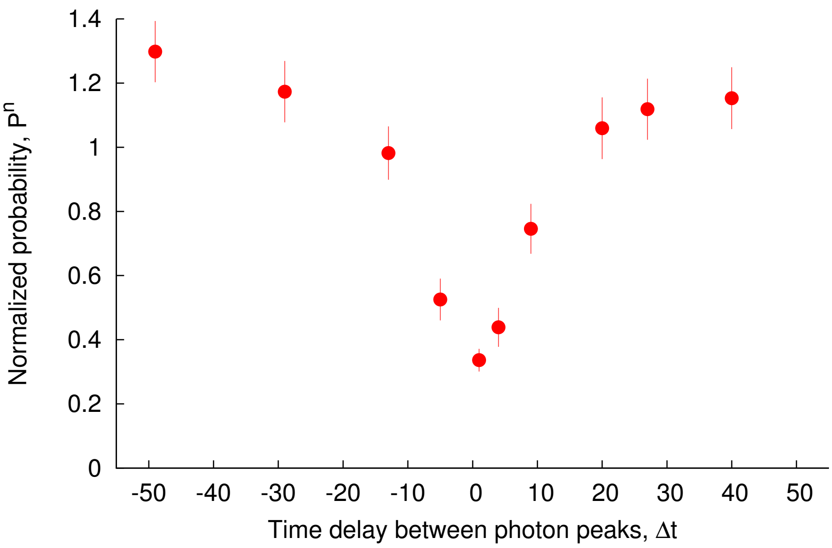

Figure 5.11: The same plot as above but without subtracting the accidental background.

Chapter 6

Conclusion and outlook

We have presented a source of narrowband, time-correlated photon pairs generated via non-degenerate four-wave mixing using a cascade level scheme in a cold ensemble of ^{87}Rb atoms. The bandwidth of the generated photons is tunable from 10 MHz–30 MHz by changing the optical density of the atomic cloud. The comparison between the measured frequency bandwidth and $1/e$ decay time of $g^{(2)}$ indicates a transform-limited spectrum of the generated photon pairs. Coupling the photon pairs into single mode fibers, we observe an instantaneous rate of 20,000 pairs per second with silicon avalanche photodetectors. The detection events exhibit a strong correlation in time [$g^2(\Delta t_{\mathrm{SI}} = 0) = 14600$] and a coupling efficiency indicated by a pair-to-single ratio of 17%. The violation of the Cauchy-Schwarz inequality by a factor of 50×10^6 indicates a strong non-classical correlation between the generated fields, while a Hanbury-Brown-Twiss experiment in the individual photons reveals their thermal nature. The generated photon pairs are also entangled in the polarization degree of freedom. The purity of the resultant polarization entangled state P=tr[ρ]=0.98±0.01 is close to a pure state even though the atomic ensemble is prepared in an ill-defined statistical mixture of magnetic sublevels by the magneto-optical cooling/trapping process. The narrow bandwidth and brightness makes our source a prime candidate for interfacing with ^{87}Rb atoms, a common workhorse for quantum memories.

We are currently working towards interfacing our photons with a single ^{87}Rb atom in an optical dipole trap in free space. As a first step, we have performed a Hong-Ou-Mandel (HOM) interference experiment to show that a heralded single photon from our source is indistinguishable from a single photon emitted by a single atom. The measured interference visibility of 66.4% without any accidental correction and 84.5%

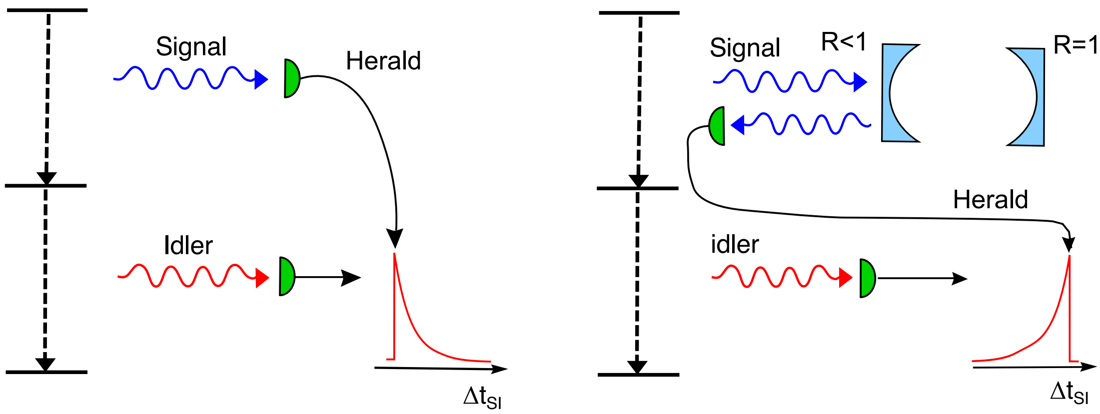

Figure 6.1: Concept of time reversal of the heralded photons using an asymmetric cavity. (Left) Temporal profile of the heralded idler photons without the cavity as presented in Chapter 3. (Right) In the presence of an asymmetric cavity in the signal mode, the temporal profile of heralded idler photon is reversed.

with accidental correction is well beyond the classical limit of 50%. The HOM experiment also provides a better understanding to what extent heralded photons can be considered equivalent to 'true' single photons as in that case they should in principle be efficiently absorbed by a single atom in free-space in a time-reversed Weisskopf-Wigner situation.

6.1 Time reversal of the heralded photons

Efficient absorption of a single photon by a single atom also requires that the temporal profile of the incoming photons should match the time reversal of photons generated by spontaneous decay from the transition of interest [134, 135]. In a separate experiment with our photon pair source, we have demonstrated a way to prepare heralded single photons with a temporal envelope that resembles the time reversal of photons from the spontaneous decay process. The detailed description of this experiment can be found in [72, 136]. Here, we will briefly discuss the concept of how a cavity can be used to reverse the temporal envelope of the heralded photons as illustrated in Figure 6.1. An asymmetric cavity with an end mirror of unit reflectivity and other partially reflecting mirror can transform an incident photon with an exponentially rising envelope into an exponential decaying envelope given that the ring down time of the cavity matches the

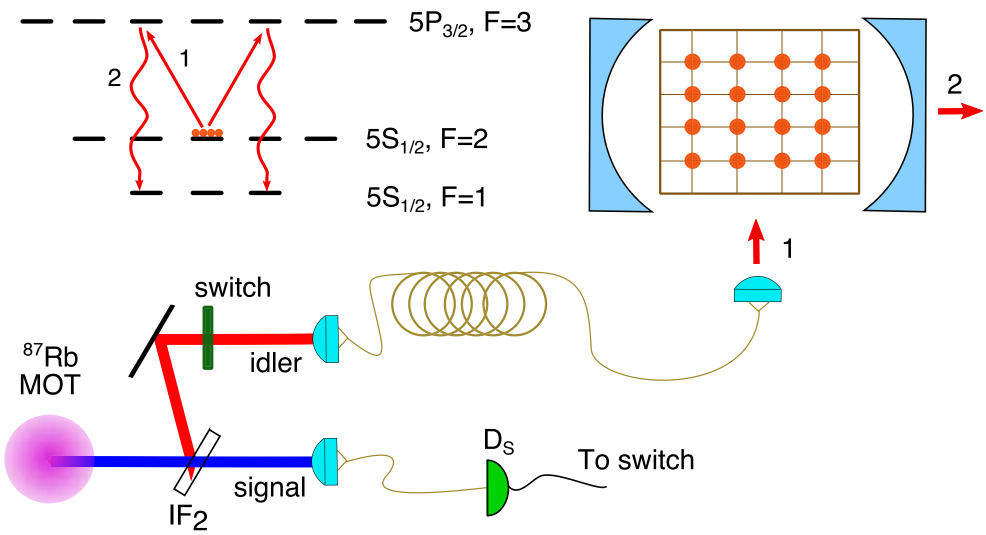

Figure 6.2: Schematic of proposed experiment to establish an interface between photon pairs from our source with cavity quantum electrodynamics (CQED) system. An idler photon (1) from our source with an encoded polarization qubit is absorbed by an ensemble of ^{87}Rb atoms initially prepared in the hyperfine ground state $|F = 2, m_F = 0\rangle$ inside a high finesse cavity. Emission of a π polarized photon (2) into the cavity mode heralds the transfer of the atomic ensemble to a collective state with one atom in a superposition of the $|F = 2, m_F = \pm 1\rangle$ states. An optical switch in the idler mode is turned on only when heralding photon (signal) is detected by D_S.

coherence time of the photons. The idea was first experimentally demonstrated by [137] using attenuated coherent pulses. Using such a cavity with our photon pairs, we have obtained a exponential rising shaped temporal envelope of the single photon resonant with the ground state transition. One of the proposed future experiments would be to study how the remote manipulation of temporal envelope of the generated photons with an asymmetric cavity can affect the absorption of photons by an atom.

6.2 Towards hybrid quantum systems

Another proposed future experiment is to interface polarization entangled photon pairs from our source with a cavity quantum electrodynamics (CQED) system developed in our Centre [138, 139]. The two sources are located at a distance of 50 m apart. The CQED system hosts an ensemble of ^{87}Rb atoms in a superlattice structure. The lattice structure enables photons from an optical mode entering the cavity sideways to scatter superradiantly into the cavity mode. The bandwidth of our entangled photons is suitable for absorption by the atoms inside cavity. A simplified schematic of such an experiment is illustrated in Figure 6.2. The experiment of interest would be to investigate how efficiently the polarization state of a photon can be transferred, stored, and subsequently retrieved from the collective state of the atoms in CQED system [25].

Appendix A

Rubidium transition lines

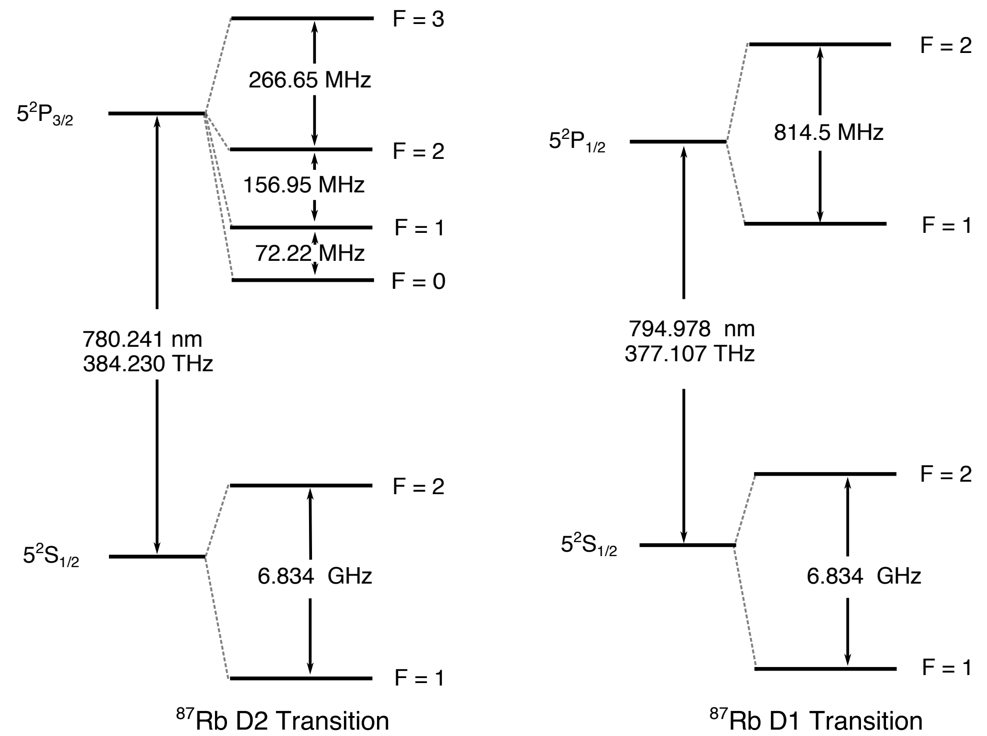

Figure A.1: (a) Hyperfine structure of the D1 and D2 transition in ^{87}Rb atom [3]

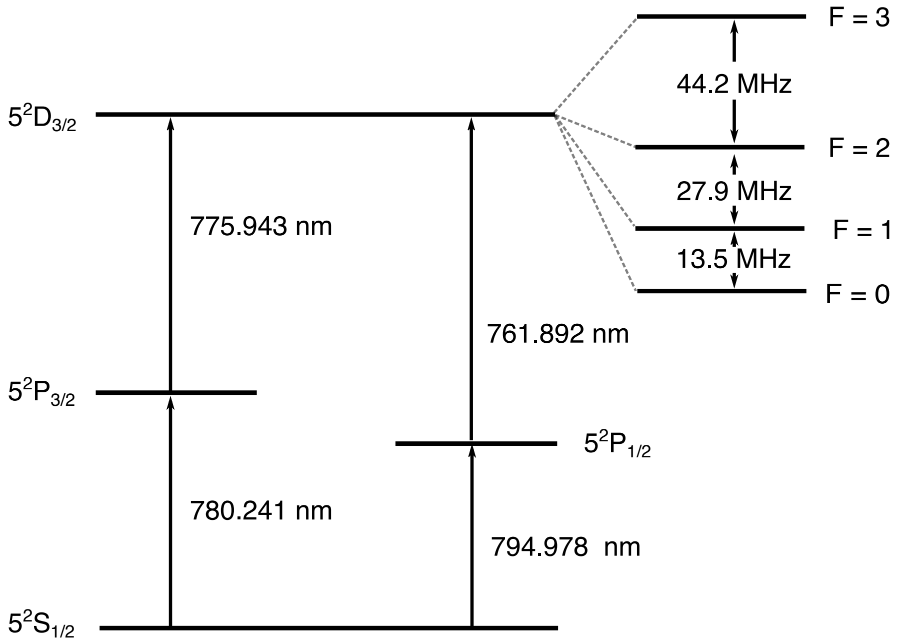

Figure A.2: (a) Hyperfine structure of $5D_{3/2}$ level in ^{87}Rb atom [4]

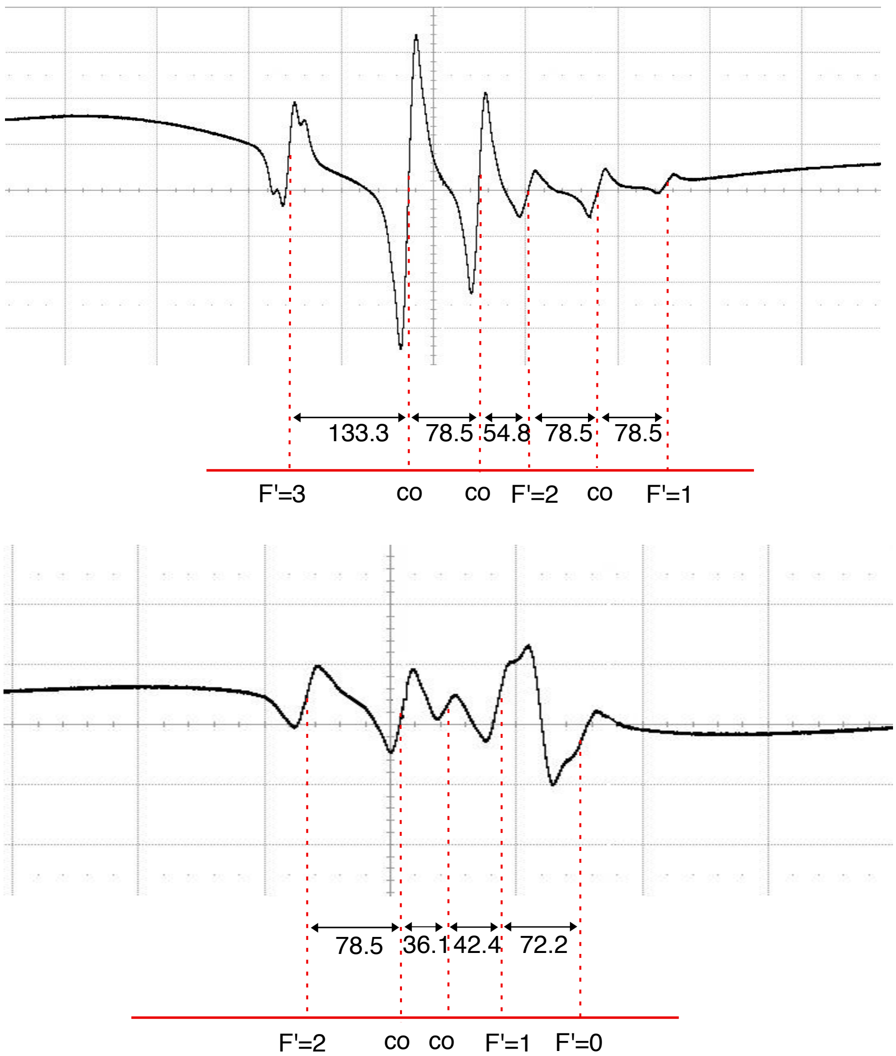

Figure A.3: Spectroscopy error signal of the 780 nm laser corresponding to ^{87}Rb D2 line. The hyperfine lines (F′) and the cross-over lines (co) from $5S_{1/2}, F = 2$ level (Top) and $5S_{1/2}, F = 1$ level (bottom). The separation frequency (in MHz) between the adjacent lines is indicated.

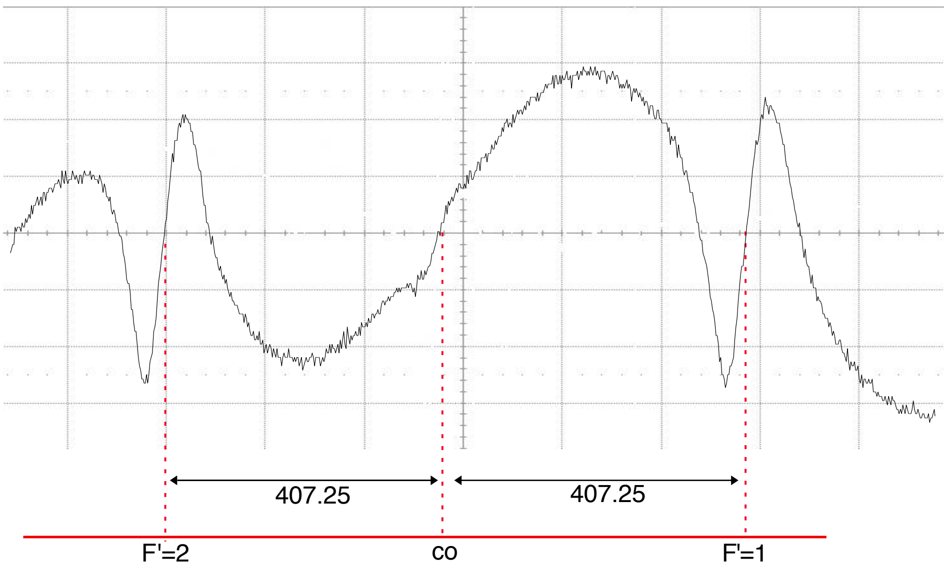

Figure A.4: Spectroscopy error signal of the 795 nm laser corresponding to ^{87}Rb D1 line. The hyperfine lines (F$'$) and the cross-over lines (co) are from $5S_{1/2}, F = 2$ level. The separation frequency (in MHz) between the adjacent lines is indicated.

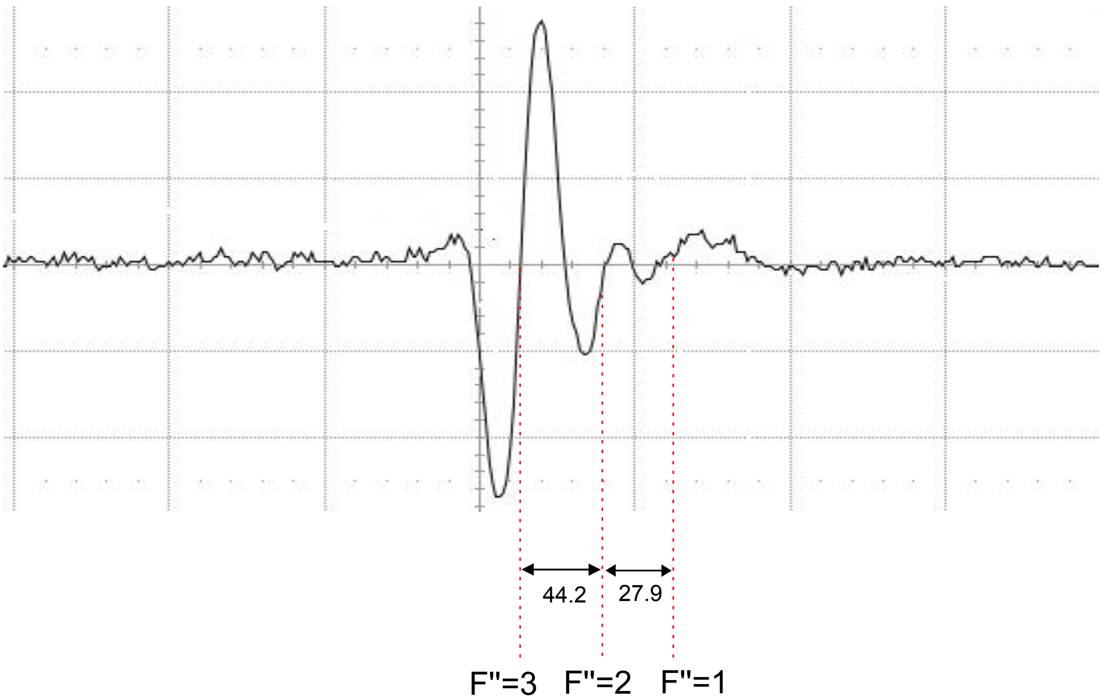

Figure A.5: Spectroscopy error signal of the 762 nm laser. To resolve the hyperfine lines, we first use a 795nm laser on resonant to $5S_{1/2}, F = 2 \rightarrow 5P_{1/2}, F' = 2$ as a pump. Another laser at 762 nm is used in a counter-propagating direction as a probe. The hyperfine lines illustrated in the figure correspond to allowed transitions from $5P_{1/2}, F' = 2$ level to different hyperfine levels of $5D_{3/2}$. The separation frequency (in MHz) between the adjacent lines is indicated.

Appendix B

Photon pairs to heralded single photons

Time correlated photon pairs are a source of heralded single photons, where detection of one photon of the pair heralds the preparation of a single photon in the other mode. Heralded single photons have been produced from various physical systems such as non-linear optical crystal [140], atomic ensembles [141], photonic crystal fibers [142], Si waveguides [143]. In this Chapter, we will demonstrate the single photon character of our heralded photons. A more detailed description of the experiment can be found in [42, 72].

Unlike single quantum emitters [144, 145, 146], the probability of generating more than one photon per heralding event in a parametric process does not vanish due to the thermal nature of the emission process from the atomic ensemble [71]. We consider the second order correlation function $g^{(2)}(\Delta t_{12})$ for the probability of observing two photons in a given mode with a time difference Δt_{12}. Any classical light field exhibits $g^{(2)}(0) \geq 1$, while $g^{(2)}(\Delta t_{12}) < 1$ is referred to as photon antibunching, with an ideal single photon source reaching $g^{(2)}(0) = 0$ [70].

We determine this correlation function experimentally in a Hanbury-Brown–Twiss (HBT) geometry, where the idler light (795 nm) is distributed with a 50:50 fiber beam splitter (FBS) onto two single photon counting silicon avalanche detectors (APD) $D_{\mathrm{i1}}, D_{\mathrm{i2}}$ while signal photons (762 nm) are detected by D_{s} as heralds.

As demonstrated in Chapter 3, the correlation function between the signal and idler $g^{(2)}_{si}(\Delta t_{si})$ has the shape of a decreasing exponential, with more than 98% of the coincidences occuring within a time window T_c=30 ns. We record a histogram

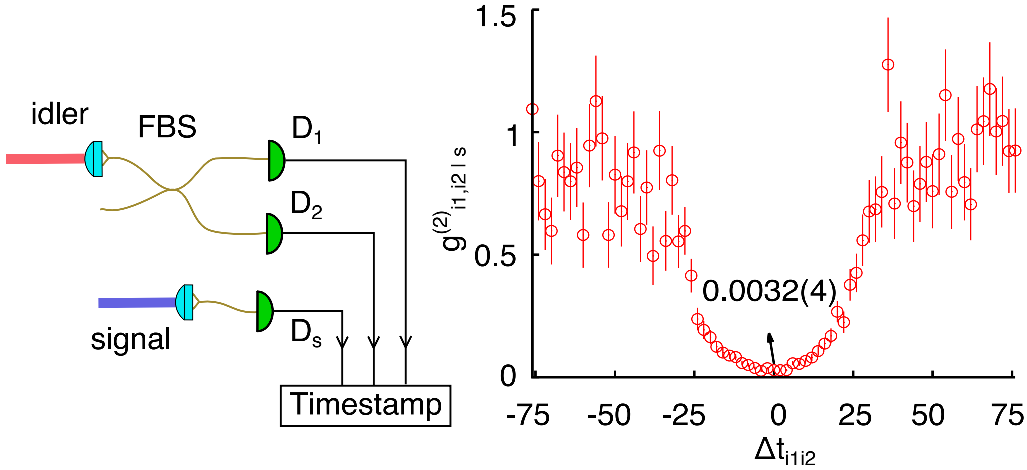

Figure B.1: (Left) Experimental setup for HBT experiment. (Right) The correlation function $g^{(2)}_{i1i2|s}$ of idler photons separated by a time difference Δt_{12}, conditioned on detection of a heralding event in the signal mode, shows strong photon antibunching over a time scale of $\pm 20\,$ns, indicating the single photon character of the heralded photons. The error bars indicate the propagated poissonian counting uncertainty from $G^{(2)}_{i1i2|s}$ and $N_{i1i2|s}$.

$G^{(2)}_{\mathrm{i1i2|s}}(\Delta t_{12})$ of idler detection events on D_{i1} and D_{i2} with a time difference $\Delta t_{12} = t_2 - t_1$ if one of them occurs within a coincidence time window T_c after the detection of a heralding event in the signal mode. The normalized correlation function of heralded coincidences between the two idler modes is

$$g^{(2)}_{\mathrm{i1i2|s}}(\Delta t_{12}) = G^{(2)}_{\mathrm{i1i2|s}}(\Delta t_{12})/N_{i1i2|s}(\Delta t_{12}), \tag{B.1}$$

where $N_{i1i2|s}(\Delta t_{12})$ is the estimated number of accidental coincidences. Due to the strong temporal correlation between signal and idler photons, the probability of accidental coincidences is not uniform. We thus estimate $N_{i1i2|s}(\Delta t_{12})$ for every Δt_{12} by integrating the time difference histograms between the signal and each arm of the HBT, $G^{(2)}_{si1}(\Delta t_{si})$ and $G^{(2)}_{si2}(\Delta t_{si})$ within T_c normalized to the total number of triggers N_s. Due to the time ordering of the cascade process, it is only meaningful to consider positive time delays after the detection of the heralding photon, thus splitting $N_{i1i2|s}$

into two cases. For $\Delta t_{12} \geq 0$, we use

$$N^{(+)}_{i1i2|s}(\Delta t_{12}) = \frac{1}{N_s} \int\limits_0^{T_c} G^{(2)}_{si1}\left(\Delta t_{si}\right) G^{(2)}_{si2}\left(\Delta t_{si} + \Delta t_{12}\right)\ d\Delta t_{si} \tag{B.2}$$

while for $\Delta t_{12} < 0$, we use

$$N^{(-)}_{i1i2|s}(\Delta t_{12}) = \frac{1}{N_s} \int\limits_0^{T_c} G^{(2)}_{si1}\left(\Delta t_{si} + \Delta t_{12}\right) G^{(2)}_{si2}\left(\Delta t_{si}\right)\ d\Delta t_{si}. \tag{B.3}$$

The resulting $g^{(2)}_{\mathrm{i1i2|s}}(\Delta t_{12})$ is shown in Figure B.1 as function of the delay Δt_{12}, sampled into 2 ns wide time bins. With a signal photon detection rate of $50000\,\mathrm{s}^{-1}$ (at $\Delta_2 = 0$), we observe $g^{(2)}_{\mathrm{i1i2|s}}(0) = 0.032 \pm 0.004$. When switching the roles of the signal and idler arms, we observe $g^{(2)}_{\mathrm{s1s2|i}}$ of 0.018 ± 0.007 with an idler photon detection rate of $13000\,\mathrm{s}^{-1}$.

In both the cases we see a clear signature of antibunching with $g^{(2)}(0) << 1$. This shows that we prepare a very good approximation of an ideal single photon state in the idler mode upon the detection of a heralding photon in the signal mode, and vise versa.

Appendix C

Density matrices

A system containing n qubits is represented by a 2^n square density matrix, which has 4^n-1 free parameters. Hence, 4^n projective measurements are required for quantum state tomography of such a system. Therefore, in the case of a two qubit system, 16 measurements are needed. These measurements, consisting of projections onto the 16 vectors $|\psi_\nu\rangle$ are complete if and only if the 16×16 matrix with elements

$$B_{\mu,\nu} = \langle\psi_\nu|\ |\hat{\Gamma}_\mu|\ |\psi_\nu\rangle \tag{C.1}$$

is nonsingular[101]. The $\hat{\Gamma}_\mu$ are the set of matrices $\hat{\sigma}_i \otimes \hat{\sigma}_j$ with $i,j = 0,1,2,3$, where σ_0 is 2×2 identity, and other $\hat{\sigma}_i$ are Pauli matrices. The normalised density matrix is given by

$$\hat{\rho} = \frac{\sum\limits_{\nu=1}^{16}\left[\sum\limits_{\nu=1}^{16}(B^{-1})_{\nu,\mu}\,\hat{\Gamma}_i\right] n_\nu}{\sum\limits_{\nu=1}^{4} n_\nu} \tag{C.2}$$

where n_ν is the number of counts for $|\psi_\nu\rangle$ measurement. This method thus provides a simple way of calculating an estimate of a quantum state given the appropriate measurements. The details about tomographic reconstruction method is discussed in [101]. Using this method we reconstruct density matrices of the polarisation entangled state of photon pairs for decay path X and Y as

For the decay path X

$$\rho_X = \begin{pmatrix} 0.0044 & -0.01491 - 0.0428i & -0.02915 + 0.0292i & 0.0252 + 0.01356i \\ -0.0149 + 0.0428i & 0.3241 & -0.4106 - 0.0589i & -0.0010 - 0.0653i \\ -0.0291 - 0.0292i & -0.4106 + 0.0589i & 0.6670 & 0.0094 + 0.0700i \\ 0.0252 - 0.0135i & -0.001 + 0.0653i & 0.0094 - 0.07i & 0.0043 \end{pmatrix} \tag{C.3}$$

For the decay path Y

$$\rho_Y = \begin{pmatrix} 0.0058 & -0.0455 - 0.0923i & 0.0080 + 0.0627i & 0.0242 - 0.0217i \\ -0.0455 + 0.0923 & 0.61204 & -0.4473 + 0.0105i & 0.0242 - 0.0649i \\ 0.0080 - 0.0627 & -0.4473 - 0.0105i & 0.3759 & -0.0464 + 0.0377i \\ 0.0242 + 0.0217i & 0.0242 + 0.0649i & -0.0464 - 0.0377i & 0.0061 \end{pmatrix} \tag{C.4}$$

References

[1] A. Walther, A. Amari, S. Kröll, and A. Kalachev. **Experimental superradiance and slow-light effects for quantum memories**. *Phys. Rev. A*, **80**:012317, Jul 2009.

[2] H H Jen. **Spectral analysis for cascade-emission-based quantum communication in atomic ensembles**. *J. Phys. B: At. Mol. Opt. Phys.*, **45**:165504, 2012.

[3] D.A. Steck. **Rubidium 87 D line data**, 2001.

[4] **NIST Atomic Spectra Database**.

[5] A. Einstein. **ber einen die Erzeugung und Verwandlung des Lichtes betreffenden heuristischen Gesichtspunkt**. *Annalen der Physik*, **322**(6):132–148, 1905.

[6] Gilbert N. Lewis. **The Conservation of Photons**. *Nature*, **118**:874–875, 1926.

[7] Jr. Lamb, W.E. **Anti-photon**. *Applied Physics B*, **60**(2-3):77–84, 1995.

[8] Meng Khoon Tey, Zilong Chen, Syed Abdullah Aljunid, Brenda Chng, Florian Huber, Gleb Maslennikov, and Christian Kurtsiefer. **Strong interaction between light and a single trapped atom without the need for a cavity**. *Nature Physics*, **4**:924–927, 2008.

[9] R Alleaume, F Treussart, G Messin, Y Dumeige, J-F Roch, A Beveratos, R Brouri-Tualle, J-P Poizat, and P Grangier. **Experimental open-air quantum key distribution with a single-photon source**. *New Journal of Physics*, **6**(1):92, 2004.

[10] Rosa Brouri, Alexios Beveratos, Jean-Philippe Poizat, and Philippe Grangier. **Photon antibunching in the fluorescence of individual color centers in diamond**. *Opt. Lett.*, **25**(17):1294–1296, Sep 2000.

[11] Christian Maurer, Christoph Becher, Carlos Russo, Jrgen Eschner, and Rainer Blatt. **A single-photon source based on a single Ca + ion**. *New Journal of Physics*, **6**(1):94, 2004.

[12] Charles Santori, Matthew Pelton, Glenn Solomon, Yseulte Dale, and Yoshihisa Yamamoto. **Triggered Single Photons from a Quantum Dot**. *Phys. Rev. Lett.*, **86**:1502–1505, Feb 2001.

[13] P. Michler, A. Kiraz, C. Becher, W. V. Schoenfeld, P. M. Petroff, Lidong Zhang, E. Hu, and A. Imamoglu. **A Quantum Dot Single-Photon Turnstile Device**. *Science*, **290**(5500):2282–2285, 2000.

[14] J. McKeever, A. Boca, A. D. Boozer, R. Miller, J. R. Buck, A. Kuzmich, and H. J. Kimble. **Deterministic Generation of Single Photons from One Atom Trapped in a Cavity**. *Science*, **303**(5666):1992–1994, 2004.

[15] E. Moreau, I. Robert, J. M. Grard, I. Abram, L. Manin, and V. Thierry-Mieg. **Single-mode solid-state single photon source based on isolated quantum dots in pillar microcavities**. *Applied Physics Letters*, **79**(18):2865–2867, 2001.

[16] Bharath Srivathsan, Gurpreet Kaur Gulati, Brenda Chng, Gleb Maslennikov, Dzmitry Matsukevich, and Christian Kurtsiefer. **Narrow Band Source of Transform-Limited Photon Pairs via Four-Wave Mixing in a Cold Atomic Ensemble**. *Phys. Rev. Lett.*, **111**:123602, 2013.

[17] John F. Clauser, Michael A. Horne, Abner Shimony, and Richard A. Holt. **Proposed Experiment to Test Local Hidden-Variable Theories**. *Phys. Rev. Lett.*, **23**:880–884, Oct 1969.

[18] Alain Aspect, Philippe Grangier, and Gérard Roger. **Experimental Realization of Einstein-Podolsky-Rosen-Bohm *Gedankenexperiment* : A New Violation of Bell's Inequalities**. *Phys. Rev. Lett.*, **49**:91–94, Jul 1982.

[19] Edward S. Fry and Randall C. Thompson. **Experimental Test of Local Hidden-Variable Theories**. *Phys. Rev. Lett.*, **37**:465–468, Aug 1976.

[20] Michael A. Nielsen and Isaac L. Chuang. *Quantum Computation and Quantum Information.* Cambridge University Press, 1 edition, January 2004.

[21] D. Bouwmeester, A.K. Ekert, and A. Zeilinger. *The Physics of Quantum Information: Quantum Cryptography, Quantum Teleportation, Quantum Computation.* Springer, 2010.

[22] Artur K. Ekert. **Quantum cryptography based on Bell's theorem**. *Phys. Rev. Lett.*, **67**:661–663, Aug 1991.

[23] Nicolas Gisin, Grégoire Ribordy, Wolfgang Tittel, and Hugo Zbinden. **Quantum cryptography**. *Rev. Mod. Phys.*, **74**:145–195, Mar 2002.

[24] A. Stute, B. Casabone, B. Brandstätter, K. Friebe, T. E. Northup, and R. Blatt. **Quantum-state transfer from an ion to a photon**. *Nature Photonics*, **advance online publication**, 2013.

[25] Stephan Ritter, Christian Noelleke, Carolin Hahn, Andreas Reiserer, Andreas Neuzner, Manuel Uphoff, Martin Muecke, Eden Figueroa, Joerg Bochmann, and Gerhard Rempe. **An elementary quantum network of single atoms in optical cavities**. *Nature*, **484**:195–200, 2012.

[26] Tatjana Wilk, Simon C. Webster, Axel Kuhn, and Gerhard Rempe. **Single-Atom Single-Photon Quantum Interface**. *Science*, **317**:488–490, 2007.

[27] A. Kuzmich, W. P. Bowen, A. D. Boozer, A. Boca, C. W. Chou, L.-M. Duan, and H. J. Kimble. **Generation of nonclassical photon pairs for scalable quantum communication with atomic ensembles**. *Nature*, **423**:731–734, 2003.

[28] James K. Thompson, Jonathan Simon, Huanqian Loh, and Vladan Vuleti. **A High-Brightness Source of Narrowband, Identical-Photon Pairs**. *Science*, **313**(5783):74–77, 2006.

[29] H. J. Kimble. **The quantum internet**. *Nature*, **453**:1023–1030, 2008.

[30] L.-M. Duan, M. D. Lukin, J. I. Cirac, and P. Zoller. **Long-distance quantum communication with atomic ensembles and linear optics**. *Nature*, **414**:413–418, 2001.

[31] Christian Kurtsiefer, Markus Oberparleiter, and Harald Weinfurter. **High-efficiency entangled photon pair collection in type-II parametric fluorescence**. *Phys. Rev. A*, **64**:023802, Jul 2001.

[32] T Kim F N C Wong and J H Shapiro. **Efficient generation of polarization-entangled photons in a nonlinear crystal**. *Laser Phys.*, **16**:1517–1524, 2006.

[33] A. Haase, N. Piro, J. Eschner, and M. W. Mitchell. **Tunable narrowband entangled photon pair source for resonant single-photon single-atom interaction**. *Opt. Lett.*, **34**:55–57, 2009.

[34] F. Wolfgramm, X. Xing, A. Cerè, A. Predojević, A. M. Steinberg, and M. W. Mitchell. **Bright filter-free source of indistinguishable photon pairs**. *Opt. Express*, **16**(22):18145–18151, Oct 2008.

[35] Alessandro Cerè, Valentina Parigi, Marta Abad, Florian Wolfgramm, Ana Predojević, and Morgan W. Mitchell. **Narrowband tunable filter based on velocity-selective optical pumping in an atomic vapor**. *Opt. Lett.*, **34**(7):1012–1014, Apr 2009.

[36] R. T. Willis, F. E. Becerra, L. A. Orozco, and S. L. Rolston. **Photon statistics and polarization correlations at telecommunications wavelengths from a warm atomic ensemble**. *Opt. Express*, **19**(15):14632–14641, Jul 2011.

[37] Dong-Sheng Ding, Zhi-Yuan Zhou, Bao-Sen Shi, Xu-Bo Zou, and Guang-Can Guo. **Generation of non-classical correlated photon pairs via a ladder-type atomic configuration: theory and experiment**. *Opt. Express*, **20**(10):11433–11444, May 2012.

[38] T. Chanelière, D. N. Matsukevich, S. D. Jenkins, T. A. B. Kennedy, M. S. Chapman, and A. Kuzmich. **Quantum Telecommunication Based on Atomic Cascade Transitions**. *Phys. Rev. Lett.*, **96**:093604, Mar 2006.

[39] Shengwang Du, Pavel Kolchin, Chinmay Belthangady, G. Y. Yin, and S. E. Harris. **Subnatural Linewidth Biphotons with Controllable Temporal Length**. *Phys. Rev. Lett.*, **100**:183603, May 2008.

[40] Matthaus Halder, Alexios Beveratos, Nicolas Gisin, Valerio Scarani, Christoph Simon, and Hugo Zbinden. **Entangling independent photons by time measurement**. *Nature Physics*, **3**:692–695, 2007.

[41] C. K. Hong, Z. Y. Ou, and L. Mandel. **Measurement of subpicosecond time intervals between two photons by interference**. *Phys. Rev. Lett.*, **59**:2044–2046, Nov 1987.

[42] Gurpreet Kaur Gulati, Bharath Srivathsan, Brenda Chng, Alessandro Cerè, Dzmitry Matsukevich, and Christian Kurtsiefer. **Generation of an exponentially rising single-photon field from parametric conversion in atoms**. *Phys. Rev. A*, **90**:033819, Sep 2014.

[43] R. Mcmillan A., Laurent Labonté, S. Clark A., Brin Bell, Anthony Martin, Olivier Alibart, William J. Wadsworth, Sébastien Tanzilli, and J. G. Rarity. **Two-photon interference between disparate sources for quantum networking**. *Scientific Reports*, **3**:2032, June 2013.

[44] Sergey V Polyakov, Andreas Muller, Edward B Flagg, Alex Ling, Natalia Borjemscaia, Edward Van Keuren, Alan Migdall, and Glenn S Solomon. **Coalescence of Single Photons Emitted by Disparate Single-Photon Sources: The Example of InAs Quantum Dots and Parametric Down-Conversion Sources**. *Phys. Rev. Lett.*, **107**(15):157402, October 2011.

[45] D. Nodop, C. Jauregui, D. Schimpf, J. Limpert, and A. Tünnermann. **Efficient high-power generation of visible and mid-infrared light by degenerate four-wave-mixing in a large-mode-area photonic-crystal fiber**. *Opt. Lett.*, **34**(22):3499–3501, Nov 2009.

[46] E. A. Goldschmidt, M. D. Eisaman, J. Fan, S. V. Polyakov, and A. Migdall. **Spectrally bright and broad fiber-based heralded single-photon source**. *Phys. Rev. A*, **78**:013844, Jul 2008.

[47] Jay E. Sharping, Kim F. Lee, Mark A. Foster, Amy C. Turner, Bradley S. Schmidt, Michal Lipson, Alexander L. Gaeta, and Prem Kumar. **Generation of correlated photons in nanoscale silicon waveguides**. *Opt. Express*, **14**(25):12388–12393, Dec 2006.

[48] Alain Aspect, Philippe Grangier, and Gérard Roger. **Experimental Tests of Realistic Local Theories via Bell's Theorem**. *Phys. Rev. Lett.*, **47**:460–463, Aug 1981.

[49] Robert W. Boyd. **Chapter 1 - The Nonlinear Optical Susceptibility**. In Robert W. Boyd, editor, *Nonlinear Optics (Third Edition)*, pages 1 – 67. Academic Press, Burlington, third edition edition, 2008.

[50] R.W Hellwarth. **Theory of phase-conjugation by four-wave mixing in a waveguide**. *Quantum Electronics*, **15**:101–109, 2003.

[51] J. AuYeung and A. Yariv. *Phase Conjugate Optics*, **21** of *Springer Series in Optical Sciences*, pages 492–503. Springer Berlin Heidelberg, 1979.

[52] Hendrik J. Gerritsen. **Non linear effects in image formation**. *Applied Physics Letters*, **10**(9):239–241, 1967.

[53] R. E. Slusher, L. W. Hollberg, B. Yurke, J. C. Mertz, and J. F. Valley. **Observation of Squeezed States Generated by Four-Wave Mixing in an Optical Cavity**. *Phys. Rev. Lett.*, **55**:2409–2412, Nov 1985.

[54] R. T. Willis, F. E. Becerra, L. A. Orozco, and S. L. Rolston. **Four-wave mixing in the diamond configuration in an atomic vapor**. *Phys. Rev. A*, **79**:033814, Mar 2009.

[55] R. T. Willis, F. E. Becerra, L. A. Orozco, and S. L. Rolston. **Photon statistics and polarization correlations at telecommunications wavelengths from a warm atomic ensemble**. *Opt. Express*, **19**(15):14632–14641, Jul 2011.

[56] C. H. van der Wal, M. D. Eisaman, A. Andre, R. L. Walsworth, D. F. Phillips, A. S. Zibrov, and M. D. Lukin. **Atomic Memory for Correlated Photon States**. *Science*, **301**:196–200, 2003.

[57] Stephen E. Harris. **Electromagnetically Induced Transparency**. *Physics Today*, **50**(7):36–42, 1997.

[58] Carl E. Wieman and Leo Hollberg. **Using diode lasers for atomic physics**. *Review of Scientific Instruments*, **62**(1), 1991.

[59] Gary C. Bjorklund. **Frequency-modulation spectroscopy: a new method for measuring weak absorptions and dispersions**. *Opt. Lett.*, **5**(1):15–17, Jan 1980.

[60] J.L. Hall, L. Hollberg, T. Baer, and H.G. Robinson. **Optical heterodyne saturation spectroscopy**. *Applied Physics Letters*, **39**:680–682, November 1981.

[61] D.W Preston. **Doppler-free saturated absorption: Laser spectroscopy**. *Am. J. Phys.*, **64**:1432–1436, 1996.

[62] K. Lindquist, M. Stephens, and C. Wieman. **Experimental and theoretical study of the vapor-cell Zeeman optical trap**. *Phys. Rev. A*, **46**:4082–4090, Oct 1992.

[63] Jayampathi C. B. Kangara, Andrew J. Hachtel, Matthew C. Gillette, Jason T. Barkeloo, Ethan R. Clements, Samir Bali, Brett E. Unks, Nicholas A. Proite, Deniz D. Yavuz, Paul J. Martin, Jeremy J. Thorn, and Daniel A. Steck. **Design and construction of cost-effective tapered amplifier systems for laser cooling and trapping experiments**. *American Journal of Physics*, **82**(8):805–817, 2014.

[64] H.J. Metcalf and P. van der Straten. *Laser Cooling and Trapping*. Graduate Texts in Contemporary Physics. Springer New York, 1999.

[65] John Prodan, Alan Migdall, William D. Phillips, Ivan So, Harold Metcalf, and Jean Dalibard. **Stopping Atoms with Laser Light**. *Phys. Rev. Lett.*, **54**:992–995, Mar 1985.

[66] E. Riis C.S. Adams. **Laser cooling and trapping of neutral atoms**, 1997.

[67] Christopher J. Foot. *Atomic Physics (Oxford Master Series in Atomic, Optical and Laser Physics)*. Oxford University Press, USA, 1 edition, February 2005.

[68] Stephen E. Harris. **Electromagnetically Induced Transparency**. *Physics Today*, (50):36–40, July 1997.

[69] S. D. Jenkins, D. N., T. Chanelière, S.-Y. Lan, T. A. B. Kennedy, and A. Kuzmich. **Quantum telecommunication with atomic ensembles**. *J. Opt. Soc. Am. B*, **24**(2):316–323, Feb 2007.

[70] Roy J. Glauber. **The Quantum Theory of Optical Coherence**. *Phys. Rev.*, **130**:2529–2539, Jun 1963.

[71] Leonard Mandel and Emil Wolf. *Optical Coherence and Quantum Optics*. Cambridge University Press, 1 edition, September 1995.

[72] Bharath Srivathsan. *Heraded single photon for interaction with a single atom (in preparation)*. PhD thesis, National University of Singapore, 2014.

[73] R. H. Dicke. **Coherence in Spontaneous Radiation Processes**. *Phys. Rev.*, **93**:99–110, Jan 1954.

[74] M. Gross, C. Fabre, P. Pillet, and S. Haroche. **Observation of Near-Infrared Dicke Superradiance on Cascading Transitions in Atomic Sodium**. *Phys. Rev. Lett.*, **36**:1035–1038, Apr 1976.

[75] N. Skribanowitz, I. P. Herman, J. C. MacGillivray, and M. S. Feld. **Observation of Dicke Superradiance in Optically Pumped HF Gas**. *Phys. Rev. Lett.*, **30**:309–312, Feb 1973.

[76] Rafael A. de Oliveira, Milrian S. Mendes, Weliton S. Martins, Pablo L. Saldanha, José W. R. Tabosa, and Daniel Felinto. **Single-photon superradiance in cold atoms**. *Phys. Rev. A*, **90**:023848, Aug 2014.

[77] M. Gross and S. Haroche. **Superradiance: An essay on the theory of collective spontaneous emission**. *Physics Reports*, **93**(5):301 – 396, 1982.

[78] Vlatko Balić, Danielle A. Braje, Pavel Kolchin, G. Y. Yin, and S. E. Harris. **Generation of Paired Photons with Controllable Waveforms**. *Phys. Rev. Lett.*, **94**:183601, May 2005.

[79] Claude Cohen-Tannoudji, Jacques Dupont-Roc, and Gilbert Grynberg. *Optical Bloch Equations*, pages 353–405. Wiley-VCH Verlag GmbH, 1994.

[80] B. R. Mollow. **Power Spectrum of Light Scattered by Two-Level Systems**. *Phys. Rev.*, **188**:1969–1975, Dec 1969.

[81] Benjamin Miquel and Hiroki Takesue. **Observation of 1.5 ?m band entanglement using single photon detectors based on sinusoidally gated InGaAs/InP avalanche photodiodes**. *New journal of Physics*, **11**, 2009.

[82] Xiaoying Li, Jun Chen, Paul Voss, Jay Sharping, and Prem Kumar. **All-fiber photon-pair source for quantum communications: Improved generation of correlated photons**. *Opt. Express*, **12**(16):3737–3744, Aug 2004.

[83] C Xiong, GD Marshall, A Peruzzo, Mirko Lobino, AS Clark, D-Y Choi, SJ Madden, CM Natarajan, MG Tanner, RH Hadfield, et al. **Generation of correlated photon pairs in a chalcogenide As2S3 waveguide**. *Applied Physics Letters*, **98**(5):051101, 2011.

[84] G. Rempe, R. J. Thompson, H. J. Kimble, and R. Lalezari. **Measurement of ultralow losses in an optical interferometer**. *Opt. Lett.*, **17**:363–365, 1992.

[85] D F. Walls and Gerard J. Milburn. *Quantum optics*. Springer, Jan 2008.

[86] Hacène Boukari, E. D. Palik, and Robert W. Gammon. **Closed-form expressions to fit data obtained with a multipass Fabry–Perot interferometer**. *Appl. Opt.*, **34**(1):69–86, Jan 1995.

[87] S.M. Barnett and P.M. Radmore. *Methods in Theoretical Quantum Optics*. Oxford science publications. Oxford University Press, USA, 2003.

[88] M. D. Reid and D. F. Walls. **Violations of classical inequalities in quantum optics**. *Phys. Rev. A*, **34**:1260–1276, Aug 1986.

[89] John F. Clauser and Michael A. Horne. **Experimental consequences of objective local theories**. *Phys. Rev. D*, **10**:526–535, Jul 1974.

[90] John S. Bell. **On the Einstein-Podolsky-Rosen paradox**. *Physics*, **1**:195–200, 1964.

[91] J. I. Cirac, P. Zoller, H. J. Kimble, and H. Mabuchi. **Quantum State Transfer and Entanglement Distribution among Distant Nodes in a Quantum Network**. *Phys. Rev. Lett.*, **78**:3221–3224, Apr 1997.

[92] Charles H. Bennett, Gilles Brassard, Claude Crépeau, Richard Jozsa, Asher Peres, and William K. Wootters. **Teleporting an unknown quantum state via dual classical and Einstein-Podolsky-Rosen channels**. *Phys. Rev. Lett.*, **70**:1895–1899, Mar 1993.

[93] **Advances in quantum metrology**. *Nat Photon*, **5**(4):222–229, April 2011.

[94] J. D. Franson. **Bell inequality for position and time**. *Phys. Rev. Lett.*, **62**:2205–2208, May 1989.

[95] J. Brendel, N. Gisin, W. Tittel, and H. Zbinden. **Pulsed Energy-Time Entangled Twin-Photon Source for Quantum Communication**. *Phys. Rev. Lett.*, **82**:2594–2597, Mar 1999.

[96] J. G. Rarity and P. R. Tapster. **Experimental violation of Bell's inequality based on phase and momentum**. *Phys. Rev. Lett.*, **64**:2495–2498, May 1990.

[97] Paul G. Kwiat, Klaus Mattle, Harald Weinfurter, Anton Zeilinger, Alexander V. Sergienko, and Yanhua Shih. **New High-Intensity Source of Polarization-Entangled Photon Pairs**. *Phys. Rev. Lett.*, **75**:4337–4341, Dec 1995.

[98] D. N. Matsukevich, P. Maunz, D. L. Moehring, S. Olmschenk, and C. Monroe. **Bell Inequality Violation with Two Remote Atomic Qubits**. *Phys. Rev. Lett.*, **100**:150404, Apr 2008.

[99] M. Muller, S. Bounouar, K. D. Jons, M. Glassl, and P. Michler. **On-demand generation of indistinguishable polarization-entangled photon pairs**. *Nat Photon*, **8**(3):224–228, March 2014.

[100] Andrew G. White, Daniel F. V. James, Philippe H. Eberhard, and Paul G. Kwiat. **Nonmaximally Entangled States: Production, Characterization, and Utilization**. *Phys. Rev. Lett.*, **83**:3103–3107, Oct 1999.

[101] Daniel F. V. James, Paul G. Kwiat, William J. Munro, and Andrew G. White. **Measurement of qubits**. *Phys. Rev. A*, **64**:052312, Oct 2001.

[102] Valerie Coffman, Joydip Kundu, and William K. Wootters. **Distributed entanglement**. *Phys. Rev. A*, **61**:052306, Apr 2000.

[103] William K. Wootters. **Entanglement of Formation of an Arbitrary State of Two Qubits**. *Phys. Rev. Lett.*, **80**:2245–2248, Mar 1998.

[104] Stewart D. Jenkins. *Theory of Light Atomic Ensemble Interactions: Entanglement, Storage, and Retrieval*. PhD thesis, Georgia Institute of Technology, 2006.

[105] G. Breit. **Quantum Theory of Dispersion (Continued). Parts VI and VII**. *Rev. Mod. Phys.*, **5**:91–140, Apr 1933.

[106] E.B. Aleksandrov. **Luminescence Beats Induced by Pulse Excitation of Coherent States**. *Optics and Spectroscopy*, **17**:522, dec 1964.

[107] J N Dodd, W J Sandle, and D Zissermann. **Study of resonance fluorescence in cadmium: Modulation effects and lifetime measurements**. *Proceedings of the Physical Society*, **92**(2):497, 1967.

[108] M. Schug, C. Kurz, P. Eich, J. Huwer, P. Müller, and J. Eschner. **Quantum interference in the absorption and emission of single photons by a single ion**. *Phys. Rev. A*, **90**:023829, Aug 2014.

[109] F.E. Bacerra, R.T Willis, S.L Rolston, and L.A. Orozco. **Quantum Beats from four-wave mixing in Rubidium 87**. *Revista Mexicana De Físca S*, **57**:23–28, 2011.

[110] A. Aspect, J. Dalibard, P. Grangier, and G. Roger. **Quantum beats in continuously excited atomic ensembles**. *Opt. Commun.*, **49**:429, 1984.

[111] Marlan O. Scully and Kai Drühl. **Quantum eraser: A proposed photon correlation experiment concerning observation and "delayed choice" in quantum mechanics**. *Phys. Rev. A*, **25**:2208–2213, Apr 1982.

[112] S. P. Walborn, M. O. Terra Cunha, S. Pádua, and C. H. Monken. **Double-slit quantum eraser**. *Phys. Rev. A*, **65**:033818, Feb 2002.

[113] H.-J. Briegel, W. Dür, J. I. Cirac, and P. Zoller. **Quantum Repeaters: The Role of Imperfect Local Operations in Quantum Communication**. *Phys. Rev. Lett.*, **81**:5932–5935, Dec 1998.

[114] H. J. Kimble. **The quantum internet**. *Nature*, **453**:1023–1030, 2008.

[115] H. de Riedmatten, I. Marcikic, W. Tittel, H. Zbinden, and N. Gisin. **Quantum interference with photon pairs created in spatially separated sources**. *Phys. Rev. A*, **67**:022301, Feb 2003.

[116] Rainer Kaltenbaek, Bibiane Blauensteiner, Marek Żukowski, Markus Aspelmeyer, and Anton Zeilinger. **Experimental Interference of Independent Photons**. *Phys. Rev. Lett.*, **96**(24):240502, June 2006.

[117] Thomas Legero, Tatjana Wilk, Markus Hennrich, Gerhard Rempe, and Axel Kuhn. **Quantum Beat of Two Single Photons**. *Phys. Rev. Lett.*, **93**(7):070503, August 2004.

[118] J Beugnon, M P A Jones, J Dingjan, B Darquié, G Messin, A Browaeys, and Philippe Grangier. **Quantum interference between two single photons emitted by independently trapped atoms**. *Nature*, **440**(7085):779–782, April 2006.

[119] Charles Santori, David Fattal, Jelena Vu ccaron kovi cacute, Glenn S Solomon, and Yoshihisa Yamamoto. **Indistinguishable photons from a single-photon device**. *Nature*, **419**(6907):594–597, October 2002.

[120] Anthony J. Patel, Raj B.and Bennett, Ian Farrer, David A. Ritchie, and Andrew J. Shields. **Two-photon interference of the emission from electrically tunable remote quantum dots**. *Nat Photon*, **4**:632635, 2010.

[121] Hannes Bernien, Lilian Childress, Lucio Robledo, Matthew Markham, Daniel Twitchen, and Ronald Hanson. **Two-Photon Quantum Interference from Separate Nitrogen Vacancy Centers in Diamond**. *Phys. Rev. Lett.*, **108**:043604, Jan 2012.

[122] A. Kiraz, M. Ehrl, Th. Hellerer, Ö. E. Müstecaplioğlu, C. Bräuchle, and A. Zumbusch. **Indistinguishable Photons from a Single Molecule**. *Phys. Rev. Lett.*, **94**:223602, Jun 2005.

[123] R. Lettow, Y. L. A. Rezus, A. Renn, G. Zumofen, E. Ikonen, S. Götzinger, and V. Sandoghdar. **Quantum Interference of Tunably Indistinguishable Photons from Remote Organic Molecules**. *Phys. Rev. Lett.*, **104**:123605, Mar 2010.

[124] T. Chanelière, D. N. Matsukevich, S. D. Jenkins, S.-Y. Lan, R. Zhao, T. A. B. Kennedy, and A. Kuzmich. **Quantum Interference of Electromagnetic Fields from Remote Quantum Memories**. *Phys. Rev. Lett.*, **98**:113602, Mar 2007.

[125] P Maunz, D L Moehring, S Olmschenk, K C Younge, D N Matsukevich, and C Monroe. **Quantum interference of photon pairs from two remote trapped atomic ions**. *Nature Physics*, **3**(8):538–541, August 2007.

[126] syed abdullah aljunid. *Interaction of a strongly focused light beam with single atoms.* PhD thesis, National University of Singapore, 2012.

[127] Sandoko Kosen. *Quantum interference between single photons from a single atom and a cold atomic ensemble.* Master's thesis, National University of Singapore, 2014.

[128] Syed Abdullah Aljunid, Gleb Maslennikov, Yimin Wang, Hoang Lan Dao, Valerio Scarani, and Christian Kurtsiefer. **Excitation of a single atom with exponentially rising light pulses**. *Phys. Rev. Lett*, **111**:103001, 2013.

[129] V.S. Malinovsky and J.L. Krause. **General theory of population transfer by adiabatic rapid passage with intense, chirped laser pulses**. *The European Physical Journal D - Atomic, Molecular, Optical and Plasma Physics*, **14**(2):147–155, 2001.

[130] John D. Feichtner, Joe H. Gallagher, and Masataka Mizushima. **Lifetime of the First Excited Atomic States of** Rb^{87}. *Phys. Rev.*, **164**:44–48, Dec 1967.

[131] U Volz and H Schmoranzer. **Precision lifetime measurements on alkali atoms and on helium by beamgaslaser spectroscopy**. *Physica Scripta*, **1996**(T65):48, 1996.

[132] peter nisbet jones. *Shaping single photons.* PhD thesis, University of Oxford, 2012.

[133] H. Paul. **Interference between independent photons**. *Rev. Mod. Phys.*, **58**:209–231, Jan 1986.

[134] M. Stobińska, G. Alber, and G. Leuchs. **Perfect excitation of a matter qubit by a single photon in free space**. *Europhys. Lett.*, **86**:14007, 2009.

[135] Yimin Wang, J Minář, Lana Sheridan, and Valerio Scarani. **Efficient excitation of a two-level atom by a single photon in a propagating mode**. *Phys. Rev. A*, **83**:063842, Jun 2011.

[136] Bharath Srivathsan, Gurpreet Kaur Gulati, Alessandro Cerè, Brenda Chng, and Christian Kurtsiefer. **Reversing the Temporal Envelope of a Heralded Single Photon using a Cavity**. *Phys. Rev. Lett.*, **113**:163601, Oct 2014.

[137] M Bader, S Heugel, A L Chekhov, M Sondermann, and G Leuchs. **Efficient coupling to an optical resonator by exploiting time-reversal symmetry**. *New Journal of Physics*, **15**(12):123008, 2013.

[138] Kyle J. Arnold, Markus P. Baden, and Murray D. Barrett. **Collective cavity quantum electrodynamics with multiple atomic levels**. *Phys. Rev. A*, **84**:033843, Sep 2011.

[139] Markus P. Baden, Kyle J. Arnold, Arne L. Grimsmo, Scott Parkins, and Murray D. Barrett. **Realization of the Dicke Model Using Cavity-Assisted Raman Transitions**. *Phys. Rev. Lett.*, **113**:020408, Jul 2014.

[140] Peter J. Mosley, Jeff S. Lundeen, Brian J. Smith, Piotr Wasylczyk, Alfred B. U'Ren, Christine Silberhorn, and Ian A. Walmsley. **Heralded Generation of Ultrafast Single Photons in Pure Quantum States**. *Phys. Rev. Lett.*, **100**:133601, Apr 2008.

[141] D. N. Matsukevich, T. Chanelière, S. D. Jenkins, S.-Y. Lan, T. A. B. Kennedy, and A. Kuzmich. **Deterministic Single Photons via Conditional Quantum Evolution**. *Phys. Rev. Lett.*, **97**:013601, Jul 2006.

[142] Jérémie Fulconis, Olivier Alibart, Jeremy L. O'Brien, William J. Wadsworth, and John G. Rarity. **Nonclassical Interference and Entanglement Generation Using a Photonic Crystal Fiber Pair Photon Source**. *Phys. Rev. Lett.*, **99**:120501, Sep 2007.

[143] Marcelo Davanco, Jun Rong Ong, Andrea Bahgat Shehata, Alberto Tosi, Imad Agha, Solomon Assefa, Fengnian Xia, William M. J. Green, Shayan Mookherjea, and Kartik Srinivasan. **Telecommunications-band heralded single photons from a silicon nanophotonic chip**. *Applied Physics Letters*, **100**(26):–, 2012.

[144] Christian Kurtsiefer, Sonja Mayer, Patrick Zarda, and Harald Weinfurter. **Stable Solid-State Source of Single Photons**. *Phys. Rev. Lett.*, **85**:290–293, Jul 2000.

[145] P Michler, A Kiraz, C Becher, W.V Schoenfeld, P.M Petroff, Lidong Zhang, E Hu, and A Imamoglu. **A Quantum Dot Single-Photon Turnstile Device**. *Science*, **290**:2282–2285, 2000.

[146] Axel Kuhn, Markus Hennrich, and Gerhard Rempe. **Deterministic Single-Photon Source for Distributed Quantum Networking**. *Phys. Rev. Lett.*, **89**:067901, Jul 2002.